공학박사 학위논문

Discrete element modelling of fracture transmissivity evolution around a deep geological repository for high-level radioactive waste

개별요소법을 활용한 고준위 방사성 폐기물

심층처분장 주변 균열투수량계수 변화 모델링

2021 년 2 월

서울대학교 대학원

에너지시스템공학부

권 새 하

Discrete element modelling of fracture transmissivity evolution around a deep geological repository for high-level radioactive waste

지도 교수 민 기 복

이 논문을 공학박사 학위논문으로 제출함
2020 년 11 월

서울대학교 대학원
에너지시스템공학부
권 새 하

권새하의 박사학위논문을 인준함
2020 년 12 월

위 원 장 　　송 재 준 　　　　　　　　(인)

부위원장 　　민 기 복 　　　　　　　　(인)

위　　원 　　전 석 원 　　　　　　　　(인)

위　　원 　　권 상 기 　　　　　　　　(인)

위　　원 　　지 성 훈 　　　　　　　　(인)

Abstract

Discrete element modelling of fracture transmissivity evolution around a deep geological repository for high-level radioactive waste

Saeha Kwon

Department of Energy Systems Engineering

Rock Mechanics & Rock Engineering Laboratory

The Graduate School

Seoul National University

High-level radioactive waste produced from nuclear power plant continuously emits radioactivity and heat after it has been disposed of, so it should be isolated from the biosphere for a sufficient amount of time. To dispose of high-level radioactive waste, deep geological repository systems consisting of engineered barriers and natural barriers are suggested. As a performance assessment, numerous experiments and numerical simulations are performed to characterize the long-term behaviors of engineered and natural barriers. Especially, the transmissivity of natural barriers is considered an important parameter related to radionuclide leakage. Therefore, the relation between transmissivity and a variety of thermal, hydraulic, and mechanical factors are raised, and quantitative studies to determine the effects

on transmissivity are suggested for performance assessment.

This thesis aims to quantify the transmissivity of natural barriers, especially crystalline fractured rock, under a variety of factors possibly happening during the construction and operation of a geological repository. Three-dimensional discrete element models were constructed based on the rock and fracture characteristics extracted from the Äspö Hard Rock Laboratory in Sweden to describe the realistic behaviors of the crystalline fractured rock. The effects of excavation damage zone, thermal loading, glaciation, and earthquake were applied to numerical models as the factors disturbing the fracture transmissivity. The excavation damage zone was considered the effect of stress re-distribution inducing the fracture normal deformation and shear slip. The heat sources, glacial boundary conditions, and dynamic load were separately applied to the tunnel model after the stress re-distribution to determine the transmissivity changes.

The transmissivity changes induced by the excavation damage zone appeared as three-order increases due to the combined effects of normal opening/closure and shear dilation, depending on the fracture orientation. Thermal, glacial, and earthquake scenarios included the loading and unloading cycles and recovered the initial stress conditions after each scenario ended. Irreversible transmissivity increases were found for several fractures under thermal, glacial, and earthquake effects. According to the transient analysis of transmissivity and stress path, the normal closure dominated the transmissivity during loading cycles, while the irreversible effects of shear dilation were revealed after the dissipation of normal loads. These reversible normal deformations and irreversible shear dilations appeared depending on the geometrical characteristics of fractures.

To define the relation between the geometry of fractures and transmissivity

changes, the uniformly distributed joints were applied on the tunnel models to analyze the effects of excavation damage zone, thermal loading, glaciation, and earthquake. The transmissivity increases were larger on joints parallel to the direction of maximum horizontal stress due to the absence of effects from the largest principal stress inducing the normal stress on fractures. At the vicinity of the tunnel, the joints that are slightly inclined from the tunnel surface accompanied a large amount of permanent transmissivity increase, because the additional stresses were converted to the shear stress on fractures due to the mechanically free surface.

The results extracted in this research can be the basis data for performance assessments of geological repositories under excavation damage zone, thermal loading, glaciation, and earthquake scenarios which can happen during the lifetime of repositories. This thesis implies that the hydraulic parameters of natural barriers should be considered as dynamic variables that change as a repository operates.

Contents

Lists of Tables

Lists of Figures

Chapter 1. Introduction

1.1 Motivation

Nuclear power plants generate energy from the fuel in the nuclear reactor. After a specific time period, about 5 years for light water reactors and 10 months for heavy water reactors, the reactor fuel cannot generate enough energy to generate electricity. The spent fuel should be replaced by new fuel and disposed of as high-level radioactive waste (HLW). Even though the HLW no longer generates enough energy for the reactor, the fuel still emits radiation and heat, which can threaten the biosphere. Therefore, the HLW should be covered and isolated until the sufficient radioactivity decays.

<div align="center">(a)　　　　　　　　　　　　　　　(b)</div>
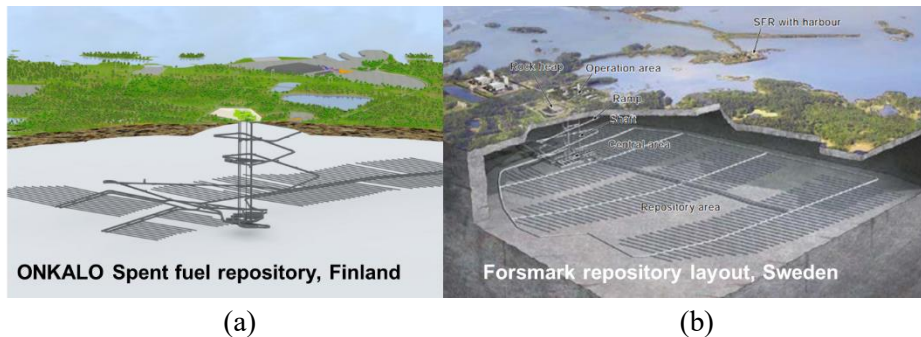
Figure 1.1 Schematic layout of the planned spent fuel repository in (a) Olkiluoto, Finland (Sannio et al., 2012) and (b) Forsmark, Sweden (SKB, 2010b)

Currently, most countries temporarily store the spent fuel in an interim storage facility or in a spent fuel pool within the nuclear power plant. Only Finland and Sweden have suggested plans for a final repository for HLW in the Olkiluoto and Forsmark sites, respectively, based on the sufficient geological, hydrological,

ecological, and social considerations (Figure 1.1). Both countries decided to dispose of the HLW in a system of tunnels at a depth of about 500 m in the appropriate bedrock. The disposed HLW will be covered by two categories of barriers, natural barriers indicating the bedrock itself and engineered barriers consisting of the copper canisters and bentonite buffer materials (Figure 1.2).
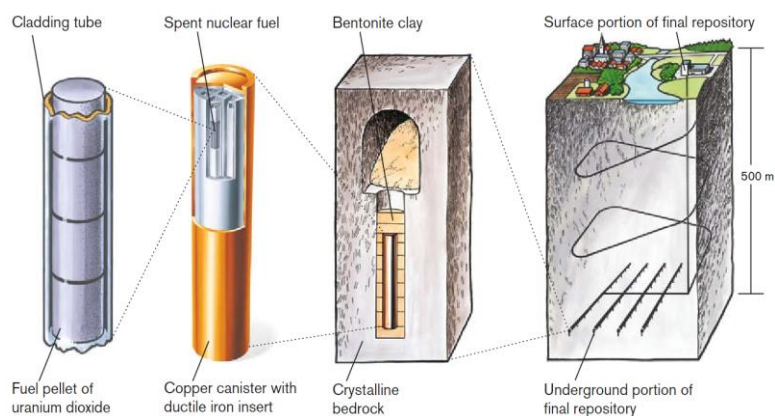
Figure 1.2 Overview of the deep geological repository system (SKB, 2010b)

To ensure the safety of the geological repository during the sufficient lifetime, both countries constructed an underground research laboratory to perform the in-situ measurements, characterize the bedrock, and demonstrate the deposition systems in the repository environment. According to the data extracted from the underground research laboratory, numerous modelling works were performed to simulate the construction, operation, and closure of the geological repository. Especially, assessing the post-closure safety is the most difficult issue with numerous complicated factors. The Nuclear Energy Agency (NEA) shares a compilation of databases regarding the factors for the performance assessment divided by features, events and processes (FEPs) through international collaboration (NEA, 2019).

2

In the international FEP lists, each scenario focuses on the leakage of radionuclides to quantify the threat on repository systems in aspects of geological, mechanical, hydrological, chemical, and biological effects. In particular, the hydraulic effect is considered an important aspect directly deciding the possibility of radionuclide leakage. Furthermore, the hydraulic responses in the barrier system can affect other aspects, such as mechanical, thermal, chemical, and biological processes. Therefore, it is important to understand how external factors disturb the hydraulic parameters of a repository system and quantify the hydraulic responses induced by possible scenarios. Sufficient numerical simulations should be performed to predict the performance of the geological repository throughout its lifespan.

In this research, four issues critical to the geological repository's safety, especially the natural barrier, are selected: excavation damage zone (EDZ), thermal loading, glaciation, and earthquake. The change of transmissivity, as the parameter representing the ability to cause a leakage of radionuclide, is carefully investigated under each scenario. Special emphasis is given to the competing reversible normal deformations and irreversible shear dilation on the transmissivity change regarding the geometrical characteristics of discontinuities. The uniformly jointed models provide the basic estimations of the magnitude and spatial extent of transmissivity evolutions using the geometry of discontinuities.

1.2 **Objectives**

The ultimate goal of this study is to suggest considerations for performance assessments of a geological repository for high-level radioactive waste in the crystalline rock of a candidate site. To achieve this goal, two detailed objectives are proposed:

(1) *To quantify the transmissivity evolution in the natural barrier based on the fracture crystalline rock during the construction and operation of the geological repository.* Three-dimensional models were constructed containing the deterministic discrete fracture network and horseshoe-shaped tunnel to describe the Äspö Hard Rock Laboratory (HRL). The detailed mechanical behavior of fractures was applied based on observations from field and laboratory measurement. Four important considerations were applied to the constructed three-dimensional discrete element model (DEM): excavation, thermal loading, glaciation, and earthquake (Figure 1.3). First, the effects of stress re-distribution by excavation were analyzed as fracture transmissivity changes resulting from deformations and slip. The effects of thermal loading, glaciation, and earthquake were additionally applied to the tunnel model to quantify the disturbance. The permanent fracture transmissivity change and spatial extent of the disturbance were compiled for each effect.
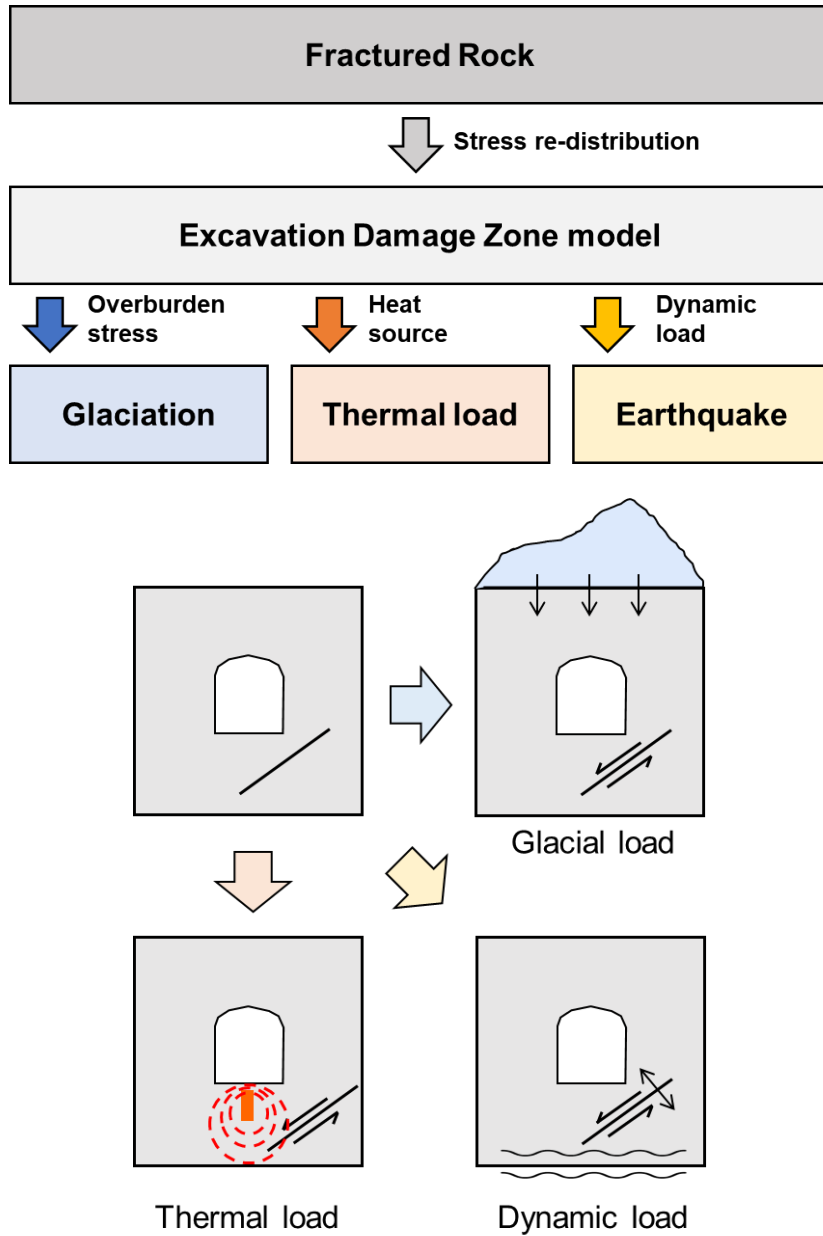
Figure 1.3 Simulation procedures in this research

(2) *To analyze the fracture transmissivity evolution by the geometrical characteristics of the fractures.* To define the relation between the fracture transmissivity and fracture geometry, the uniformly jointed tunnel models were constructed using a three-dimensional DEM model. On jointed models with different

dips and dip directions, the fracture transmissivity changes induced by stress re-distribution in EDZ, thermal loading, glaciation, and earthquake were compiled by their monitored positions. The spatial extent of the disturbed area was visualized for each model and each scenario.

Chapter 2. Literature review

2.1 Excavation Damage Zone

The Excavation Damage Zone (EDZ) has been an important issue for the safety of underground structures. Hudson et al. (2009) defined EDZ as a rock zone with inevitable and irreversible changes around the underground excavation. The EDZ entails the hydromechanical and geochemical modifications that induce significant changes in the flow and transport properties of rock (Tsang et al., 2005a).

Harrison and Hudson (2000) distinguished between the Excavation Damage Zone (EDZ) and Excavation disturbed Zone (EdZ) depending on the reversibility of the property changes of the area. EdZ is associated with the reversible process without major changes in the hydraulic and mechanical properties of the host rock. On the other hand, EDZ accompanies a significant irreversible change in the properties and instability of the underground structures. EDZ can be further distinguished into Highly Damaged Zone (HDZ), stress-induced EDZ (EDZsi), construction-induced EDZ (EDZci or CDZ), and blast-induced damage zone (BIDZ) (Figure 2.1). HDZ includes the interconnection of macro-fractures caused by blasting or high stresses and accompanies significant changes to hydro-mechanical properties. EDZsi and EDZci are irreversibly damaged zones created by the stress re-distribution and construction methods, respectively. BIDZ is also indicates a zone fractured irreversibly by blasting, but BIDZ entails extremely significant property changes (Siren et al., 2015).
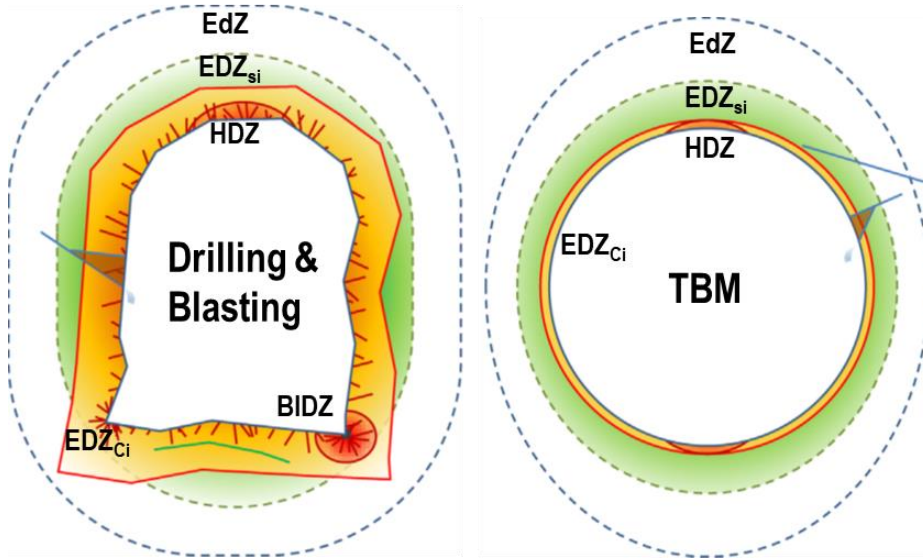
Figure 2.1 Overview of the damaged zones by origin (modified from Siren et al., 2015)

In crystalline rocks, EDZ can also be defined as a zone of irreversible deformation due to fracture slip, creation, and propagation (Pusch, 1989; Hudson et al., 2009). The fluid flow through the crystalline rock tends to be dominated by the fracture network due to the lower permeability of the host rock than the fracture permeability. Therefore, it is important to understand the fracture behavior to characterize the irreversible property changes in the EDZ.

The best way to characterize the EDZ is the in-situ measurements and laboratory tests of the specimens from the underground research laboratory (URL). In the in-situ scale, the extent of the EDZ can be directly visualized by the dye penetrating test (Figure 2.2), radar methods, or geometrical/geological measurements (Hudson et al., 2009). Simple tests, including acoustic emission measurement, seismic investigations, or hydraulic tests measuring water flow, water pressure, and gas permeability, can be performed in the tunnel (Follin et al., 2014).
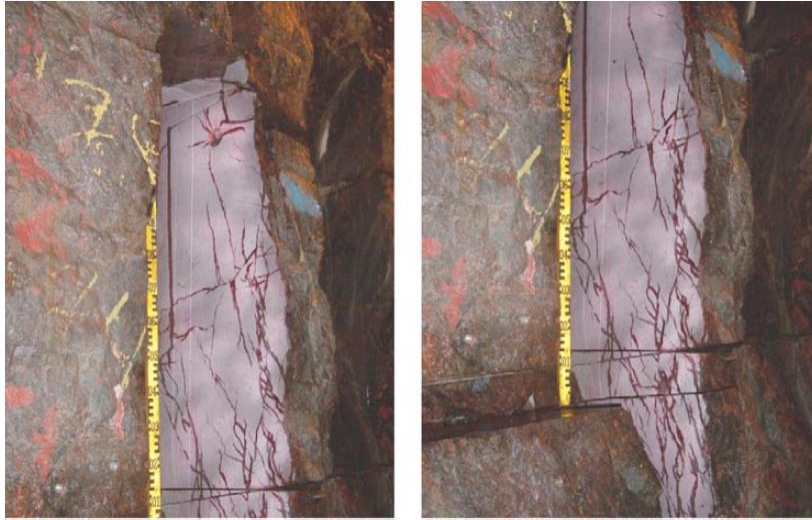
Figure 2.2 Dyed fractures from the excavation of the TASQ tunnel in Äspö Hard Rock Laboratory (Bäckblom, 2008)

Kelsall et al. (1984) introduced the permeability change observed around the underground opening. The effects of excavation on the permeability change are analyzed based on the blast damage and the stress relief. Stress relief at the vicinity of the opening could induce two to three orders increase in hydraulic conductivity. The calculated damage zone is validated by the results of the in-situ permeability tests performed at the Stripa Mine in Sweden.

Emsley et al. (1997) tried to characterize the mechanical and hydraulic damage and disturbance induced by tunnel excavation with blasting and tunnel boring (TBM) in Äspö HRL, Sweden (Figure 2.3). The extent of the EDZ was captured by monitoring Acoustic Emission (AE) events. The extent of the blasting method was 1 meter, while the extent of the TBM was a few tens of centimeters. The permeability distributions by depth in the boreholes were compared using hydraulic tests before and after the excavation, and significant changes in hydraulic properties only appeared in the damage zone (Figure 2.3).
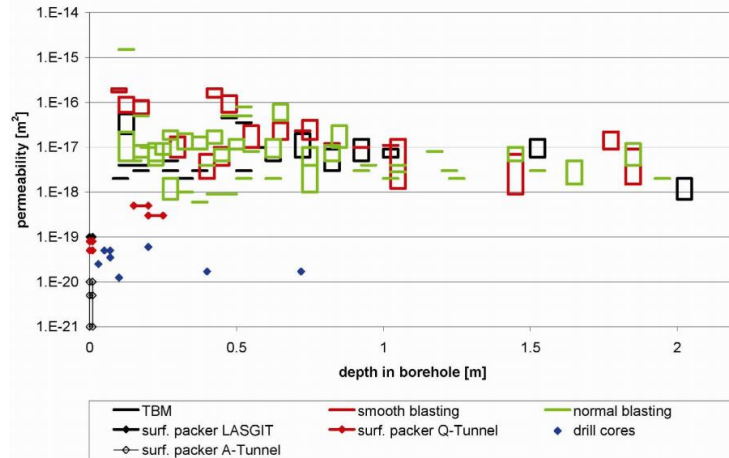
Figure 2.3 The permeability distributions by excavation methods (Nowak et al., 2007)

In Korea, previous studies have characterized the disturbance on the thermal, mechanical, and hydraulic properties in EDZ by in-situ measurements in the KAERI Underground Research Tunnel (KURT) (Kwon and Cho, 2008; Kwon et al., 2009). KURT was excavated using drill and blasting methods, and the spatial extent of the EDZ was estimated to be about 1.5 m from the tunnel surface. A one-order increase of hydraulic conductivity and significant decreases of P wave velocity, deformation modulus, tensile strength, and cohesion in the EDZ were observed in the in-situ and laboratory tests. The elastic modulus in the EDZ was reduced by 56% of the intact rock property, and it was able to determine the extent of the EDZ by the disturbance of the deformation modulus. Lee (2012) performed both in-situ and laboratory experiments with specimens extracted from KURT to determine the physical, mechanical, and thermal characteristics of a blast-induced EDZ. The extent of the EDZ was able to be determined by the thermal conductivity disturbance on fractured rock.

Autio et al. (1998) and Kiuru et al. (2019) also characterized the physical, hydraulic, and mechanical excavation damage on the ONKALO underground research facility in Finland. According to the hydraulic tests on the deposition holes, about a 2.4 times increase of porosity and a two-order increase of hydraulic conductivity were measured at the disturbed zone (Autio et al., 1998). The laboratory tests showed the depth-dependency of resistivity, S wave velocity, shear impedance, shear modulus and elastic modulus, and the estimated EDZ area induced by the drill and blasting method was about 0.7 m from the tunnel surface (Kiuru et al., 2019). However, the dependencies of properties in the EDZ were different in granitic and gneissic specimens, so the texture and mineralogy of the host rock should be carefully considered when investigating the EDZ area.

To determine the effects of the EDZ on the stability of underground structures including the geological repository for the HLW, efforts have been made to emulate the mechanical behaviors of the EDZ on the fractured rock mass. Shen and Barton (1997) determined the stress disturbed zone induced by the stress re-distribution around the opening through an analysis and discontinuum numerical simulations of the shear slip zone on the uniformly jointed rock model. The discontinuum model was appropriate to investigate the spatial extent of the disturbed zone around the opening, and the results were validated using an analytical solution considering the shear failure of the joints.

In the international research project DECOVALEX-THMC, there was a study of the multiple-code simulation for characterizing the thermal, hydrological, mechanical, and chemical processes in EDZ (Rutqvist et al., 2009). Five numerical codes were adopted to model the EDZ evolution including boundary element, finite

element, finite difference, particle mechanics, and the cellular automata approach. The finite difference and cellular automata approaches emulated the characteristics of the EDZ through stress-permeability functions calibrated by field observations. The finite element method (FEM) used the continuum damage model considering the permeability evolution based on aperture changes from the crack tensor theory. The boundary element method described the crack propagation and considered the permeability changes according to the aperture and cubic law. The particle model also described the crack propagation using particle bonds, but it cannot simulate the permeability change. Practically, the finite difference and cellular automat approaches were simple but powerful options to describe the EDZ, while the other methods might suggest the detailed behaviors of the EDZ with the appropriate laboratory data as its input parameters.

Siren et al. (2015) tried to compare the construction-induced EDZ and stress-induced EDZ on the circular TBM tunnel model in the Äspö HRL constructed by the two-dimensional displacement discontinuity method (DDM). The hydraulic conductivity was the target parameter, and the construction-induced effect appeared up to 100 mm in depth as a one-order increase while the stress-induced effect slightly appeared up to 80 mm in depth. The simulation results followed the observed extent of the EDZ by the ground penetrating radar measurement.

To concentrate on the detailed fracture behavior of the EDZ, DEM is frequently adopted as a simulation tool. Mas Ivars et al. (2015) constructed a numerical model of the TASQ tunnel at the Äspö HRL with a three-dimensional DEM. In the tunnel model, five discontinuities were included with the stress-dependent normal stiffness based on the in-situ observation (Hakami et al., 2008). The simulation focused on

the shear displacement on fractures induced by the stress re-distribution around the tunnel. The stress-induced shear displacement ranged from 1.2 to 2.8 mm.

Hong (2020) constructed a two-dimensional discrete element model to analyze the effects of the slip zone and permeability on the disposal tunnels and holes. Applying the uniformly distributed joints and discrete fracture networks around the opening, the extent of the slip and aperture changed area were investigated. The magnitude and extent of the aperture changes resulted in a high dependency of the stress ratios, friction angles, and fracture orientations.

Zhao et al. (2020) performed a two-dimensional discrete element numerical modelling to determine the extent of the EDZ based on the fracture roughness and orientation. Two joint sets with a persistent geometry were applied in the horseshoe-shaped tunnel model, and a variety of joint angles were prepared. The EDZ appeared as three types of joint behaviors: failure, open, and shear slip, and the zone areas were mainly dominated by the joint orientations and roughness.

Those previous numerical studies determining the spatial extent and magnitude of the EDZ generally focused on the shear zone or shear displacement on a few discontinuities. Although several studies have analyzed EDZ occurrences by joint geometrical/geomechanical characteristics using uniformly jointed models or fracture networks models, the numerical simulations have been generally performed from two-dimensional discontinuum models. In this thesis, three-dimensional discontinuum models were prepared with both fracture networks and uniformly distributed joints to determine the extent and magnitude of the stress-induced effects in EDZs. Two-dimensional models provide conservative results assuming persistent discontinuities and plane stress conditions (Min and Thoraval, 2012). On the other

hand, three-dimensional models can perform more accurate simulations while considering the exact geometry of discontinuities and three-dimensional stress conditions applied on the surfaces.

2.2 **Thermal loading**

Apart from the radionuclides, the HLW emits decay heat, which can cause temperature changes by conduction and convection. The temperature increases can disturb the physical, chemical, and biological properties of both the natural and engineered barriers (NEA, 2019), so the maximum temperatures expected on the designed repository model should be carefully analyzed using numerical simulations. There have been some efforts to control the expected maximum temperature on repository models by selecting the proper disposal concept, design of the engineered barrier, and waste acceptance criteria (Bond and Watson, 2012).

In KBS-3H systems, the maximum temperature within the spent nuclear fuel will be between 200°C and 250°C, and the outer surface temperature of the canister will not exceed 100°C (Ikonen, 2006). Ikonen and Raiko (2015) performed thermal simulations to decide the proper canister spacings for KBS-3H systems at the Olkiluoto site. The allowable maximum canister temperature was 95°C, and the canister spacing limit to not exceed the temperature threshold was 7.9~9.0 m, depending on the canister design. Hökmark et al. (2009) also derived the temperature distribution at the canister, buffer, and rock wall by spacing for the Laxemar and Forsmark sites. The peak buffer temperature appeared 5-15 years after deposition, and the temperature-spacing curves were plotted by the thermal conductivity of the rock (Figure 2.4).
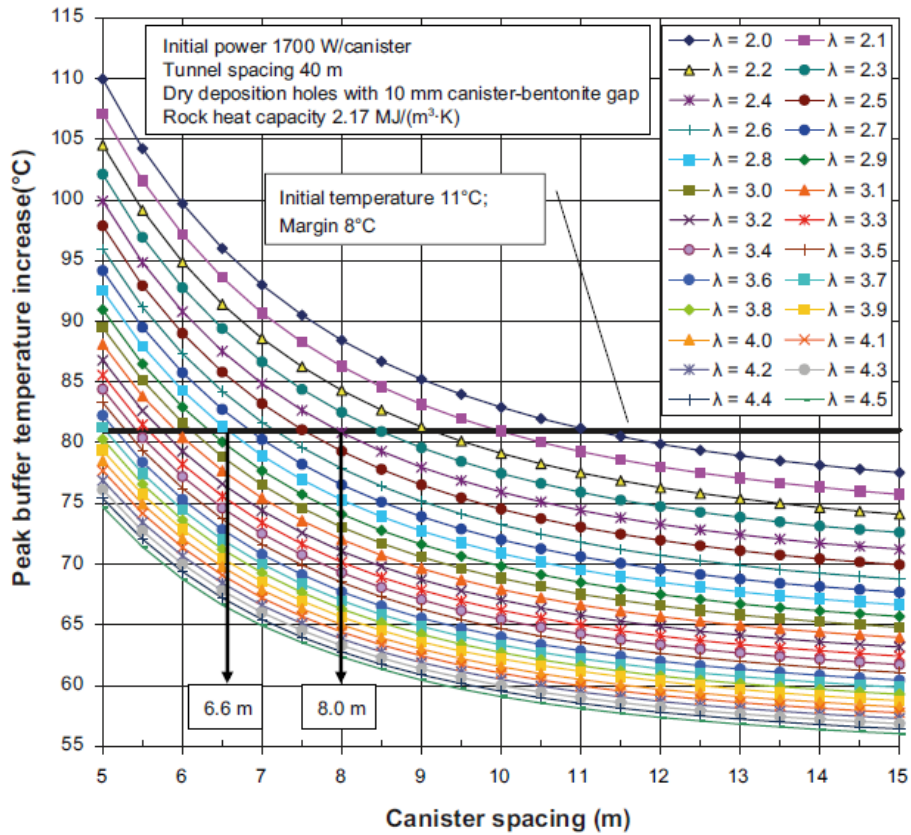
Figure 2.4 Nomographic chart between canister spacing and peak buffer temperature increase for KBS-3 concept with various thermal conductivity of rock (λ) (Hökmark et al., 2009)

Previous research has been done to determine the thermally induced disturbance on the stability of natural barriers. To monitor the realistic behaviors of rock mass under the repository conditions, in-situ heater tests were performed at the underground research facilities. At the Yucca Mountain Drift Scale Test, the large-scale in-situ heater tests were performed during a 4-year heating with the wall temperature up to 200°C and 4-year cooling process, and they monitored the transient permeability changes (Rutqvist et al., 2008). Both the in-situ tests and the numerical simulations with the finite difference method showed a one-order decrease

of permeability during the heating phase and remaining permeability change factors ranging from 0.2 to 1.8 after the 4-year cooling period.

In ONKALO, Finland, the in-situ heater tests monitoring the pillar stability and spalling strength around the boreholes proceeded as part of Posiva's Olkiluoto Spalling Experiment (POSE) (Valli et al., 2013). The heat source, of which the maximum temperature was below 100°C, induced 100 MPa of the maximum principal stress magnitude. Since the crack damage threshold of pegmatitic granite at the Olkiluoto site was 85±17 MPa, the experiment was expected to exceed the threshold. However, the spalling was not observed at the hole.

The Äspö Pillar Stability Experiment (APSE) also proceeded for the thermo-mechanical processes on the fractured rock mass during the in-situ heater tests in the Äspö HRL in Sweden (Figure 2.5) (Andersson and Martin, 2009; Andersson et al., 2009). To observe the thermally induced failure process, four heaters maintaining up to 60°C of temperature were mounted and operated during about 60 days. The thermally induced tangential stress was estimated at about 25 MPa by the backcalculation according to the thermal expansion and elastic modulus, and the acoustic emission was also counted during the temperature increase.
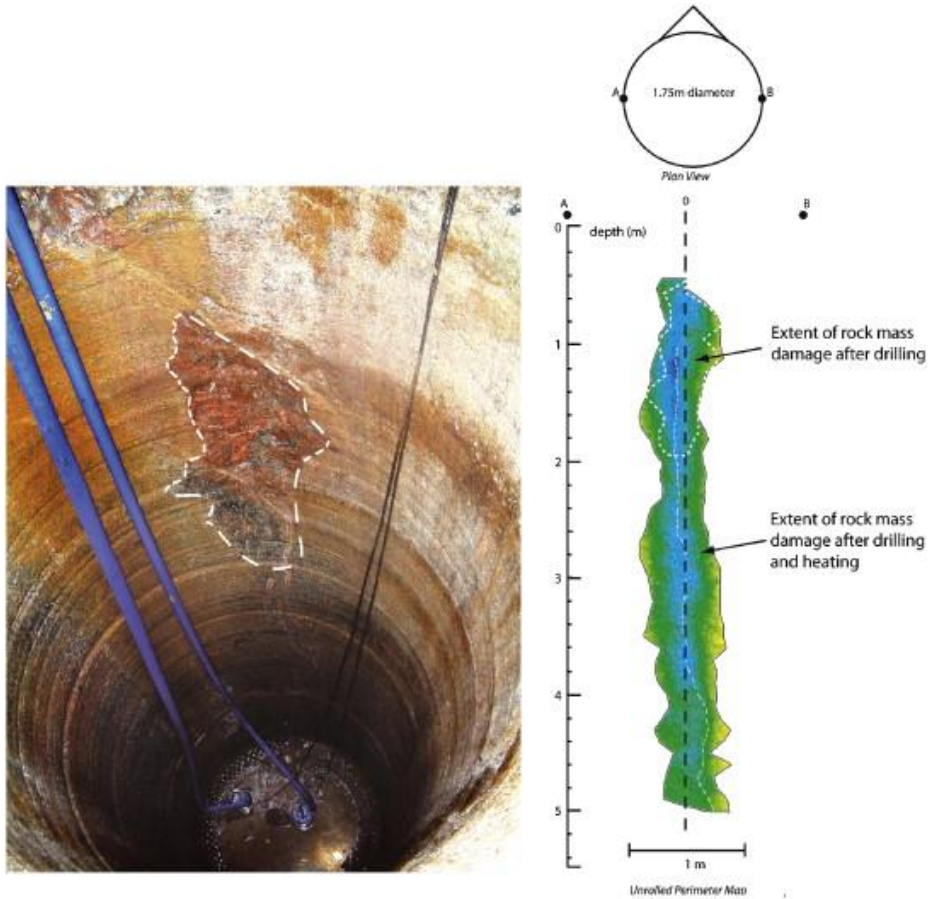
Figure 2.5 Observed spatial extent of damage after drilling (dashed irregular oval)
and heating scanned by the 3D-laser method from APSE (Andersson, 2007)

Koyama et al. (2013) numerically determined the thermo-mechanical processes
in APSE using FEM and particle-based DEM. The simulations showed the
qualitative agreement on the transient temperature and stress path compared to the
in-situ test results, and the two-dimensional DEM emulated the crack generation
observed at the site as spalling.

Hökmark et al. (2010) constructed a three-dimensional DEM model of the
Laxemar and Forsmark sites containing the heat source emulating from the spent
fuel canister. The numerical model included the two fractures, and the transient

18

change of fractures transmissivity was monitored during the 100,000-year thermal cycle, of which the maximum rock wall temperature was up to 50°C. The thermally induced fracture transmissivity change was dominated by the thermal compression during heating cycles, and the shear displacement was negligible.

(a)   (b)
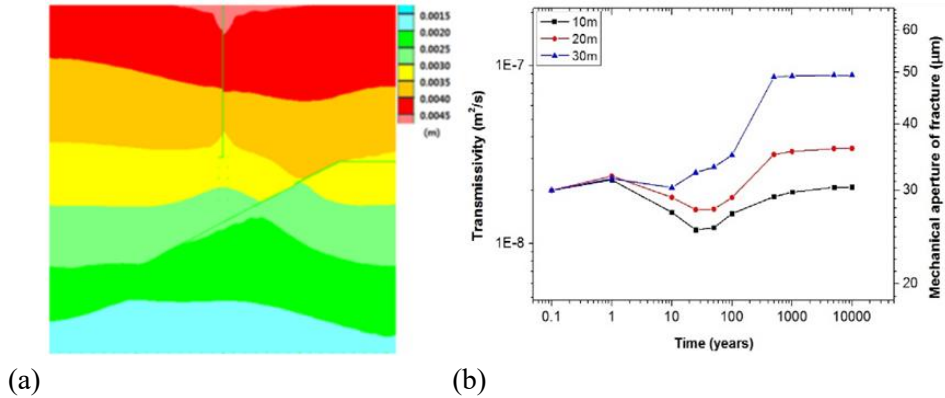
Figure 2.6 (a) Thermally induced displacement around the canister and (b) transmissivity changes on the fracture (Park et al., 2015)

Min et al. (2013) simulated the thermo-mechanical processes on fractured rock in the Forsmark site focusing on the shear slip of the fractures. The three-dimensional continuum model was constructed for the purpose of determining the thermally induced shear slip zone. During the 10,000-year thermal cycles with a 50°C maximum temperature, the probabilities of shear slip and permeability changes were calculated by time. Park et al. (2015) tried to quantitatively derive the shear behavior induced by the temperature change in the fractured rock model of the Forsmark site using the two-dimensional DEM (Figure 2.6). After 100,000 years of heating and cooling cycles, the permanent increase in the fracture transmissivity caused by thermo-shearing was observed as a one- to three-order increase from the initial value.

The numerical studies regarding the thermal effects on fractured rock have been

generally performed on discontinuum models containing few discontinuities. Furthermore, the results considering the thermally induced shear dilation on the hydraulic parameters of fractures are rare, especially in the three-dimensional discontinuum methods. Therefore, the quantification of thermo-shearing in the three-dimensional discontinuum models with multi fractures is worthy of investigation.

2.3 Glaciation

The final disposal for nuclear waste should assure the performance of barriers during its lifetime, which is expected to be up to 100,000 years after closure (SSM, 2008). Therefore, every possible event that can disturb the performance of the disposal needs to be determined before operation. Loutre and Berger (2000) warned that the next glacial phase is expected within 100,000 years, so glaciation should also be treated as a possible event able to disturb the mechanical conditions around the geological disposal, especially in high latitude areas, including Fennoscandia, northern Russia, and Canada (Lund et al., 2009).

For the performance assessment of ONKALO, which is the site for the final disposal of spent nuclear fuel in Olkiluoto, Finland, the growth and retreat of ice sheets are treated as important factors disturbing hydraulic, mechanical, and chemical analyses (Posiva, 2012). Pimenoff et al. (2011) predicted three stadial periods with a potential for ice sheet formation around 10-20 kyr, 50-60 kyr, and 90-100 kyr after the present, which corresponds to the Northern Hemisphere's summer insolation minima and the estimated maximum ice sheet thickness of 2.5 km in Olkiluoto area. Based on the climate prediction, Posiva (2012) aimed to compare the glacial effect to the mechanical strength of the engineered barrier in aspects of the shear displacement, swelling pressure, and hydrostatic load from Raiko et al. (2010).

Sweden is preparing for the final disposal of spent nuclear fuel at the Forsmark area with the site investigations and safety assessments regarding the geology, hydrology, ecology, and social impact. In the safety assessment, four climate cases were assumed, and the Weichselian glacial cycle climate case was the scenario

21

concerning ice sheet development (SKB, 2014). Näslund (2006) generated the prospective Weichselian glacial model for the Forsmark and Oskarshamn sites using thermo-mechanical ice sheet modelling with the climate pattern and an estimated 3 km of maximum ice thickness and about 500 m of shore-level increase at the Forsmark site (Figure 2.7).
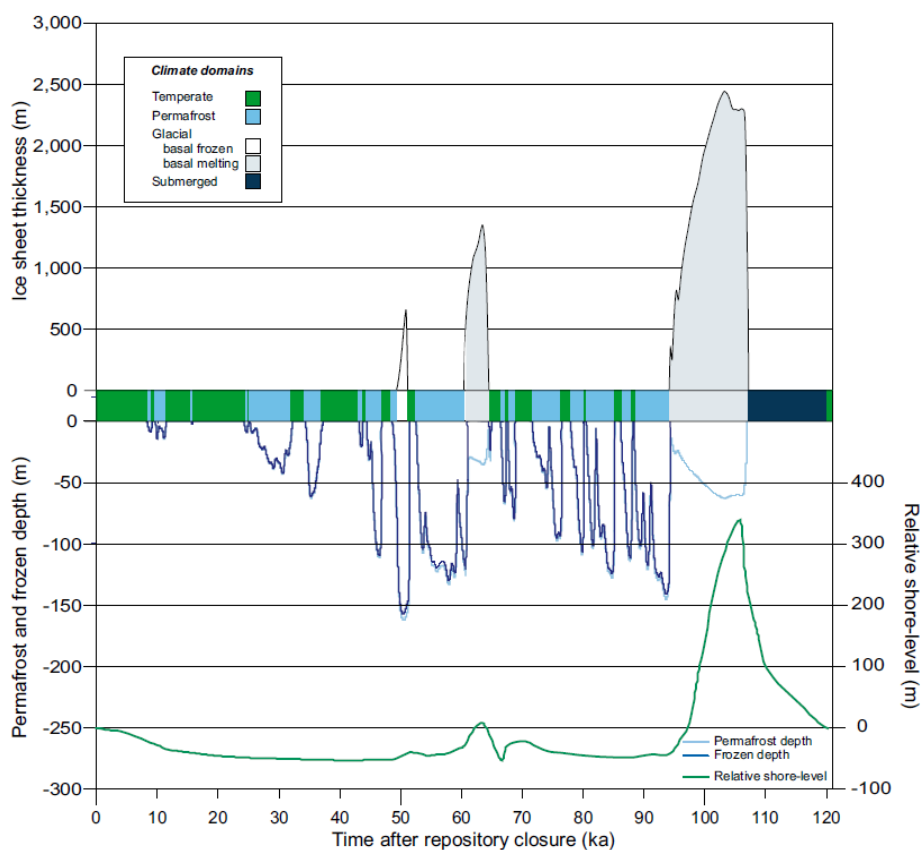
Figure 2.7 Estimated evolution of climate-related variables at the Laxemar site for the base variant of the main scenario (Näslund, 2006)

Based on the Weichselian glacial model, Lund et al., (2009) constructed three-dimensional ice and earth models and calculated the repository depth glacially

22

induced stress at the Forsmark and Oskarshamm site. The two glacial maxima entailed two loading and unloading cycles, and the overburden stresses were up to 40 MPa in Forsmark and 30 MPa in Oskarshamn, respectively. The derived stress model reflected the induced horizontal stress and pore pressure during the growth and retreat of the overburdened ice sheet. A fault stability analysis was also performed using the Coulomb failure criterion on two stress fields with the glacially induced stress model, and fault instabilities resulted under the reverse faulting background stress.

Hökmark et al. (2010) performed detailed numerical simulations about the mechanical behavior of fractured rock using a coupled thermo-hydro-mechanical analysis on the three-dimensional DEM models. The stress conditions of Weichselian glacial model were applied to the repository model containing two fractures. The simulations focused on simulating the fracture transmissivity using normal deformations according to the stress-transmissivity model constructed using the lab tests, but the effects of the shear slip were ignored. The transmissivity changes on fractures during the glacial scenarios were analyzed from the normal deformations, and an increase factor of three at maximum was found at the repository depth.

Park et al. (2015) simulated the glaciation scenarios on the Forsmark site using a two-dimensional DEM model. The numerical model contained a horseshoe-shaped tunnel and deposition hole, and the Weichselian glacial model was applied to the upper and lateral boundaries of the cross-section. The transmissivity changes on five pre-existing fractures were monitored during the glaciation scenarios based on the normal deformations and shear dilations of fractures, but the glacial effects on the

transmissivity were negligible.

Hutri and Antikainen (2002) modelled the mechanical response induced by glacial loading at the Olkiluoto site, Finland. The three-dimensional rock mass model containing the fracture zones was constructed by the DEM model, and the overburden stresses were applied based on four glaciation scenarios, of which the maximum loads were up to 25 MPa. The shear displacements on nine selected fractures were monitored during each glaciation scenario. The glacially induced shear displacement in the fractured bedrock model was less than 1 cm.

(a)   (b)
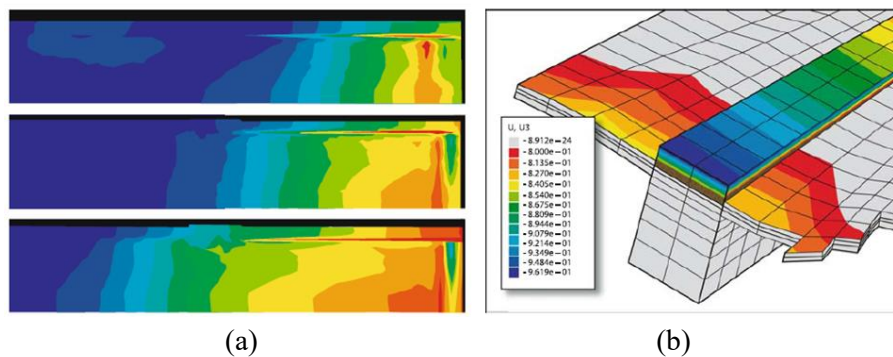
Figure 2.8 (a) Hydraulic pressure development on the fracture zone under the advancement of an icesheet and (b) vertical displacment focusing on the horizontal fracture zone (Vidstrand et al., 2008)

The considerations of glaciation and permafrost were also addressed in the international research project DECOVALEX III (Chan et al., 2005; Tsang et al., 2005b; Vidstrand et al., 2008). The Bench Mark Test 3 (BMT3) of this project aimed to determine the long-term hydraulic/mechanical evolutions on a fractured rock under glaciation and deglaciation at the underground research facility site in Whiteshell, Canada. In BMT3, two- and three-dimensional numerical models

containing the fracture zones with different hydraulic conductivity were constructed in both FDM and FEM. The target parameter was the hydraulic pressure in the groundwater flow during the advancement of an ice sheet, and the coupled hydro-mechanical simulations drew out the 2-3 orders of hydraulic pressure increase on the fracture zone due to glaciation (Figure 2.8).

The glacially induced disturbance on the fractured rock mass was mostly characterized as shear displacement on discontinuities in the previous numerical studies. However, there was a lack of consideration of the detailed mechanical behavior of discontinuities like shear slip. Therefore, this thesis focuses on the fracture behaviors induced by the glacial scenarios and investigates the disturbance trends using fracture geometry.

2.4 Earthquake

Even though the deep underground structures are safer and less vulnerable to earthquake than surface or shallow structures (Hashash et al., 2001), earthquakes can threaten the stability of geological repositories. Especially, earthquake effects on rock masses containing discontinuities accompany rock fall, spalling, faulting, opening deformations, and displacement from the discontinuities which can induce the collapse of tunnels, disturbance of supports or lining, and canister breakage (Figure 2.9) (Sharma and Judd, 1991; Fäith et al., 2008). Therefore, seismic hazards are considered an important issue that could possibly disturb the nuclear waste, engineered barrier systems, and the surrounding rocks of the geological repository (NEA, 2019).

In Sweden's repository performance assessment, earthquake events were considered as a less probable scenario (SKB, 2015). The effects of earthquakes are quantified as flow increases around the disposal according to the annual probability of earthquakes. After earthquake events, the concrete barriers in silos are assumed to have failed. A quantitative modelling of the water flow changes based on the failure of the concrete barriers has been performed and resulted in 1 m^3/year of flow increases induced by the earthquake. The earthquake-induced flow increases were applied to the calculation of the annual dose by radionuclides as a less probable effect.
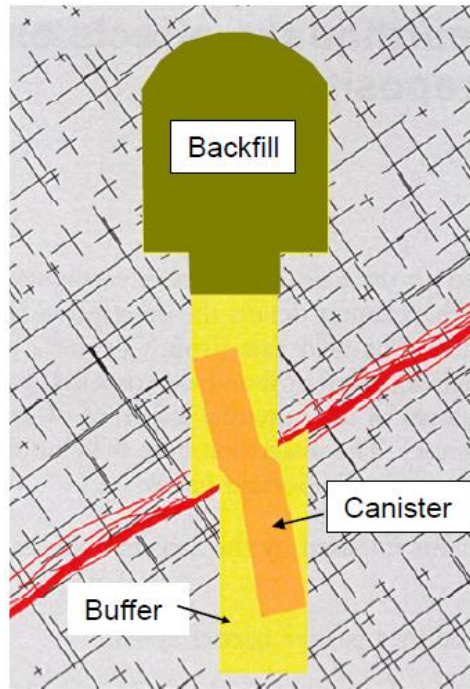
Figure 2.9 Possible canister breakage due to large earthquake (Fäith et al., 2008)

Seismic hazard was also considered an important scenario in the Total System Performance Assessment Model for the License Application (TSPA-LA) for the proposed HLW repository at Yucca Mountain (Meacham et al., 2011). Helton et al. (2014) quantified the expected dose to the Reasonably Maximally Exposed Individual (RMEI) by means of a probabilistic analysis of a seismic scenario class. The ground motion modelling showed that the seismic event could contribute to the mean annual dose of up to 1 mrem/year.

The effect of the earthquakes on hydrological systems has been raised in a variety of aspects. Elkhoury et al. (2006) investigated the relation between the occurrence of earthquakes and the permeability of aquifers according to the long-term observations of the tidal response observed from the well-aquifer systems in Southern California. The tidal response was indicated by the water level changes

induced by the permeability changes, and the transient trends of the permeability changes coincided with the occurrence of the large magnitude of earthquakes (Figure 2.10).
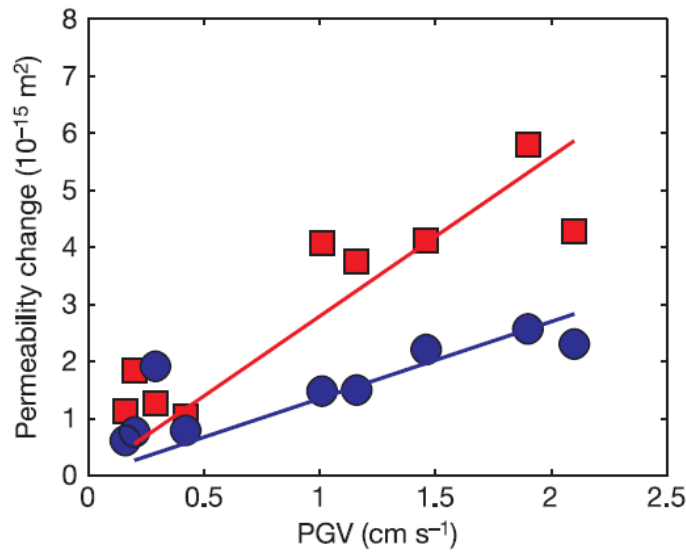
Figure 2.10 Permeability changes observed from two different well-aquifer systems according to the PGV of each earthquake (Elkhouri et al., 2006)

Focusing on the detailed mechanical behaviors of the rock mass under the dynamic hazard, Xue et al. (2013) monitored the tidal response of water levels to determine the transient permeability of the damage zone from the causative fault of the magnitude 7.9 Wenchuan earthquake. The transient permeability calculated from the tidal response indicated faulting from the abrupt permeability increases and a healing fault from the rapid permeability decreases.

On the laboratory scale, Elkhoury et al. (2011) performed experiments applying the pore pressure oscillations representing the dynamic stresses on the fractured rock and measured the effective permeability. Under the pore pressure oscillations with

about 10^{-2} to 10^{-1} MPa of peak pressures, 50% of the effect permeability increases were observed from the fracture systems. The effective permeability enhancement of the fractured rock showed trends proportional to the oscillation amplitude. In detail, both reversible and irreversible mechanisms were raised to explain the observed transient effective permeability, such as clogging and microfracturing, respectively (Figure 2.11).
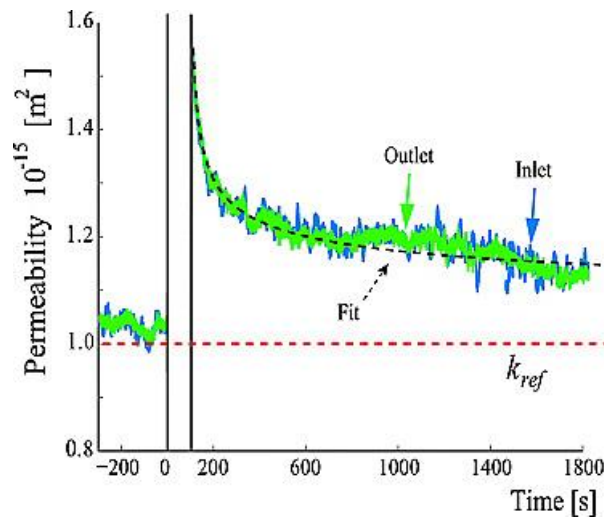
Figure 2.11 Effective permeability before and after the pore pressure oscillation (Elkhoury et al., 2011)

From a numerical aspect, Ahola and Chowdhury (1997) performed a dynamic analysis on a 2D DEM model describing the Yucca Mountain site. The dynamic loads histories, with 0.2g and 0.4g of peak underground acceleration, were prepared as the input parameters based on the velocity and displacement recorded from the Mexico City earthquake in 1985 and were applied to the bottom boundary of two-dimensional models with three circular tunnels at the center. A significant shear displacement of about 0.7 cm was found around the tunnel under a 0.4g earthquake

29

with the additional shear failure zones induced by dynamic loading.

Park (2015) simulated the earthquake scenarios on two-dimensional DEM models of the Forsmark site. The synthetic ground motion histories constructed by SKI (1992) were applied on the bottom boundary of the DEM model under the in-situ stress conditions at the repository depth considering the glaciation scenarios. The shear stress induced by the earthquake model with 0.1 m/s of peak ground velocity was about 1 MPa on the fracture surface, and that fracture showed less than 1 μm of permanent normal displacement after the earthquake model dynamic simulations with 0.1 m/s of peak ground velocity.

Gomes and Lemos (2020) constructed three-dimensional DEM models to characterize the dynamic hazard of the Baixo Sabor dam, which has a rock mass containing two faults. Five seismic records with different peak ground accelerations were prepared and applied on the bottom boundary of the dam and rock mass models. During the 8 second dynamic duration time, the permanent shear displacements on two joints were monitored. The dynamic model with 0.5g of peak acceleration resulted in 8 cm of maximum shear displacement on the contained joint.

According to previous studies, the three-dimensional simulations of earthquake scenarios on fractured rock have been rare, particularly the simulations determining the hydraulic parameters, so quantitative information regarding the earthquake-induced disturbance on natural barriers has not been well determined. This study provides the quantitative hydraulic and mechanical response on fractured rock considering the detailed fracture behaviors during the earthquake scenario.

Chapter 3. Theory and methodology

3.1 Discrete Element Method

In rock engineering problems, both continuum and discontinuum methods are often used to simulate the mechanical behavior of rock mass. The continuum methods, including the Finite Difference Method (FDM), Finite Element Method (FEM), and Boundary Element Method (BEM), focus on the deformations of material, so they are usually adopted to simulate the intact rock or highly fractured rock, which can be treated as the intact rock with the equivalent properties. On the other hand, the discontinuum methods, including the Discrete Element Method (DEM), reflect the movement of components, which is appropriate for describing the individual movement of the moderately fractured rock (Jing, 2003).

The DEM models the mechanical behaviors of assemblies of discrete particles or blocks. There are three important aspects constituting the DEM model: the representations contacts, the representations of solid material, and the scheme used to detect and revise the set of contacts (Cundall and Hart, 1992). The discrete blocks or particles representing solid material can be moved, rotated, and deformed and the contacts can be compressed, opened or slipped (Chen and Zhao, 1998).

The DEM was first developed by Cundall (1971) with the rigid blocks and contacts governed by the spring stiffness and friction. The model allowed for large displacements as the separation of blocks and automatic update of contacts. UDEC (Itasca, 2014) and 3DEC (Itasca, 2013) are representative DEM tools with deformable blocks and various joint models in 2D and 3D, respectively.
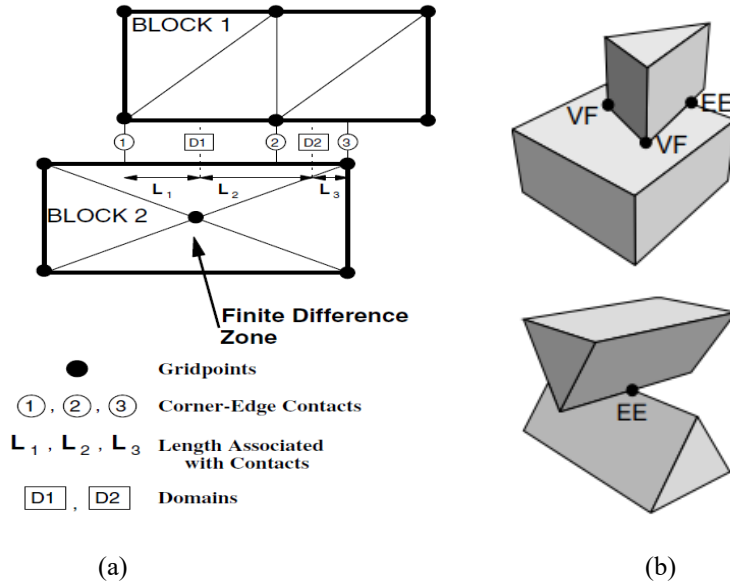
Figure 3.1 (a) Vertex-face contacts and domains between two deformable blocks (Itasca, 2014) and (b) vertex-face (VF) sub-contacts and edge-edge (EE) sub-contacts in 3DEC (Lemos, 2008)

DEM represents the interaction between blocks by contact points. It is important to identify the appropriate contact to describe the mechanical response throughout the numerical model. The contacts between the faces of each block are generated on vertex-face points (Figure 3.1). At each contact, the interaction between blocks is described by displacement and force. In 3DEC, the interacting points between blocks are represented as sub-contacts, which include vertex-face sub-contact and edge-edge sub-contact. Each sub-contact has a designated sub-contact area and normal and shear stress calculated from the contact forces (Lemos, 2008).

3DEC uses a transient algorithm to calculate the motion of the polyhedral block system using an explicit solution for the subdivided finite difference meshes (Itasca,

2013). The equation of motion for all blocks decides the new positions of the blocks and calculates the new velocities and displacements of the sub-contacts. The updated sub-contact velocities are applied to the sub-contact force-displacement relation to provide the new sub-contact forces. The calculated sub-contact forces are applied to the corresponding blocks in the next timestep. This calculation cycle repeats until the model reaches the specified limit (Figure 3.2).

Constitutive relations for all contacts

K_n

ΔU_t

ΔU_n

K_t F_t

F_n

detail

$F_n := F_n - K_n\, \Delta U_n$

$F_t := F_t - \kappa_t\, \Delta U_t$

$F_t := \min\{\mu F_n,\ \mathrm{abs}(F_t)\}\mathrm{sgn}(F_t)$

Rigid blocks

Deformable blocks

All blocks

All blocks

F_i^c

F_i^c

element

grid point

Equations of motion

X_i

At block centroids

$F_i = \Sigma F_i^c$

$M = \Sigma\, (e_{ij}\, x_i\, F_j)$

$\dfrac{d^2 U_i}{dt^2} = F_i / m$

$\dfrac{d^2 \theta}{dt^2} = M/I$

etc.
$\vdots$

At elements (zones):

$\Delta \varepsilon_{ij} = \dfrac{1}{2}\left[\dfrac{d}{dx_j}\left(\dfrac{dU_i}{dt}\right) + \dfrac{d}{dx_i}\left(\dfrac{dU_j}{dt}\right) \right] \Delta t$

$\sigma_{ij} = C(\sigma_{ij},\ \Delta \varepsilon_{ij},\ ...)$

at grid points:

$F_i = F_i^e + F_i^c$

$\dfrac{d^2 U_i}{dt^2} = F_i / m$

etc. ....

$t := t + \Delta t$

Back to

Figure 3.2 Calculation cycle for the distinct element method (Jing, 2003)

3.2 Formulations

3.2.1 Deformable block motions

3DEC allows for internal deformations of each block during the calculation of block motion by discretizing the blocks into finite-difference tetrahedral elements (Itasca, 2013). The discretized deformable blocks have gridpoints whose movement decides the motion of the block. The equations of motion at each gridpoint can be written in the form of Eq. (3.1), with the gridpoint forces containing the external and internal forces in Eq. (3.2).

$$\ddot{u}_i = \frac{\int_s \sigma_{ij}\, n_j\, ds + F_i}{m} + g_i, \qquad\qquad (3.1)$$

where $\ddot{u}_\iota$ denotes the i direction component of the acceleration vector; s is the surface enclosing the mass; m, lumped at the gridpoint; σ_{ij} is the stress tensor on the surface; n_j is the unit normal to s, g_i is the gravitational acceleration vector; and F_i is the i direction component of the gridpoint force vector, which can be formulated as:

$$F_i = F_i^z + F_i^c + F_i^l, \qquad\qquad (3.2)$$

where F_i^z is the i direction component of force vector contributed by the internal stresses in the zones adjacent to the gridpoint; F_i^c is the i direction component of sub-contact force vector from the two faces adjacent to the gridpoint; and F_i^l is the i direction component of external applied force vector.

35

The net gridpoint force vector ΣF_i is calculated at each gridpoint and every timestep during the simulation. The net gridpoint force vector should be zero if the body is at equilibrium; otherwise, the gridpoint will be accelerated according to the central difference scheme of Newton's second law of motion (Eq. (3.3)).

$$\dot{u}_i^{(t+\Delta t/2)} = \dot{u}_i^{(t-\Delta t/2)} + \sum F_i^{(t)} \frac{\Delta t}{m}, \qquad (3.3)$$

where $\dot{u}_i$ is the i direction component of the velocity vector, and t is the time.

Based on the gridpoint displacements, the strains and rotations can be decided as follows in Eqs. (3.4) and (3.5).

$$\dot{\epsilon}_{ij} = \frac{1}{2}\left(\dot{u}_{i,j} + \dot{u}_{j,i}\right) \qquad (3.4)$$
$$\dot{\theta}_{ij} = \frac{1}{2}\left(\dot{u}_{i,j} - \dot{u}_{j,i}\right), \qquad (3.5)$$

where $\dot{\epsilon}_{ij}$ is the components of the strain tensor in the ij direction, and $\dot{\theta}_{ij}$ is the components of the rotation tensor in the ij direction. The constitutive equations of the deformable blocks based on the strain can be written as Eq. (3.6).

$$\Delta\sigma_{ij}^e = \lambda\Delta\epsilon_v\delta_{ij} + 2\mu\Delta\epsilon_{ij}, \qquad (3.6)$$

where λ and μ are the Lame parameters, $\Delta\sigma_{ij}^e$ is the elastic increments of stress tensor in ij direction, $\Delta\epsilon_v$ is the increment of volumetric strain, and δ_{ij} is the Kronecker delta function.

3.2.2 Formulations used in thermal features

In the 3DEC model constructed in this research, the heat transfers via conduction through the host rock (Itasca, 2013). The transient heat conduction follows Fourier's law, as written in Eq. (3.7).

$$\mathbf{q} = -k\nabla T \tag{3.7}$$

where $\mathbf{q}$ is the heat flux vector, k is the thermal conductivity tensor, and ∇T is the temperature gradient. The thermal conductivity of the host rock is assumed as an isotropic value in this research.

Transferred heat induces the temperature change on elements. The energy balance equation under heat transfer can be written as Eq. (3.8).

$$-q_i + q_v = \rho C_v \frac{\partial T}{\partial t} \tag{3.8}$$

where q_i is the heat flux vector, q_v is the volumetric heat source intensity, ρ is the mass density of the medium, and C_v is the specific heat at constant volume. Although the volumetric strain can cause temperature changes, the amount of mechanically induced temperature change is negligible. Therefore, only the one-way coupling from thermal calculation to mechanical calculation is considered in this simulation. Based on the temperature change and thermal expansion coefficient, the thermally induced stress can be formulated as Eq. (3.9).

$$\Delta\sigma_{ij} = -3K\alpha_t\Delta T\delta_{ij} \tag{3.9}$$

where K is the bulk modulus, α_t is the linear thermal expansion coefficient, and ΔT is the temperature change.

3.2.3 Joint constitutive models

The movement of blocks accompanies the displacement of sub-contacts that represent the joint. According to the constitutive relations for sub-contacts, the new sub-contact forces to be applied on the adjacent block are calculated. In the normal direction, 3DEC uses the linear stress-displacement relationship governed by the stiffness (Eq. (3.10)).

$$\Delta\sigma_n = -k_n\Delta u_n^e, \tag{3.10}$$

where $\Delta\sigma_n$ is the effective normal stress increment applied on the sub-contacts, k_n is the joint normal stiffness, and Δu_n^e is the elastic component of incremental normal displacement.

In shear, additional considerations in the constitutive equation defining the joint slip are required. In this research, the Coulomb slip model is adopted to describe the joint slip according to the normal and shear stress applied to the sub-contacts due to its simplicity and the numerous measurements of properties regarding this criteria (Eqs. (3.11) and (3.12)).

$$|\tau_s| \leq C + \sigma_n \tan\phi = \tau_{max}, \ then \ \Delta\tau_s = -k_s\Delta u_s^e \qquad (3.11)$$
$$|\tau_s| \geq \tau_{max}, \ then \ \tau_s = sign(\Delta u_s)\tau_{max}, \qquad (3.12)$$

where σ_n and τ_s are the effective normal and shear stress, k_s is the joint shear stiffness, Δu_s is the total incremental shear displacement, Δu_s^e is the elastic component of the incremental shear displacement, C is the cohesive strength, and ϕ is the friction angle.

During the shear slip, the joint can dilate due to the roughness of the joint surface (Figure 3.3). The amount of shear dilation is proportional to the shear displacement as written in Eq. (3.13).

$$\Delta u_n^s = tan(\phi_d) \cdot \Delta u_s, \qquad (3.13)$$

where Δu_n^s is the shear component of the incremental normal displacement, and ϕ_d is the dilation angle.
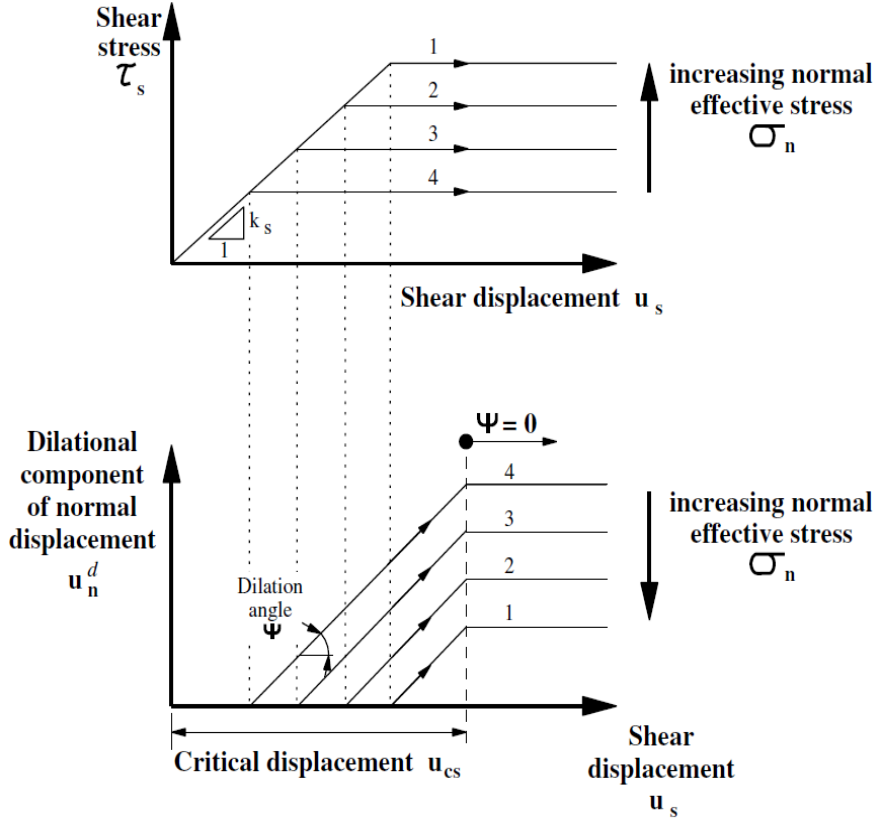
Figure 3.3 Coulomb slip and dilation model in 3DEC (Itasca, 2013)

3.2.4 Fracture Transmissivity

Fractures usually dominate the fluid flow through the rock mass in less permeable rock. Fractures allow the fluid flow based on their transmissivity which can be calculated from the hydraulic aperture and cubic law shown in Eq. (3.14) (Zimmerman and Bodvarsson, 1996).

$$T = \rho_w g e^3 / 12 \mu_w, \tag{3.14}$$

where T is the fracture transmissivity, ρ_w is the fluid density, g is the

gravitational acceleration, e is the fracture aperture, and μ_w is the fluid viscosity.

Therefore, the aperture of the fracture should be carefully monitored to maintain the hydraulic performance of the fractured rock. As suggested from the joint constitutive models, both normal and shear deformations simultaneously play a role disturbing the mechanical conditions of fractured rock under the effective normal and shear stress changes on the fractured surface (Figure 3.4). The mechanical aperture of fractures can be directly affected by the normal displacement consisting of elastic normal deformation and dilation by shear slip.
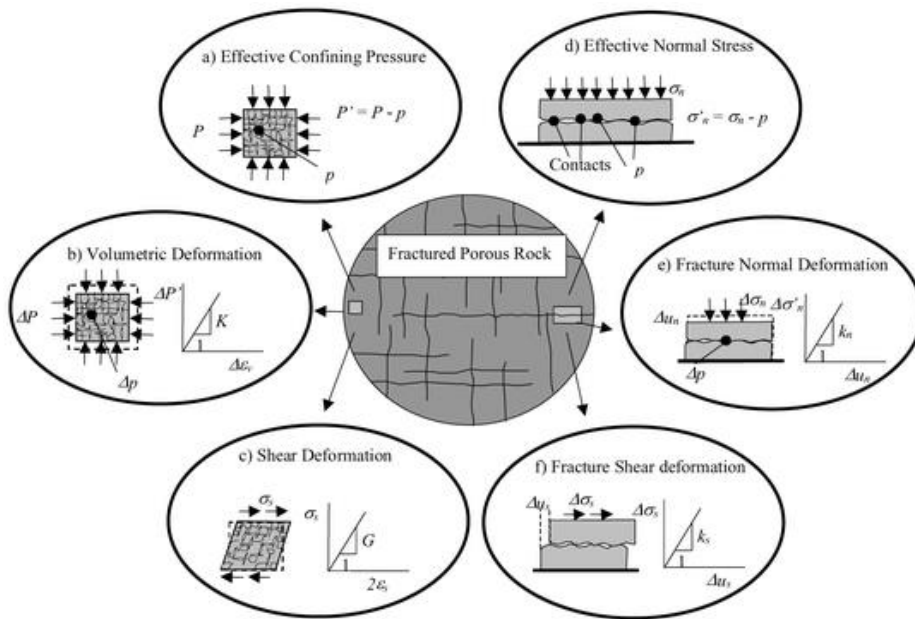
Figure 3.4 Schematic overview of a fractured geological medium (Rutqvist and Stephansson, 2003)

Barton et al. (1995) determined the correlation between the hydraulic conductivity and the stress condition of fractures from the in-situ stress and hydraulic response data extracted from boreholes of three different sites. Fractures under the

critically stressed compared to Coulomb failure envelopes usually showed hydraulically conductive behavior, indicating that the dilatancy by the shear displacement could induce a permeability increase.

On the laboratory scale, Yeo et al. (1998) performed flow tests through artificial rock fracture replicas. Before the flow tests, shear displacement was applied to the rock fracture replicas under constant normal load, and the aperture distribution was measured under different shear displacements. In the flow tests, the hydraulic aperture was also obtained by shear displacement. The fracture aperture with increasing shear displacement became heterogeneous and significant, increasing permeability in the direction perpendicular to the shear displacement.

Min et al. (2004) numerically investigated the combined effects of normal deformations and shear dilation on the permeability of fractured rock. The various stress conditions were applied on the two-dimensional DEM model containing the discrete fracture network. The increase in the fracture aperture under high differential stress became significant due to the shear dilation, while the models under low differential stress accompanied the normal closure of the fracture aperture.

In this research, fracture transmissivity is calculated from the simulated mechanical aperture and cubic law without a hydraulic analysis. The fluid density and viscosity for cubic law are assumed to be 1,000 kg/m³ and 1 cP, respectively. For the fully coupled thermo-hydro-mechanical analysis, the fluid density and viscosity tend to be treated as temperature-dependent variables (Hodgkinson et al., 1983). However, the numerical model in this research considers these properties as a constant value to concentrate on the fracture transmissivity changes according to the mechanical behavior of fractures.

Chapter 4. Geological and geomechanical data of Äspö HRL

4.1 Model descriptions

4.1.1 Äspö Hard Rock Laboratory

Äspö HRL is an underground research facility located in the Simpevarp area in the municipality of Oskarshamn, Sweden. This facility was designed as a preparation for a deep geological repository for final disposal of spent nuclear fuel (SKB, 2013). Since the Äspö HRL program was undertaken in 1986, various geological, hydro-geological, geo-mechanical, and geo-chemical field tests have been performed to understand the realistic and undisturbed host rock at the repository depth to develop the appropriate testing methods to characterize the candidate sites and demonstrate the long-term performance of the designed repository system. The deepest part of Äspö HRL is located at a depth of 460 m, and the total length of the entire tunnel is about 3,600 m.

In this research, the TAS04 tunnel in Äspö HRL is adopted as a demonstration target (Figure 4.1). The TAS04 tunnel was excavated through the N50W direction at a depth of 409 m and is selected as the research area for understanding the hydro-geological behaviors of the EDZ. The TAS04 tunnel was excavated using the drill & blast method, and the blast-induced damage was of prior interest to characterize using geophysical observation and hydro-geological in-situ tests (Figure 4.2). Ericsson et al. (2015) captured the geometry of the fracture networks at the vicinity

of the tunnel floor by the ground penetration radar observations.

Figure 4.1 Schematic layout of the Äspö Hard Rock Laboratory, Sweden (modified from SKB, 2013)

To understand the fluid pathway through the fracture networks generated after the excavation, the interference tests were performed among the 42 boreholes excavated on the tunnel floor (Figure 4.3). Each borehole is 1~2 m deep and monitored the hydraulic pressure response by depth interval during the interference tests. Apart from the fracture connectivity, the equivalent transmissivity was measured by depth from the flowrate and pressure drop extracted from the interference test (Figure 4.4). The transmissivity showed a significant increasing trend at the shallow depth up to five-order, which indicates the effects of the blast- and stress-induced EDZ.

Figure 4.2 Photograph showing the TAS04 tunnel taken from the tunnel entrance (Ericsson et al., 2015)
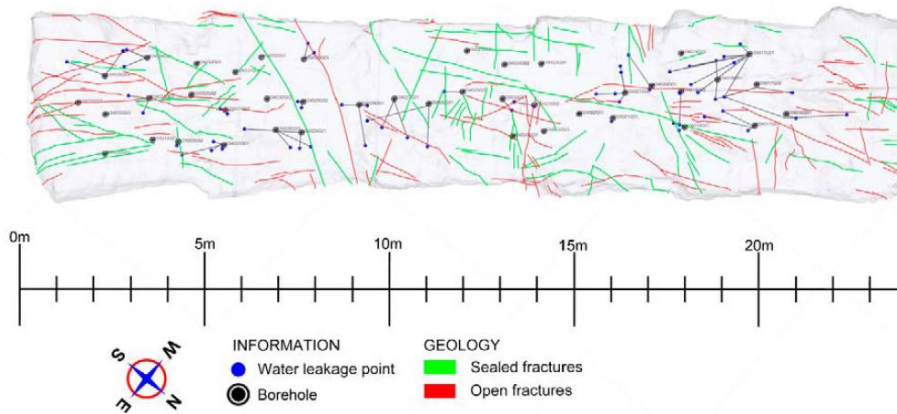
Figure 4.3 Mapped fractures on the floor of the TAS04 tunnel obtained by the injection tests (Ericsson et al., 2015)
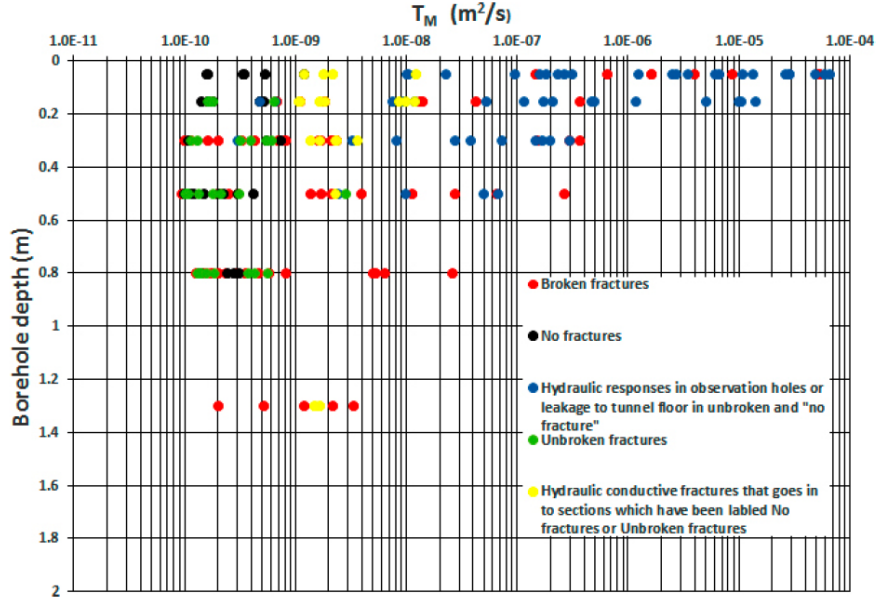
Figure 4.4 Section transmissivity by depth grouped by the mapped type of fractures in the TAS04 tunnel (Ericsson et al., 2015)

4.1.2 Three-dimensional tunnel model

For the demonstration of the three-dimensional tunnel model, the numerical model is constructed with a size of 32 m x 50 m x 50 m (Figure 4.5). At the center of the model, a horseshoe-shaped tunnel is located. The tunnel surface is assumed to be a mechanically and thermally free surface without the explicit structure of backfill materials. The geometry of the tunnel model is based on the point cloud data of the TAS04 tunnel surfaces, and the tunnel wall and floor are assumed as smooth and flat surfaces. The tunnel is 5.5 high, 5.3 m wide, and 32 m long. The edge size of the zones comprising each block is 0.6 m at the vicinity of the tunnel and enlarged at the domain far from the tunnel up to 4.2 m.
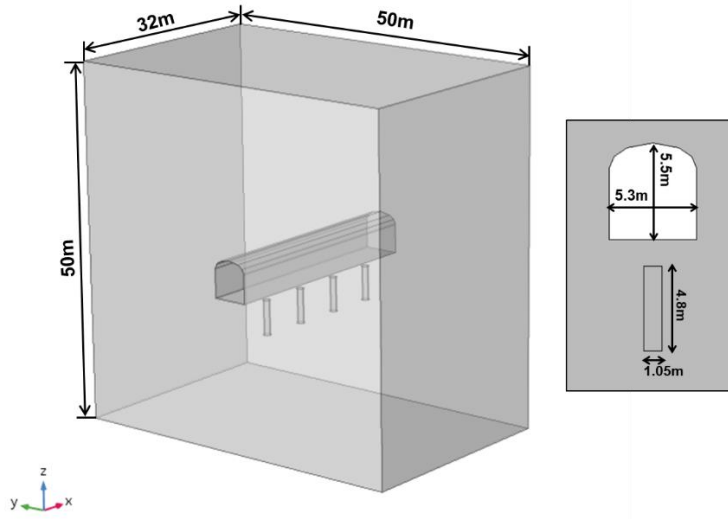
Figure 4.5 Schematic geometry of the three-dimensional numerical model with the horseshoe-shaped tunnel and four canisters. The x axis corresponds to the tunnel axis (N50W).

The tunnel penetrates the model along the x axis, which is parallel to the NW-SE direction of the maximum horizontal stress. The depth-dependent boundary stress conditions are applied on the numerical model based on the measurement at the Äspö HRL (Christiansson and Janson, 2003). The magnitude of the in-situ stress is as follows:

$$\sigma_x = 12 + 0.0295z \ (\text{MPa}) \tag{4.1}$$
$$\sigma_y = 0.0295z \ (\text{MPa}) \tag{4.2}$$
$$\sigma_z = 0.0295z \ (\text{MPa}) \tag{4.3}$$

where σ_x, σ_y, σ_z is the in-situ stress in x, y, z directions, respectively, and z is the depth in meters. At the tunnel floor, with a depth of 409 m, the vertical stress and

minimum horizontal stress are 12.07 MPa, and the maximum horizontal stress is

24.07 MPa (Figure 4.6).
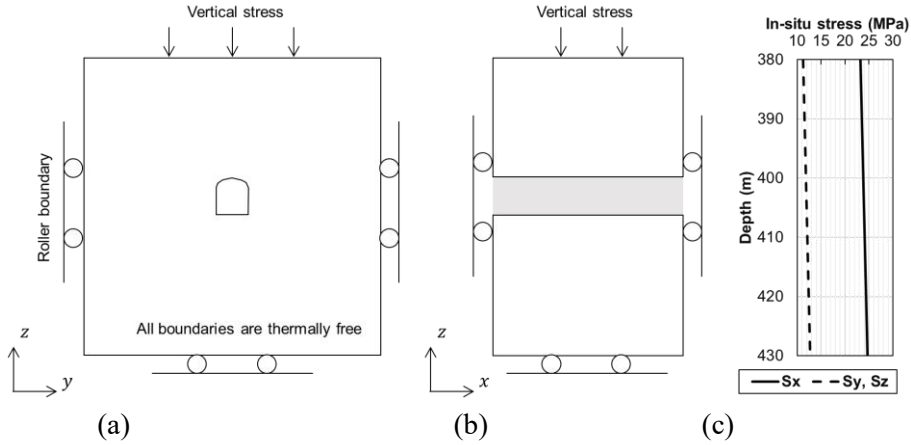
Figure 4.6 Boundary conditions of three-dimensional numerical models in (a) yz cross-section and (b) xz cross-section, and the in-situ stress conditions applied on the models

4.1.3 Fracture geometry

To model the fractured rock around the TAS04 tunnel in Äspö HRL, the

deterministic discrete fracture networks (DFN) are modelled based on the two

fracture sets, the steep NW striking set, and gently dipping NNW set, as observed

from the borehole excavated at the TAS04 tunnel floor (Ericsson et al., 2015). The

fracture population is described statistically in terms of probability distributions for

fracture size, orientation, and density. The fractures intersecting the tunnel floor

match the observed geometry of the mapped fracture from the TAS04 tunnel. The

number of constructed discrete fractures is 61,019 in a 50 m x 50 m x 50 m volume

(Meier and Backers, 2020).

This research concentrates on understanding the fracture transmissivity change

around the tunnel, so only the open fractures near the tunnel are considered. Seventy-one fractures are selected from the deterministic DFN (Figure 4.7), which directly connect to the tunnel floor and the borehole in the TAS04 tunnel (red color in Figure 4.7) and indirectly connect to the tunnel floor and the borehole through a single fracture (blue color in Figure 4.7). The fractures are assumed as circular planes with the appropriate diameter according to the size distribution.
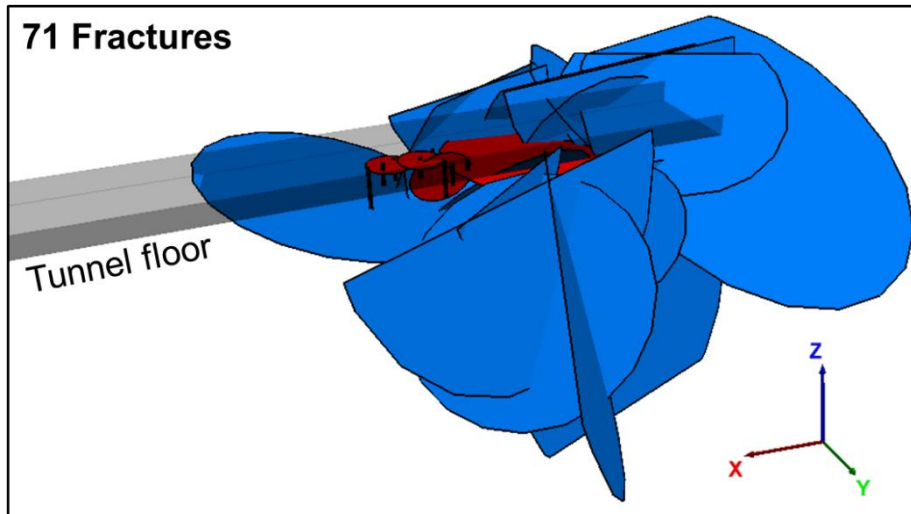
Figure 4.7 Selected 71 fractures included in the three-dimensional discrete element model. The black lines are the boreholes in the TAS04 tunnel, the red fractures are directly connected to the tunnel floor, and the blue fractures are indirectly connected to the tunnel floor through the red fractures.

4.2 Properties

4.2.1 Mechanical and thermal properties of the host rock

The rock mass around the TAS04 tunnel is dominated by the three main rock types; fine-grained granite, Äspö diorite and Ävrö granodiorite (Ericsson et al., 2015), which show the mechanical properties of the typical hard and brittle behaviors of the igneous crystalline rock. The mechanical and thermal properties extracted from the lab tests with the rock specimen are shown in Table 4.1.

Table 4.1 Mechanical and thermal properties of the host rock (Anderssson, 2007; Hakami et al., 2008)

Properties	Unit	Value
Elastic modulus	GPa	76.0
Shear modulus	GPa	30.4
Density	kg/m^3	2750
Thermal conductivity	W/mK	2.60
Specific heat	J/kgK	764
Thermal expansion coefficient	K^{-1}	7.0E-6

4.2.2 Mechanical characteristics of fractures

The aim of the simulation in this research is to quantify the transmissivity changes on the fractures induced by external effects. Characterizing the mechanical behaviors of the fractures is the most important issue for achieving the objectives. Similar to the rock properties, the numerical models include the fracture properties measured by the lab tests using the specimens from the Äspö HRL and Laxemar site. The mechanical properties of the fractures adopted for the numerical simulations are shown in Table 4.2.

Table 4.2. Mechanical properties of the fracture (Hakami et al., 2008; Fransson, 2009; Hökmark et al., 2010; SKB, 2010c)

Properties	Unit	Value
Joint normal stiffness	GPa/m	7.0 ~ 4830
Joint shear stiffness	GPa/m	39
Dilation angle	°	3.7 ~ 25.7
Joint cohesion	MPa	0.9
Joint friction angle	°	36.6
Zero stress aperture	μm	30
Maximum aperture	μm	1000
Residual aperture	μm	5
JKN*	GPa/m	367
JEN*		0.86
Joint roughness coefficient**		6.66
Joint wall compressive strength**	MPa	72.98

*JKN and JEN are the parameters in the continuously-yielding joint model (Itasca, 2013)

**Estimated by the relation between the applied normal stress and dilation angle from Barton and Choubey (1977)

At the Laxemar site, the direct shear tests and tilt tests were conducted to characterize the mechanical properties of the rock fractures (Hakami et al., 2008). The direct shear tests were conducted with 0.5, 5, and 20 MPa of the applied normal stress on the fractures, and the stiffness and the dilation angle of fractures were measured by the applied stress. Especially, the normal stiffness and the dilation angle of fractures, which are the mechanically important parameters dominating the change of the fracture aperture, showed a dependency on the applied normal stress. Hökmark et al. (2010) suggested the non-linear normal stiffness model according to the cyclic compression tests from the Laxemar specimens (Figure 4.8). The non-linear stiffness-stress relation is based on the continuously yielding joint model from Itasca (2013) according to the two parameters controlling the hyperbolic curves (Eq. (4.4)).

$$K_n = JKN \, \sigma_n^{JEN}, \tag{4.4}$$

where K_n is the joint normal stiffness, JKN is the stiffness at 1 MPa of normal stress, JEN is the joint normal stiffness exponent, and σ_n is the normal stress applied on the joint surface.
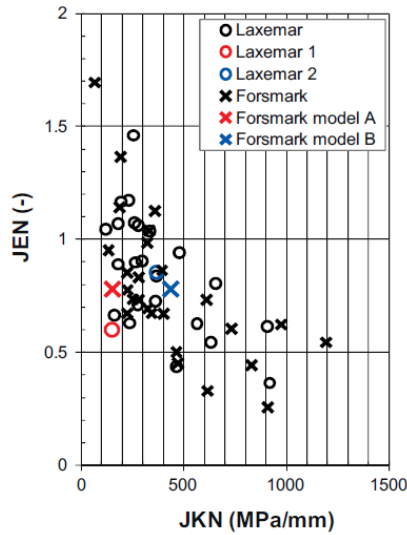
Figure 4.8 (a) JKN and JEN parameters for the continuously yielding model obtained from cyclic compression tests of samples from the Laxemar and Forsmark sites (Hökmark et al., 2010)
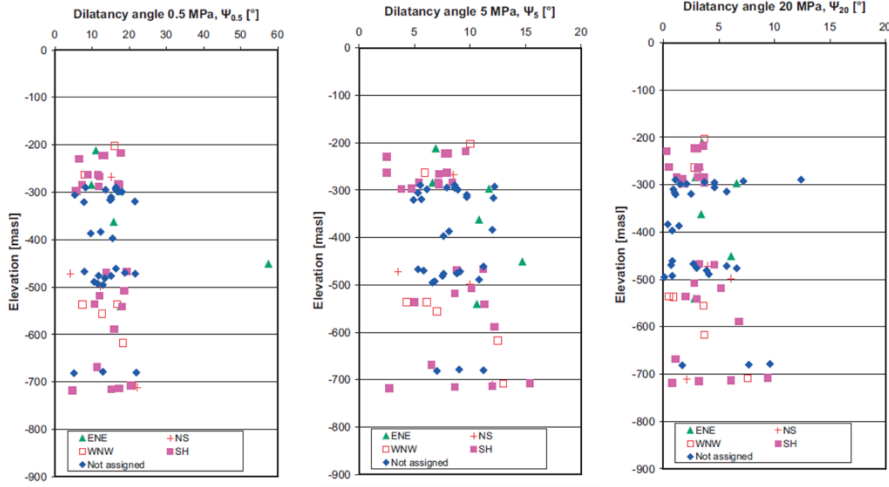
Figure 4.9 Dilation angle by elevation under 0.5, 5, and 20 MPa of normal stress applied on the fracture specimen extracted from the Laxemar site (Hakami et al., 2008)

The fracture dilation angle also showed significantly stress-dependent characteristics from the Laxemar samples lab tests (Figure 4.9) (Hakami et al., 2008). Barton and Choubey (1977) suggested an empirical relationship between the dilation angle and the applied normal stress. The dilation angle data from Laxemar also followed the Barton and Choubey's equation (Eq. (4.5)), and the joint roughness coefficient and the joint wall compressive strength can be calculated from the tendency between the dilation angle and the applied normal stress (Figure 4.10).

$$\phi_d = JRC \cdot \log (JCS/\sigma_n) \tag{4.5}$$

where ϕ_d is the joint dilation angle, JRC is the joint roughness coefficient, and JCS is the joint wall compressive strength.
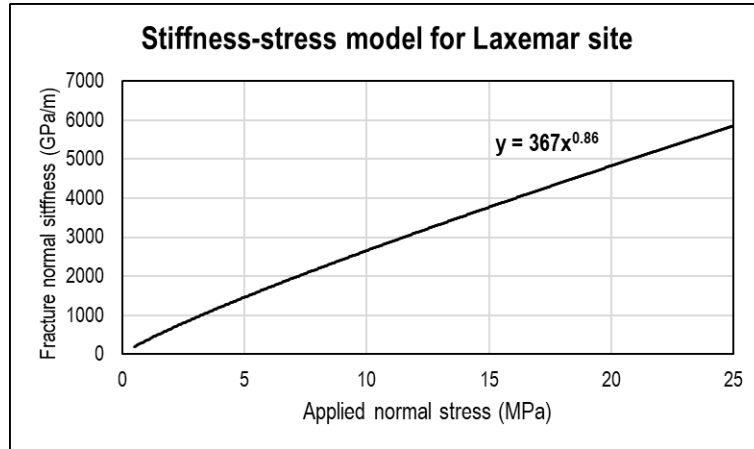
(a)
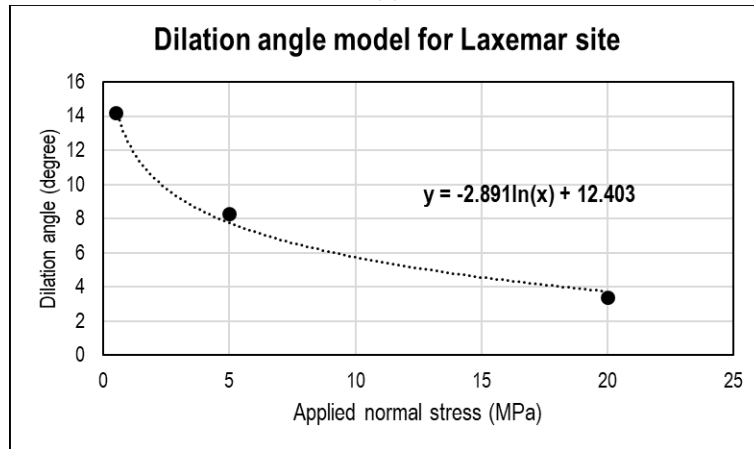
(b)

Figure 4.10 Stress dependent (a) fracture normal stiffness model and (b) dilation angle model based on the observations from the Laxemar site (Hakami et al., 2008)

To control the change of the fracture aperture in the numerical model, the model requires three aperture data inputs: the zero-stress aperture, residual aperture, and maximum aperture. In the numerical model in this research, the fractures have the same aperture model with consistent zero-stress, residual, and maximum apertures. The zero-stress aperture and residual aperture of the fractures are assumed as 30 μm and 5 μm, respectively, based on the stress-dependent aperture model, which SKB (2010c) and Hökmark et al. (2010) adopted according to the transmissivity

observation. To consider the effect of the shear dilation, the maximum aperture needs to be large enough. Fransson (2009) suggested a 1,000 μm of the maximum mechanical aperture based on the borehole observations, and the numerical model in this research uses that maximum aperture as the input data.

Chapter 5. Transmissivity evolution on the Äspö HRL model

5.1 Stress re-distribution by excavation on the Äspö HRL model

A three-dimensional DEM model was constructed with the geo-mechanical characteristics of the fractured rock at the repository depth. At the center of the fractured rock model, a horseshoe-shaped tunnel was constructed with mechanically free boundary conditions. The tunnel induces the stress concentration in a tangential and axial direction and the stress relaxation in a radial direction around the free surface. The stress conditions on the fracture surfaces are also disturbed, and the normal and shear displacements appear based on the change in the stress condition. The normal displacement directly changes the fracture apertures, and the shear displacement also induces the dilation of the fracture aperture according to the dilation angle of the fractures.

The aperture disturbed by the stress re-distribution can be assumed as the in-situ apertures of the tunnel model. In the TAS04 tunnel of Äspö HRL, the transmissivity was captured by depth using the in-situ tests in the boreholes at the tunnel floor. According to cubic law, the disturbed aperture can be calculated as the transmissivity change.

Figure 5.1 Fracture transmissivity distribution by depth under the various fracture normal stiffness including the stress-dependent model

Due to the stress re-distribution on the fractures, the fracture apertures applied as the consistent zero-stress aperture have a wide range of values. The distribution of the fracture transmissivity is plotted with respect to the depth of the center point of fractures (Figure 5.1). In the TAS04 tunnel, the equivalent transmissivity was measured by monitoring the pressure response during the interference tests (Figure 4.4). The in-situ transmissivity showed a wide distribution ranging from 10^{-2} to 10^{-10} m^2/s at the shallow depth and significant increases at the shallow depth compared to the transmissivity at a depth of 411 m ranging from 10^{-8} to 10^{-9} m^2/s. The drastic

change at the shallow depth indicates the existence of the EDZ.

The simulated distribution of the fracture transmissivity can be compared to the in-situ data from the interference tests. To validate the applied stress-dependent normal stiffness and dilation angle, additional models with the constant normal stiffness and dilation angle are prepared. Figure 5.1 shows the fracture transmissivity resulting from the numerical models with 20, 200, and 2000 GPa/m of the constant normal stiffness and the stress dependent normal stiffness without the effect of shear dilation. The effect of the stress re-distribution appears up to 3 m depth from the tunnel floor. The decrease of the normal stiffness significantly induces the wide range of the transmissivity distribution, indicating that the fractures located at the vicinity of the tunnel tend to be highly affected by the normal stress relaxation.

Compared to the constant normal stiffness, the stress-dependent normal stiffness can describe the drastic changes of the transmissivity by depth more realistically. Among the constant normal stiffness models, the 200 GPa/m model provides the most similar results to the field data. At the shallow depth, the stress-dependent normal stiffness model results in transmissivity distribution ranging from 10^{-5} to 10^{-9} m^2/s, whereas the model with a constant stiffness of 200 GPa/m results in a range from 10^{-7} to 10^{-9} m^2/s. Meanwhile, the transmissivity distribution at 411 m depth ranges from 10^{-7} to 10^{-9} m^2/s in both the stress-dependent normal stiffness model and the 200 GPa/m of constant normal stiffness model.
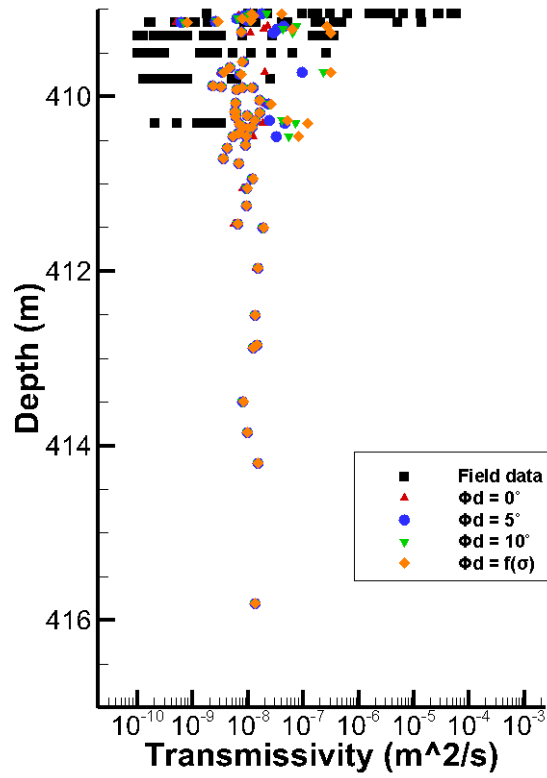
Figure 5.2 Fracture transmissivity distribution by depth under various fracture normal stiffnesses, including the stress-dependent model

Figure 5.2 shows the disturbed fracture transmissivity of the numerical models with 0°, 5°, and 10° of dilation angle and the stress-dependent dilation angle under the constant normal stiffness of 2000 GPa/m. The increase of the dilation angle also induces an increase of the fracture transmissivity, but the effect of the dilation angle does not appear on every fracture. The transmissivity change induced by the shear dilation is significant at the shallow depth, which indicates that the fractures nearby the tunnel surface are vulnerable to the shear slip. Also, the stress-dependent normal stiffness model with the stress-dependent dilation angle easily describes the drastic

change of the in-situ transmissivity by depth. In particular, at the vicinity of the tunnel, the stress-dependent dilation angle can provide a 10 times larger transmissivity increase than the 10° of constant dilation angle model. According to a comparison of the various normal stiffness and dilation angle models, the stress-induced transmissivity changes at the vicinity of the tunnel should be considered as the combined mechanisms of the normal deformations and shear slip.
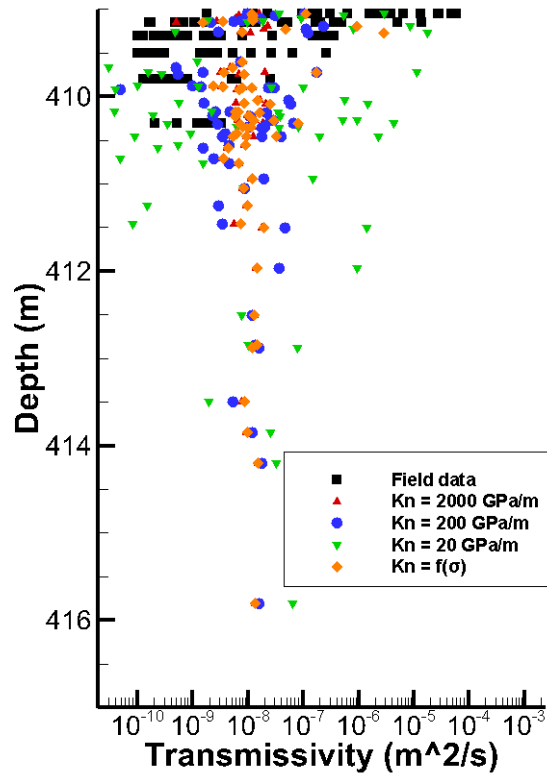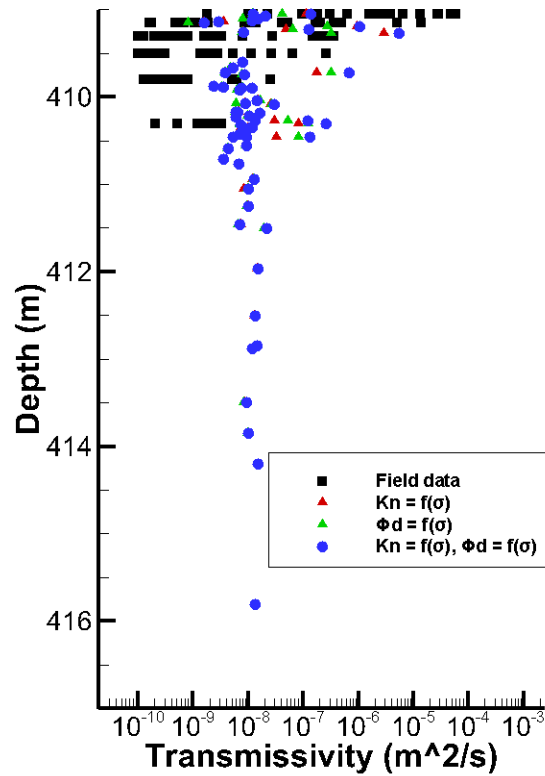

Figure 5.3 Fracture transmissivity distribution by depth under the various fracture normal stiffness including the stress-dependent model

Figure 5.3 shows the simulation results of the model with the stress-dependent normal stiffness and dilation angle. With the stress-dependent fracture properties, the drastic changes of the equivalent transmissivity from the in-situ tests can be

described. According to the numerical simulations, the stress re-distribution by the tunnel excavation accompanies the aperture opening for 23% of fractures at the depth up to 2.5 m from the tunnel floor, and 6% of fractures show a one-order increase of the transmissivity compared to the initial transmissivity at a depth up to 1.3 m. The effect of the stress re-distribution disappears from the fracture 3 m apart from the tunnel floor.

The effect of the stress re-distribution on the fracture aperture is highly related to the orientation and size of the fracture. After the excavation, the fracture parallel to the tunnel surface is released due to a reduction in the normal stress and is highly affected by the normal opening and the decrease of the normal stiffness, which can make the normal deformation drastic. In cases where of the fractures are perpendicular to the tunnel surface, the concentration of the tangential stress applies the additional normal stress on the fracture surfaces, induces the normal closure, and reduces the effect of the shear dilation due to a decreased dilation angle. The fractures inclined from the tunnel surfaces at the vicinity of the tunnel get the effects of the tangential stress concentration and radial stress relaxation simultaneously. The different trends of the stress changes induce the high shear stress that accompanies the fracture dilation, and the amount of shear dilation is dominated by the applied normal stress that controls the dilation angle.

The constructed numerical model with the stress-dependent fracture properties can describe the overall transmissivity distribution in the TAS04 tunnel. Both normal deformations and shear dilation compose the aperture changes, and the stress-dependent parameters dominate the aperture change amount, especially at shallow depths.

5.2 Thermal loading on the Äspö HRL model

5.2.1 Descriptions of heat source

Disposed HLW in the canister continuously emits heat during the lifetime of the geological repository. Even though the heat decays by time, the temperature increase induced by the HLW can disturb the stress conditions of the natural barrier. The following power decay model (Eq. (5.1)) was used for the disposed canister based on the burn-up of the fuel and the interim storage time (Figure 5.4) (Hökmark et al., 2009).

$$P(t) = \sum_{i=1}^{7} a_i \exp(-t/t_i), \hspace{3cm} (5.1)$$

where $P(t)$ is the normalized canister power t is time after deposition, t_i are the time constants, and a_i are the decay-coefficients, which are presented in Table 5.1.

Table 5.1 Decay-coefficients for the reference fuel (Hökmark et al., 2010)

i	t_i(years)	a_i
1	20	0.060147
2	50	0.705024
3	200	-0.054753
4	500	0.249767
5	2,000	0.025408
6	5,000	-0.009227
7	20,000	0.023877
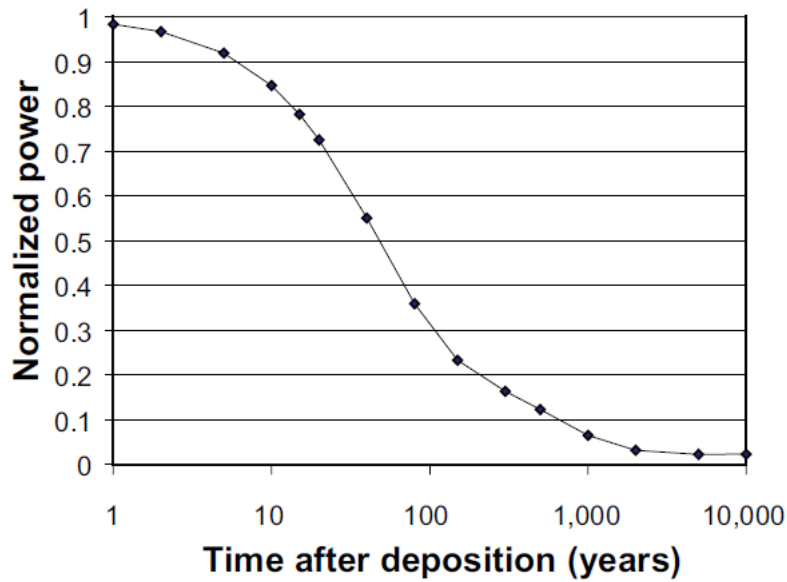
Figure 5.4 Normalized power functions by time after deposition (Hökmark et al., 2009)

In this research, four canisters with 1700 W of the initial power and the normalized power decay model shown above are considered in the numerical model. To represent the canister, a heat source of 4.8 m in height and 1.05 m in diameter were placed 1.5 m below the center line of the tunnel floor. Each heat source was placed 7 m apart along the tunnel axis. The applied initial temperature of the host rock was 11.5°C, and all boundaries were assumed to be thermally free. According to the thermal simulations, the maximum temperature generated by the canister model reaches 54.5°C at 0.5 m away from the canister (Figure 5.5) five years after the deposition. At the end of the 50,000-year simulations, the heat totally dissipates, and the temperature recovers to the initial temperature (Figure 5.6).
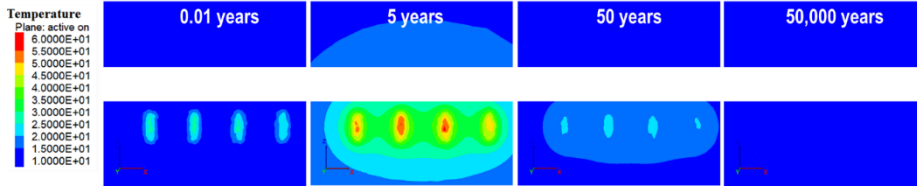
Figure 5.5 Temperature distribution around the tunnel
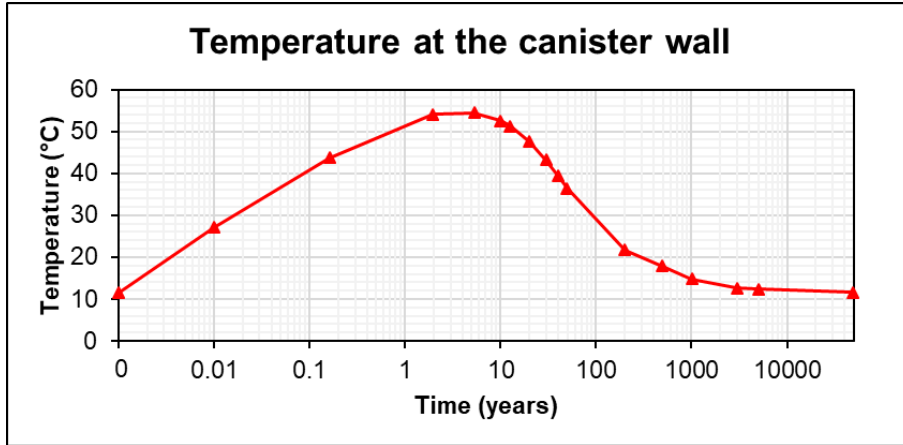
Figure 5.6 Transient temperature change at the canister wall in the numerical model

5.2.2 Results of thermal simulations

After the simulations of stress re-distribution on the fractured rock model, the thermo-mechanical simulations were performed with the constructed canister models. The transient aperture data on the fracture surfaces was monitored during the 50,000-year thermal scenarios. In Figure 5.7, the ratio between the transmissivity induced by the thermal loading and the initial transmissivity after the excavation was plotted by depth for 71 fractures. Two situations were selected to analyze the thermally induced transmissivity change: 5 years and 50,000 years after the deposition which show the peak of the temperature and the fully dissipated temperature, respectively. At the peak temperature, the transmissivity of fractures

64

tends to decrease due to the compressive thermal stress applied through the tangential and axial directions. The fracture transmissivity is distributed from 0.53 to 2.0 times of the initial transmissivity, and 15% of the fractures showed the increased transmissivity. Although the temperature increase entails an additional thermal load on the fracture surfaces induced by the temperature increase, the dilation effect from the shear slip appears on the fractures of which the shear stress also increases due to the anisotropic stress change depending on the fracture orientation.

In the final stage of the thermal scenario, 28% of the fractures showed increased transmissivity, and the transmissivity ratio ranged from 0.56 to 3.4. Since the effect of the temperature disappeared, the normally deformed fractures recovered to their initial conditions, and the overall transmissivity of the fractures tended to increase. However, the dilated aperture due to the shear slip remained irreversibly after cooling, so 28% of the fractures kept a permanent increase of transmissivity. The spatial extent of the dilated fracture was up to around 3 m from the tunnel floor.
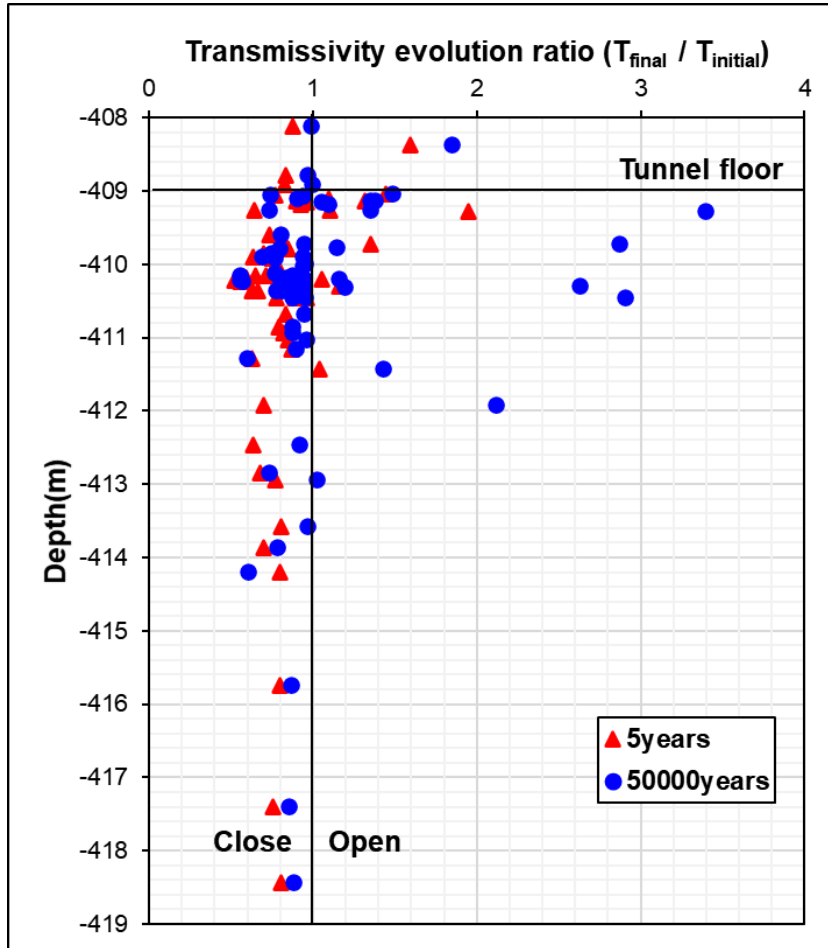
Figure 5.7 Ratio of the average transmissivity evolution on fractures by depth for 5 years and 50,000 years after deposition

To determine the detailed mechanism of fractures during the thermal scenario, two fractures were selected for monitoring the normal and shear stresses (Figure 5.8). Fracture #32 is the fracture perpendicular to the tunnel axis with 89° of dip and 43° of dip direction, and Fracture #60 is the inclined fracture with 44° of dip and 287° of dip direction.
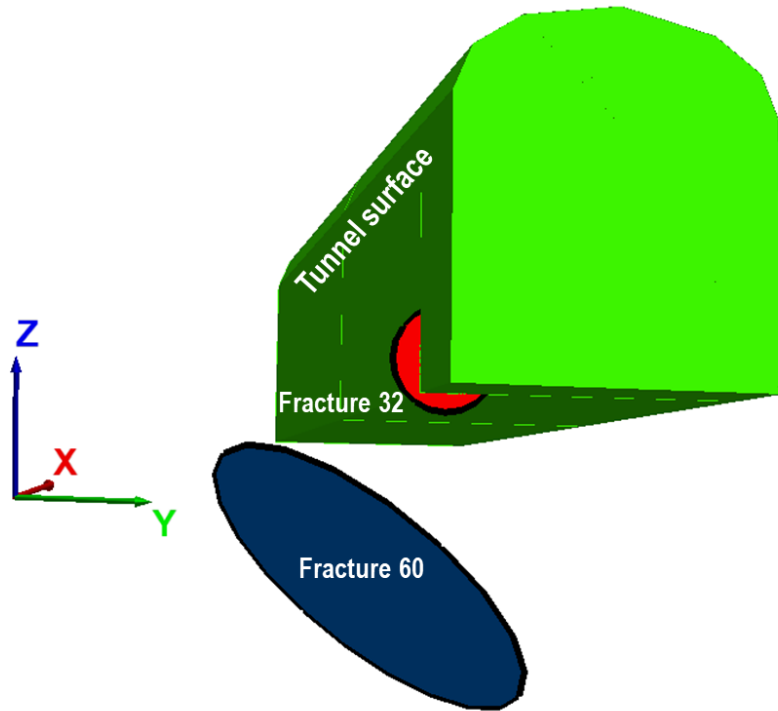
Figure 5.8 Geometry of Fracture #60 (Blue) and Fracture #32 (Red) on the tunnel surface

Figure 5.9 is the stress path and the transmissivity of Fracture #32 during the entire thermal scenario. Fracture #32 shows reversible transmissivity changes due to the increase and decrease in temperature. In the stress path of Fracture #32, the simple increase and decrease of the normal stress without a change in shear stress appeared, so the shear slip cannot occur on Fracture #32.
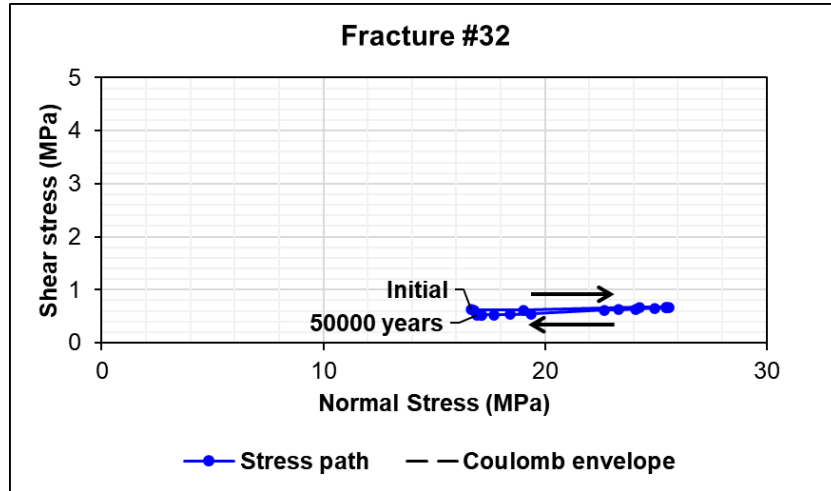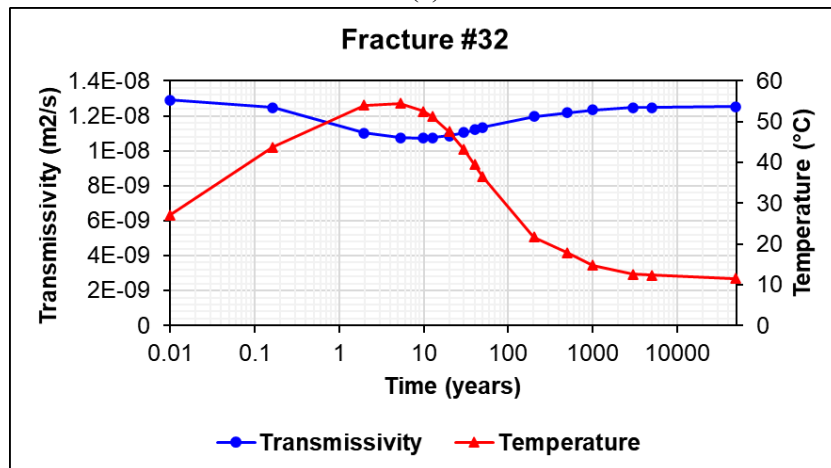
Figure 5.9 (a) Stress path and (b) transmissivity change on Fracture #32 during the thermal loading

In Figure 5.10, the transient transmissivity and the stress path on Fracture #60 are depicted. The transmissivity of Fracture #60 increased irreversibly during the thermal scenario, which indicates the possibility of shear dilation. The stress condition of Fracture #60 is vulnerable at the initial state and reaches the Coulomb failure envelope during the heating cycle. In the transient transmissivity, the effect of the shear dilation during the heating cycle did not appear due to the thermally

induced normal closure. During the cooling cycles, the reversible normal deformation dissipates, and the permanent transmissivity increase caused by the irreversible shear dilation only remained.

(a)

(b)
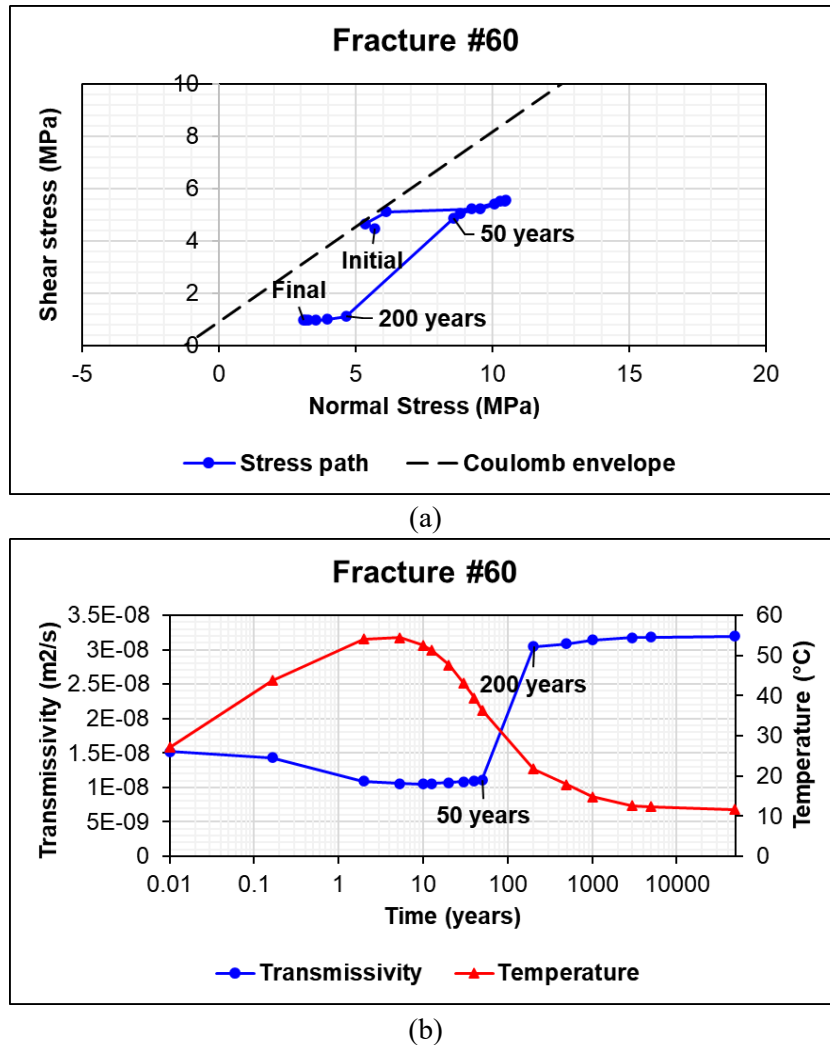
Figure 5.10 (a) Stress path and (b) transmissivity change on Fracture #60 during the thermal loading

According to the simulations on the fractured rock model, the mechanical behaviors of fractures under the thermal loading can be identified in two categories;

the reversible transmissivity change caused by the normal deformations and the irreversible transmissivity increase caused by the shear dilation. The reversible behaviors appear on the fractures perpendicular or parallel to the tunnel surfaces due to the small amount of the shear stress concentration. The irreversible transmissivity increase can be found on the inclined fractures, which are already vulnerable to shearing and receive the high shear stress induced by thermal loading, especially at the shallow depth.

5.3 Glaciation on the Äspö HRL model

5.3.1 Descriptions of the glaciation scenario

Glaciation is considered an important issue that can affect the performance of geological repositories in northern Europe (Lund et al., 2009; Hökmark et al., 2010). Lund et al. (2009) tried to predict the growth and retreat of ice sheets in the Scandinavian area and the orientation and magnitude of glacially induced stress. According to the prediction, two glacial maximums with about 2 and 3 km thickness of the overburdened ice sheets can appear at 12,000 and 54,500 years after the deposition of the HLW, respectively. Each glacial maximum induces about 16 and 27 MPa of overburden stress, with horizontal stress at the repository depth following the increase of vertical stress. After the ice sheet retreat, the vertical stress recovers to its initial condition directly, while the horizontal stress follows the recovery slowly.
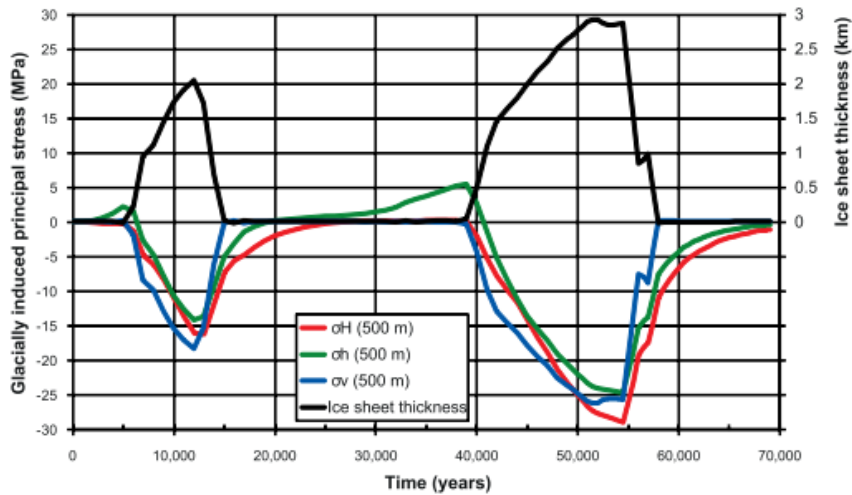
Figure 5.11 Estimated ice sheet thickness and glacially induced principal stresses at the repository depth during the Weichselian glacial cycle (Hökmark et al., 2010)

The detailed expectations of glacially induced principal stress at the repository depth are shown in Figure 5.11. The induced principal stress is converted along the axis of the numerical model (Table 5.2). The converted stress in each glacial stage is applied on the upper and lateral boundaries of the numerical model.

Table 5.2 Boundary conditions of the glacially induced stresses applied on the numerical models

		Time (years)					
		12000	15000	39000	54500	58000	70000
Glacially Induced Stress (MPa)	σ_x	-14.9	-6.8	2.1	-26.6	-10.1	0
	σ_y	-15.6	-5.7	3.0	-27.2	-8.8	0
	σ_z	-18.4	-0.3	-0.4	-25.8	0.2	0
	τ_{xy}	0.8	1.1	-2.7	2.0	1.5	0

(- : compressive)

5.3.2 Results of glacial simulations

The overburden stress during the glaciation scenario was transformed to the boundary conditions at the repository depth, as compiled in Table 5.2. The glacial stress was applied to the boundaries of the numerical models, and the mechanical behaviors of the fractures at each stage were captured. To determine the irreversibility of the transmissivity, this research focused on comparing each glacial maximum stage (12,000 and 54,500 years) and recovery stage (39,000 and 70,000 years).
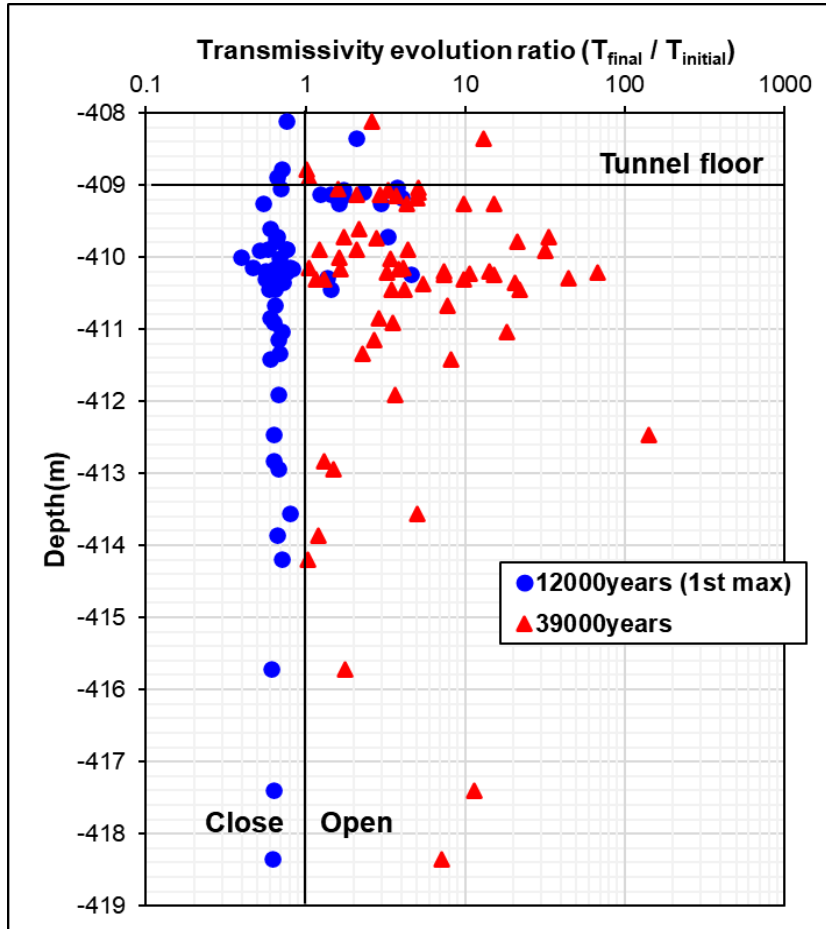
Figure 5.12 Ratio of the average transmissivity evolution on fractures by depth during the first glacial maximum

During and after the first glaciation, the average transmissivity was captured for all fractures in Figure 5.12. At the first glacial maximum, most of the fractures were closed due to glacially induced compression, and only 24% of fractures were dilated. After the first glaciation retreats, 97% of fractures showed increased transmissivity, and the effect of the glaciation appeared up to 9 m in depth from the tunnel floor as one-order transmissivity increased and up to 4 m depth as two-order transmissivity increased. The transmissivity evolution ratio of fractures was distributed ranging from 0.40 to 4.6 at the first glacial maximum and 1.0 to 140 times

at the end of the first glaciation.
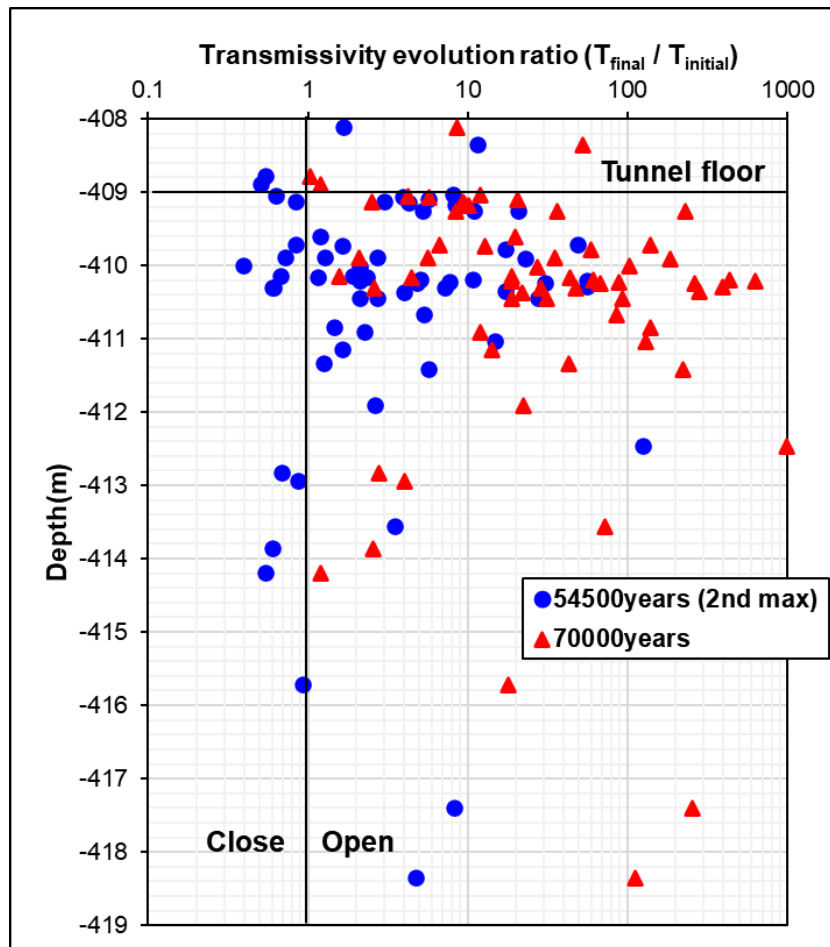
Figure 5.13 Ratio of the average transmissivity evolution on fractures by depth during the second glacial maximum
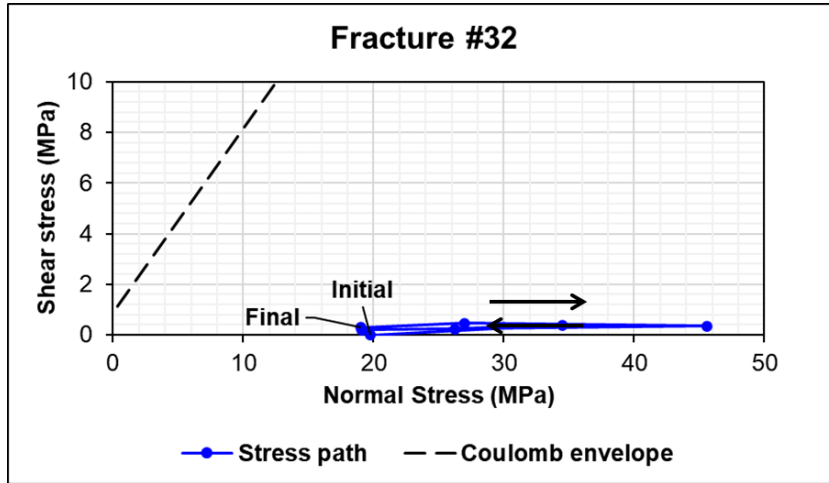
(a)
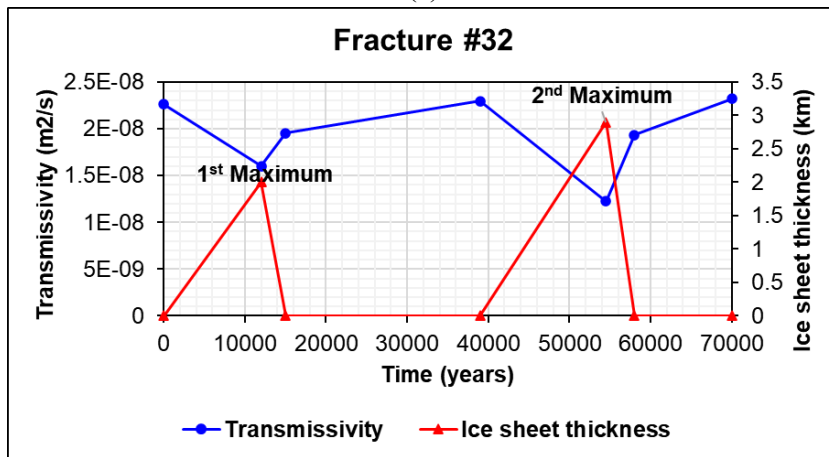
(b)

Figure 5.14 (a) Stress path and (b) transmissivity change on Fracture #32 during the glaciation

In Figure 5.13, the transmissivity changes during the second glaciation are plotted by fracture depth. Under the second glacial maximum, 51% of fractures showed a transmissivity increase compared to the initial condition. At the end of the second glaciation, 100% of fractures accompanied an increase in the average transmissivity. The glacially induced transmissivity increase appeared up to 10 m in depth as a two-order change and 4 m depth as a three-order change. The distribution

of the transmissivity ratio ranged from 0.40 to 130 times at the second glacial maximum and 1.0 to 990 times at the end of the second glaciation.

During all glaciation scenarios, the stress conditions for each fracture were also monitored. As shown in Figure 5.14, Fracture #32 closes and recovers its initial transmissivity reversibly according to the growth and retreat of the ice sheet. The stress path of Fracture #32 also shows the exclusive change of the normal stress without the shear stress change.

In Figure 5.15, the stepwise transmissivity increases for Fracture #60 are described. The transmissivity slightly decreased at the first and second glacial maximum due to the high normal stress concentration as shown in the stress path. After the glaciation retreats, the fracture transmissivity increased over the initial conditions, and the increased transmissivity remained at the end of the entire scenario. The stress path at the unloading cycles also reaches the Coulomb failure envelop, which significantly indicates the shear slip. Especially 58,000 years after the deposition, the whole glacial vertical stress disappears while the glacial horizontal stress partly remains (Lund et al., 2009). This anisotropic glacial stress can generate the shear stress on the fractures throughout the model.

Same as in the thermal scenarios, the fractures are categorized in two kinds of mechanical behaviors depending on the orientation of the fractures. The fractures perpendicular or parallel to the tunnel surface are dominated by the normal deformations, which induce a reversible transmissivity change. On the other hand, the fractures inclined from the tunnel surfaces received a high shear stress concentration induced by the glaciation, and the permanency of the transmissivity increase appears to result from the shear dilation (Figure 5.16).
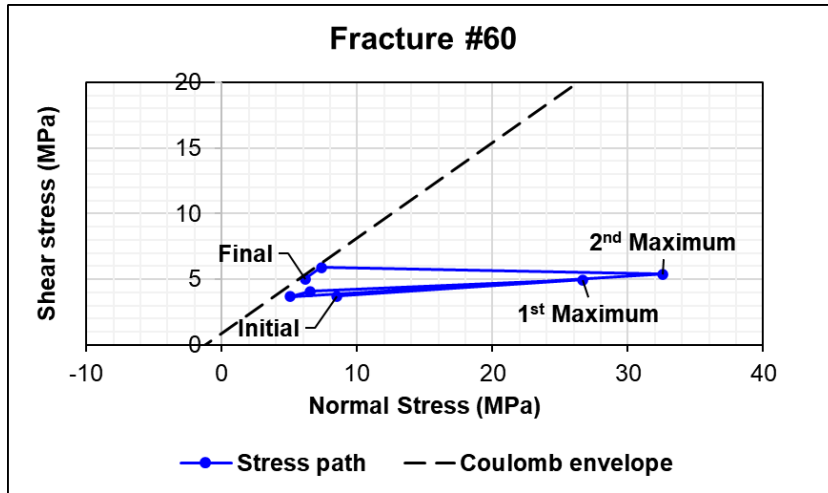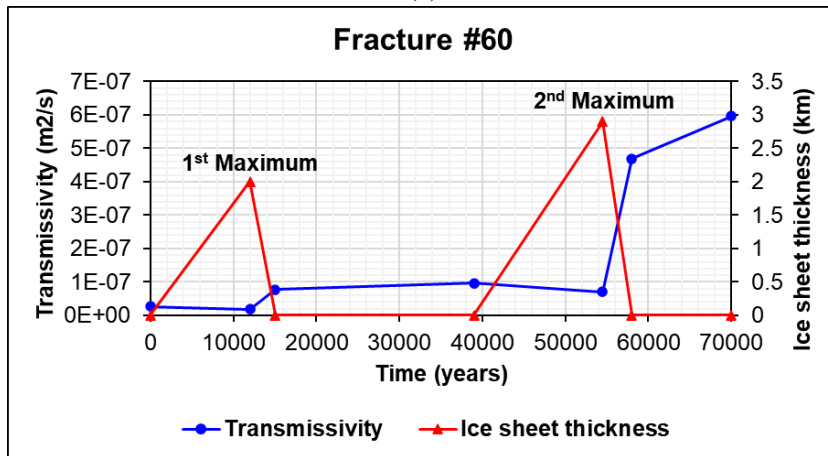
Figure 5.15 (a) Stress path and (b) transmissivity change on Fracture #60 during the glaciation
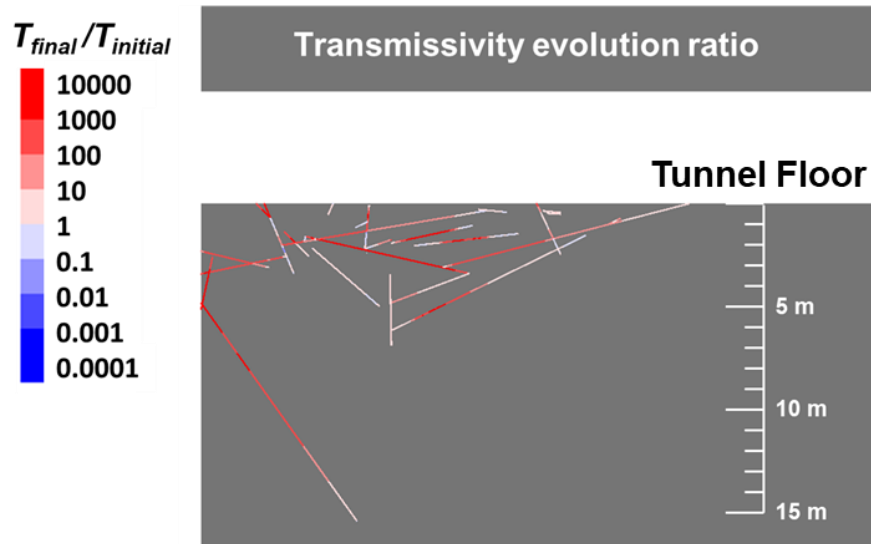
Figure 5.16 Distribution of transmissivity evolution ratio on the cross-section of model at the end of glacial scenario

5.4 Earthquake on the Äspö HRL model

5.4.1 Descriptions of earthquake models

SKI (1992) constructed synthetic ground motion histories predicting the ground response of nuclear structures under earthquake scenarios with extremely low probability level. The project specified the probability levels in frequencies of 10^{-7}, 10^{-6}, and 10^{-5} annual events per site, and characterized the ground motion models using ground response spectra and synthetic ground motion histories. The modelled ground motion histories by frequency were transient acceleration, velocity, and displacement histories in three directions perpendicular to each other. Figure 5.17 shows the ground velocity histories in three directions for a frequency of 10^{-7} annual events, which represents the shear-wave of near-field earthquakes with magnitudes of $5 \sim 6$ at typical hard rock sites.

The constructed three-dimensional synthetic ground velocity histories are converted to the normal and shear stresses to be applied at the bottom boundary surfaces of the numerical model. Assuming that the dynamic stress is applied to the bottom xy plane, the vertical wave with an oscillation parallel to the propagating direction is converted to the transient normal stress histories, while the horizontal waves are converted to the shear stress histories according to the relation in Eq. (5.2) $\sim$ (5.4) (Itasca, 2013).

Vertical

Horizontal 1
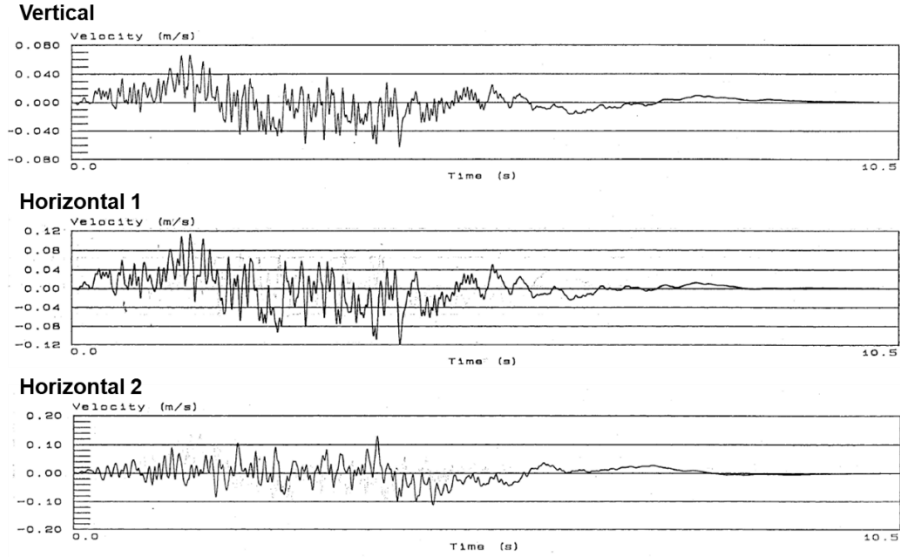
Horizontal 2

Figure 5.17 Vertical and horizontal ground velocity histories for the 10^{-7} annual event model (modified from SKI, 1992)

$$\sigma_{zz} = \rho C_p v_v \qquad\qquad (5.2)$$
$$\tau_{xz} = \rho C_s v_{h1} \qquad\qquad (5.3)$$
$$\tau_{yz} = \rho C_s v_{h2} \qquad\qquad (5.4)$$

where σ is the boundary normal stress, τ is the boundary shear stress, ρ is the density of medium, C_p is the P-wave velocity of medium, C_s is the S-wave velocity of medium, and v is the ground velocity histories. The P- and S-wave velocities of the host rock can be calculated from the elastic properties in Table 4.1 according to Eqs. (5.5) and (5.6) (Itasca, 2013).

$$C_p = \sqrt{\frac{K + (4/3)G}{\rho}} \qquad\qquad (5.5)$$
$$C_s = \sqrt{G/\rho} \qquad\qquad (5.6)$$

where K is the bulk modulus and G is the shear modulus of the rock.

To describe the far-field rock mass at the model boundary, the viscous boundary conditions are applied to all boundary surfaces. In particular, the lateral boundaries parallel to the wave propagating direction are assumed to be the dynamic free-field boundaries, which consist of a one-dimensional finite-difference calculation (Figure 5.18). Those boundary conditions can absorb the seismic wave and prevent the reflections at the boundary surfaces.

(a)   (b)
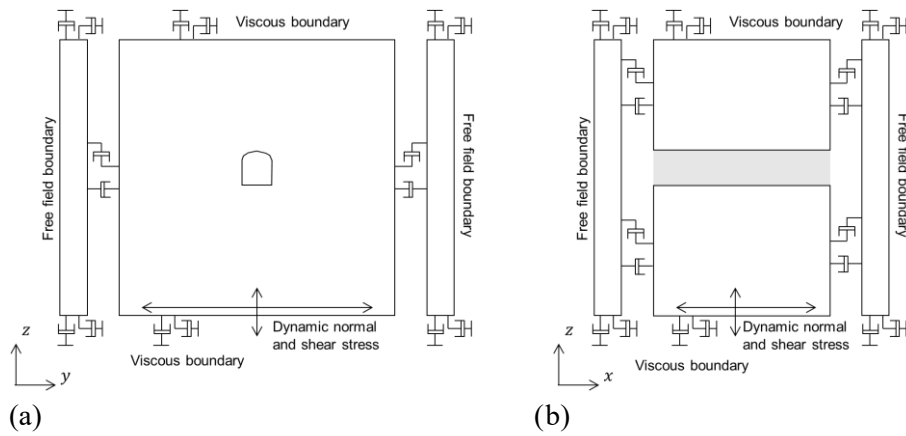
Figure 5.18 Dynamic boundary conditions of the three-dimensional numerical model in the (a) yz cross-section and (b) xz cross-section

During the dynamic analysis, Rayleigh damping was applied to all models to reflect the energy losses. Ten percent of the mass Rayleigh damping was assumed according to the guidelines for geological materials and structural systems in the dynamic simulation of 3DEC (Itasca, 2013).

In the dynamic simulations of this research, three earthquake models were prepared with different peak ground velocities to compare the effects on fractures. The velocity models in Figure 5.17 have 0.1 m/s of peak ground velocity, and models with the larger peak ground velocity can be constructed by multiplying the entire

velocity histories. The prepared velocity models reflect 0.2, 0.4, and 0.8 m/s of peak ground velocity based on the velocity histories in Figure 5.17.

Unlike the previous models in excavation, thermal, and glacial simulation, the numerical models for the dynamic analysis only include the two fractures, showing the significantly different mechanical behavior between them. Also, the larger edge sizes of zones comprising each block are used to build the dynamic model at about 4 m. During the 10 seconds of duration time, the normal and shear displacement on two fractures were captured. The transient changes of the normal and shear stress on each fracture surface were also monitored to analyze the possibility of shear slip.

5.4.2 Results of the earthquake simulation

A dynamic analysis was performed on the numerical models containing two fractures, Fracture #32 and #60, under 10 seconds of three-dimensional stress histories with three different PGVs: 0.2, 0.4, and 0.8 m/s. During the entire duration time, the detailed mechanical responses for the two fractures were monitored.

Figure 5.19 shows the transient transmissivity evolution ratio due to three different earthquake models at the center points of Fracture #32 and #60. The fluctuations of transmissivity can be found from both fractures, especially under the larger PGV earthquake. While Fracture #32 shows the reversible fluctuations in transmissivity changes, about 1.08 times the permanent transmissivity increase was found on Fracture #60 in 4.15 seconds, only under the earthquake models with 0.8 m/s PGV, which was also observed in the case of the 1999 Chi-Chi earthquake with a magnitude of 7.3 in Taiwan (Tsai and Huang, 2000).

(a)

(b)
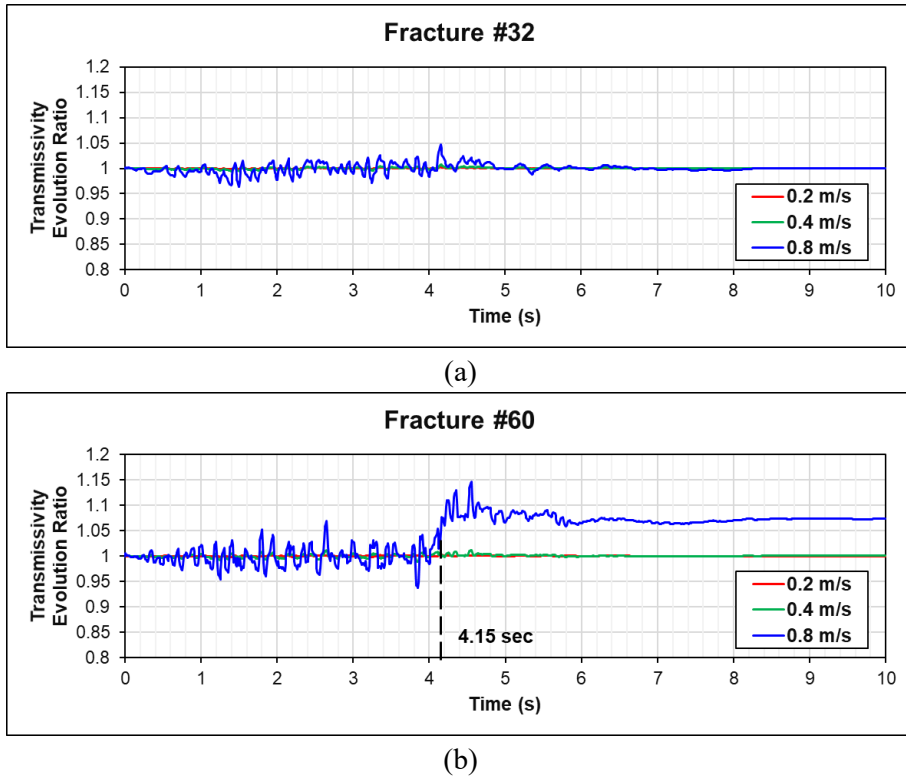
Figure 5.19 Transient transmissivity evolution ratio at the center of (a) Fracture #32 and (b) Fracture #60 during three different PGV model

To investigate the detailed mechanical behavior of fractures, the transient normal and shear stress at the center points of the fractures were monitored during an earthquake scenario with 0.8 m/s of PGV, as shown in Figure 5.20. The normal and shear stress on both fractures fluctuated, especially from 0 to 6 seconds, but finally recovered to the initial stress condition at the end of the earthquake. At 4.15 seconds on Fracture #60, the maximum shear stress was induced with a 1.5 MPa increase value compared to the initial shear stress, which indicates the possibility of shear slip. Fracture #32 showed the peak shear stress at 3.23 seconds with a 0.9 MPa increase, but shear slip may not occur because the high normal stress is maintained

during the entire earthquake scenario. Therefore, the fluctuating transmissivity on Fracture #32 is basically dominated by the reversible normal deformations induced by the normal stress fluctuations.

(a)

(b)
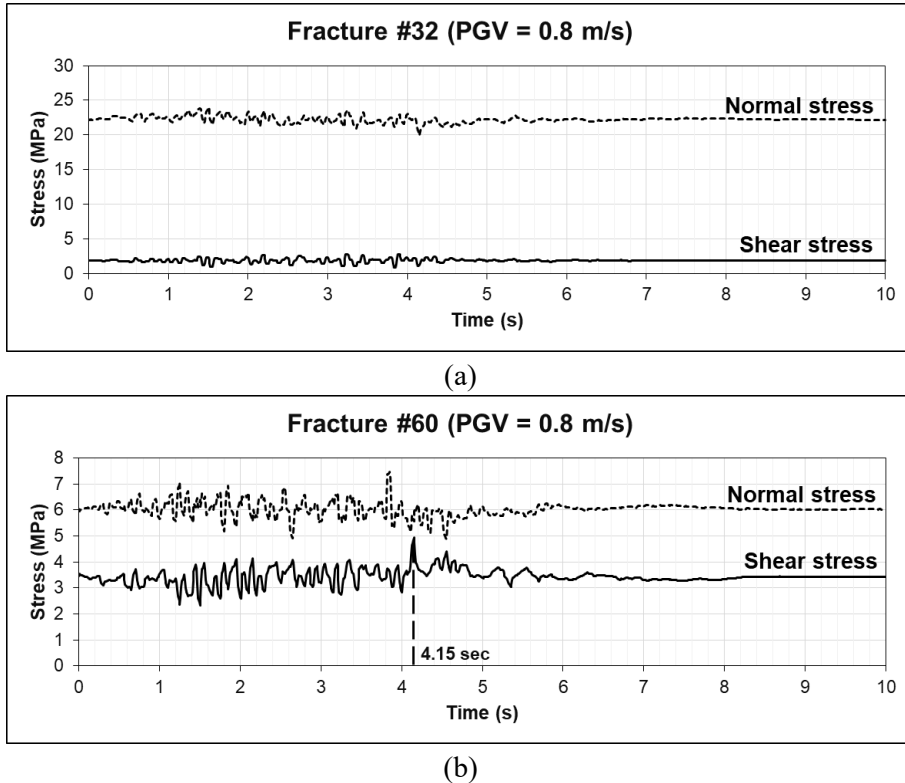
Figure 5.20 Transient normal and shear stress fluctuation during the earthquake scenarios with 0.8 m/s of PGV on (a) Fracture #32 and (b) Fracture #60

The stress conditions during the earthquake scenarios are visualized on the normal-shear stress plot to compare with the Coulomb failure envelope of fractures (Figure 5.21). The initial condition of Fracture #60 is closer to the Coulomb envelope, which indicates more vulnerable to slip, than Fracture #32, and indeed, the stress conditions of Fracture #60 in 4.15 seconds reaches the Coulomb envelope. Focusing on the point clouds of stress conditions, the stress conditions of Fracture #32 are

distributed in wider normal stress ranges than the stress distribution of Fracture #60. On the other hand, the shear stress ranges are widely distributed in Fracture #60. Similar to the glacial and thermal loading, the dynamic disturbance on Fracture #32, which is perpendicular to the tunnel surface, tends to be concentrated as tangential normal stress, while Fracture #60, which is inclined to the tunnel floor, shows the shear disturbance more.
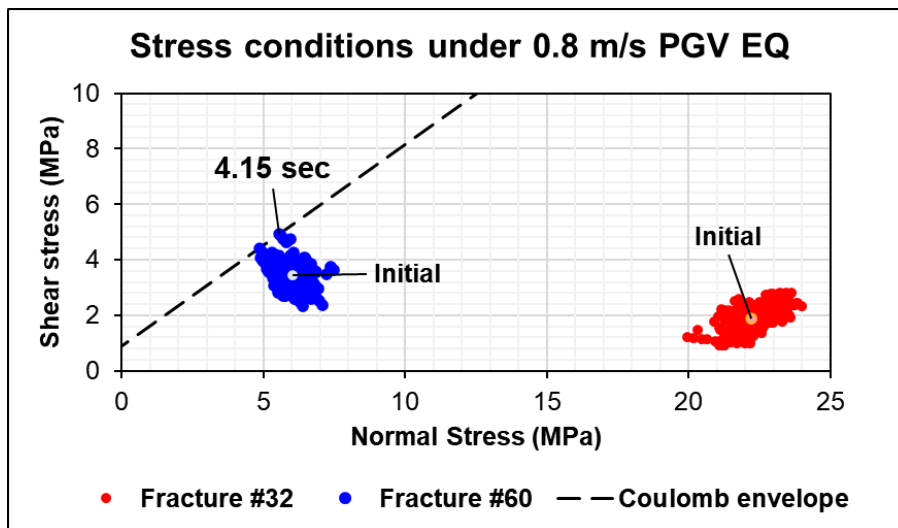
Figure 5.21 Stress conditions during the earthquake with 0.8 m/s of PGV on two fractures

Chapter 6. Transmissivity evolution on the uniformly jointed model

The previous simulation results in Chapter 4 and 5 introduced the specific case of the Äspö HRL based on the mapped fracture data. This chapter expands the numerical model with a generic case that can apply to various candidate sites for the geological repository for the HLW.

Simulations with uniformly jointed models focus on monitoring the transmissivity changes on the various orientations of the joint sets around the repository. The in-situ stress, boundary conditions, rock and joint properties are taken from the Äspö HRL model, but the contained discontinuities are different from the previous model. The 20 m x 30 m x 30 m cubic area around the center of the tunnel is assumed as the target area containing the joint set (Figure 6.1). A single joint set with 1 m spacing is positioned around the tunnel. A total of ten uniformly jointed models are prepared with five different dip angles (0°, 30°, 45°, 60° and 90°) and two different dip direction angles (0° and 90°) (Figure 6.2). A dip of the joint surface is measured downward from the horizontal (xy) plane, and the dip direction is positive measured clockwise from the y direction, which is assumed as the North direction in this chapter. Each jointed model is simplified as the "dip direction/dip" model according to the dip direction and dip angle of the included joint sets. For example, the model in Figure 6.1 with a 0° dip direction and a 45° dip is named the 000/45 model.
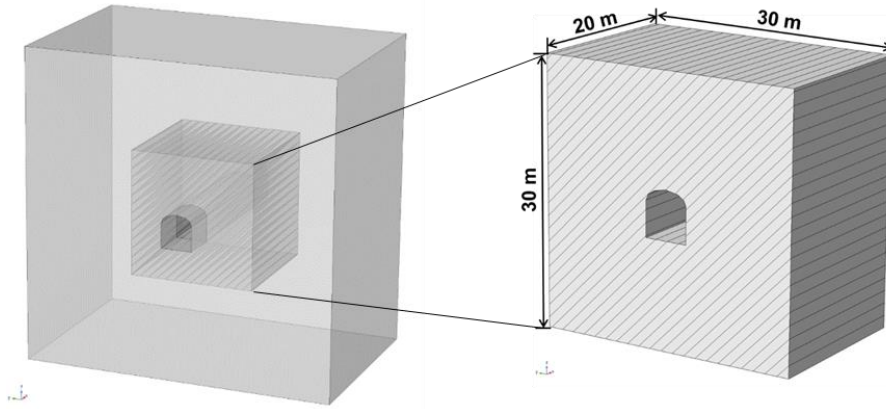
Figure 6.1 Three-dimensional geometry of the uniformly jointed model (left) and the jointed target domain with a 0° joint dip direction and 45° joint dip (right)
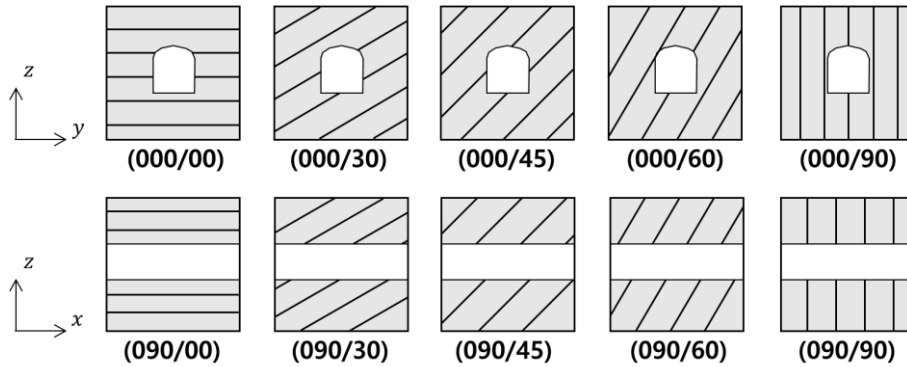
Figure 6.2 Schematic layout of the uniformly jointed domain. Each model name is simplified as (dip direction/dip)

Simulations on each jointed model are conducted considering the effects of stress-redistribution, thermal stress, glaciation, and earthquake. The main parameter to monitor during the simulations is the transmissivity on the joint and the detailed mechanical behaviors are analyzed during and after each scenario. The quantified transmissivity changes induced by excavation, thermal stress, glaciation, and earthquake are compiled, and the spatial extent of the disturbed area is determined by the location and orientation of joints.

6.1 Stress re-distribution by excavation on the uniformly jointed model

On each uniformly jointed model, the horseshoe-shaped tunnel is positioned at the center of the jointed domain. The stress re-distribution appears around the tunnel and the joints near the tunnel are disturbed, showing the deformations and shear slips. The disturbed transmissivity was calculated from the aperture that changed from 30 μm of zero-stress aperture for each gridpoint on the joints. The transmissivities are compiled by distance from the tunnel surface along the monitoring line starting from the tunnel roof, wall, and floor.

6.1.1 Model with a 0° joint dip direction

Figure 6.3 shows the transmissivity distribution by depth from models with five different dip angles. At the vicinity of the lateral wall, three-order increases of fracture transmissivity are observed in 000/60 and 000/90. The drastic transmissivity increases on the fracture disappear about 2 m away from the tunnel wall. On the other hand, the fracture transmissivity on the 000/00 and 000/30 models accompanies the high transmissivity increase along the monitoring lines of the tunnel roof and floor, while there is no significant change at the lateral wall. The fracture transmissivity increases about two orders at the roof and three orders at the floor, and the largest increase appears at the 1 m depth from the floor of the 000/30 model.
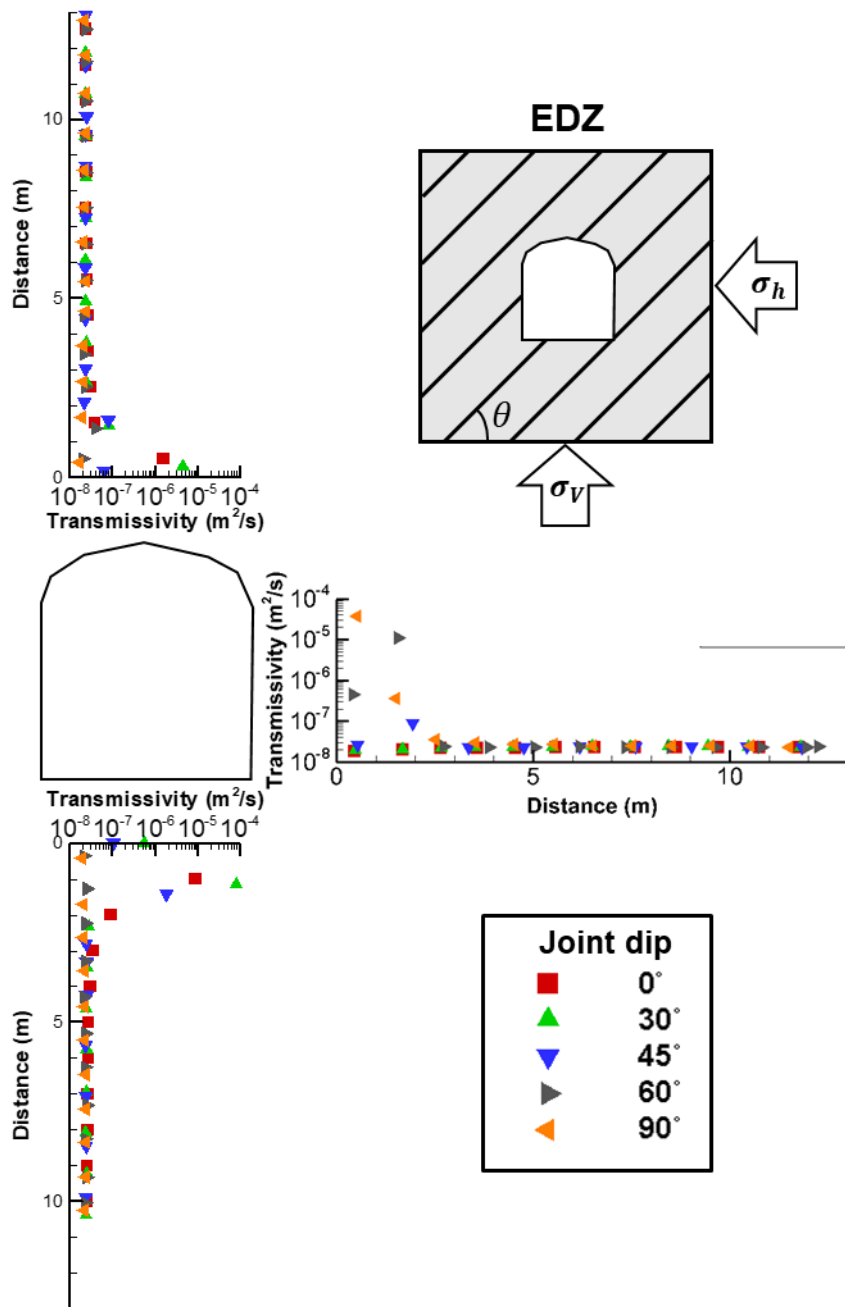
Figure 6.3 Transmissivity distribution due to the stress re-distribution on models with a 0° joint dip direction

The 000/00 fractures at the roof and floor are only dominated by the normal opening induced by stress relaxation, according to the stress-dependent normal stiffness, which happens similarly at the lateral wall of the 000/90 fractures. The 000/30 fractures at the roof and wall also disturbed by the reversible normal opening, but the tangential stress concentration plays a role in generating the shear stress on the fracture surface. The concentrated shear stress derives the shear slip and dilation of the fractures, which induce the irreversible transmissivity increase, so the 000/30 model shows the largest transmissivity increase. Similarly, the 000/60 fractures accompany a larger transmissivity increase at the lateral wall than the 000/90 fractures due to the combined effects of the normal opening and shear dilation.

6.1.2 Model with a 90° joint dip direction

In the case of models where the joint dip direction angle is 90°, the transmissivity increase appears along the roof and floor monitoring lines of the 090/00, 090/30, and 090/45 models. The 090/30 model entails the highest transmissivity increase up to two orders at the roof and three orders at the floor (Figure 6.4). The 090/00 model also shows a similar amount of increase to the 090/30 model, but the decreasing trend by depth was more drastic than in the 090/30 model. The 090/60 and 090/90 models only maintain the initial aperture or show decreased transmissivity. Along the wall monitoring lines, the transmissivity changes are not significant, and only small amount of decreases are observed at the shallow depth.
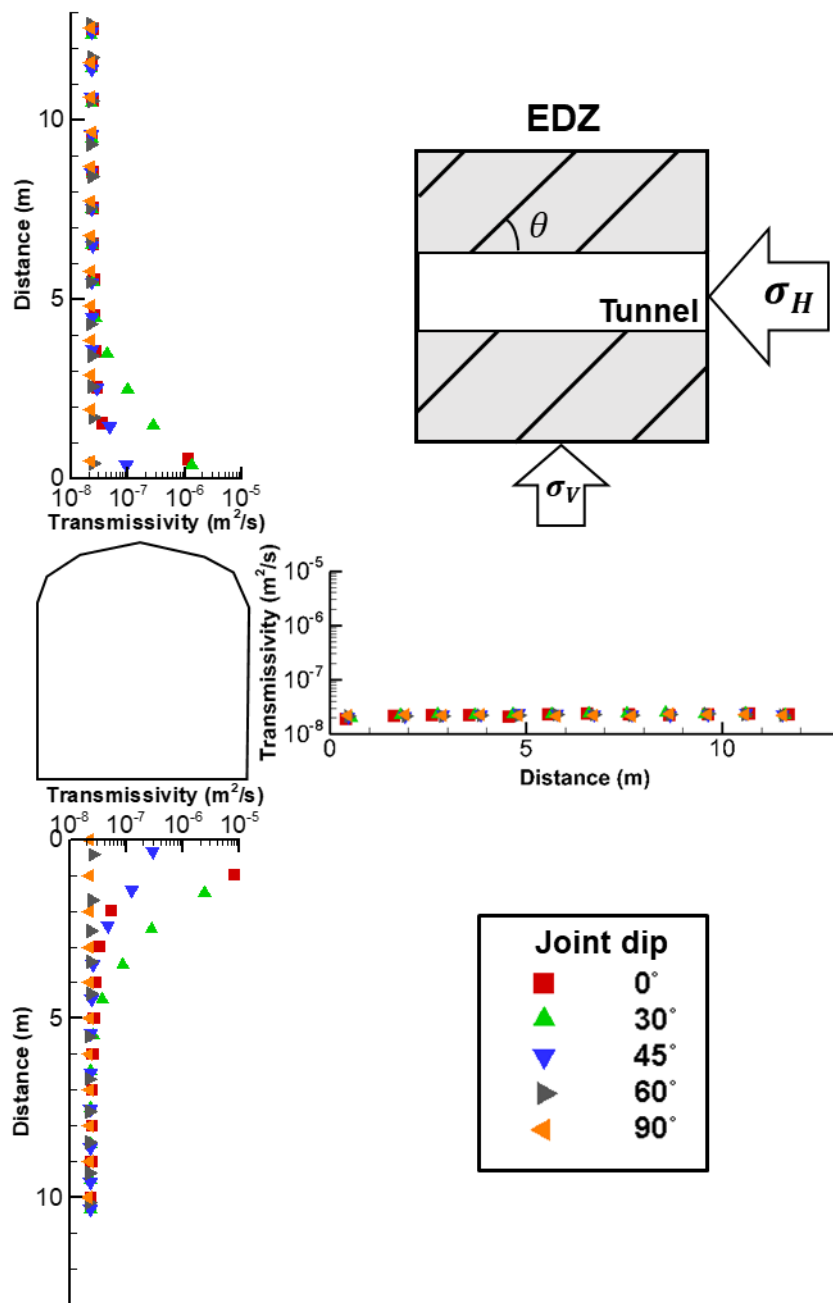
Figure 6.4 Transmissivity distribution due to the stress re-distribution on models with a 90° joint dip direction

The 90° dip direction fractures are controlled by the maximum principal stress with a magnitude about twice the vertical stress, while the stress ratio of the vertical and horizontal stresses on the 0° dip direction fractures are almost 1. The high differential stress entails not only the large in-situ shear stress on fractures but also the strong stress concentration after the excavation. Therefore, the transmissivity increases seen on the 090/30 model appear in a much wider area than the 000/30 model along the roof and floor monitoring line, while the magnitude of increase on the 090/30 model is smaller than the results from the 000/30 model, probably due to the high normal stress induced by the maximum horizontal principal stress. Similarly, the 090/45 and 090/60 models show less significant transmissivity changes than the 000/45 and 000/60 models due to the high normal stress concentration on fracture surfaces.

6.2 Thermal loading on the uniformly jointed model

In the thermal loading scenarios, the numerical simulations with the uniformly jointed models are focused on the permanent increase of fracture transmissivity after the entire scenario ends. Therefore, the mechanical responses on the joints after 50,000 years of thermo-mechanical simulations are observed and analyzed by comparing them to the initial conditions resulting from the excavation scenarios. The thermal models in this section have the same properties, boundaries, and heat sources as in Table 4.1 and Figure 5.4.

6.2.1 Model with a 0° joint dip direction

The thermally induced transmissivity changes are analyzed by the transmissivity evolution ratio between the final fracture transmissivity and the initial value obtained in Chapter 5.1. Figure 6.5 shows the distributions of the thermally induced transmissivity evolution ratio along the three monitoring lines in the 0° dip direction models. The transmissivity disturbance by heat sources only appears at the floor and lateral wall of tunnel, and there is no significant response on the tunnel roof. The transmissivity increases are more easily found at a shallow depth up to 3 m from the tunnel surface. The permanent increases in transmissivity are up to 2.2 times the initial value, and the 000/30 model shows the largest transmissivity evolution ratio at a 2 m depth from the tunnel floor.

Figure 6.5 Transmissivity evolution ratio by thermal loading on models with a 0°
joint dip direction
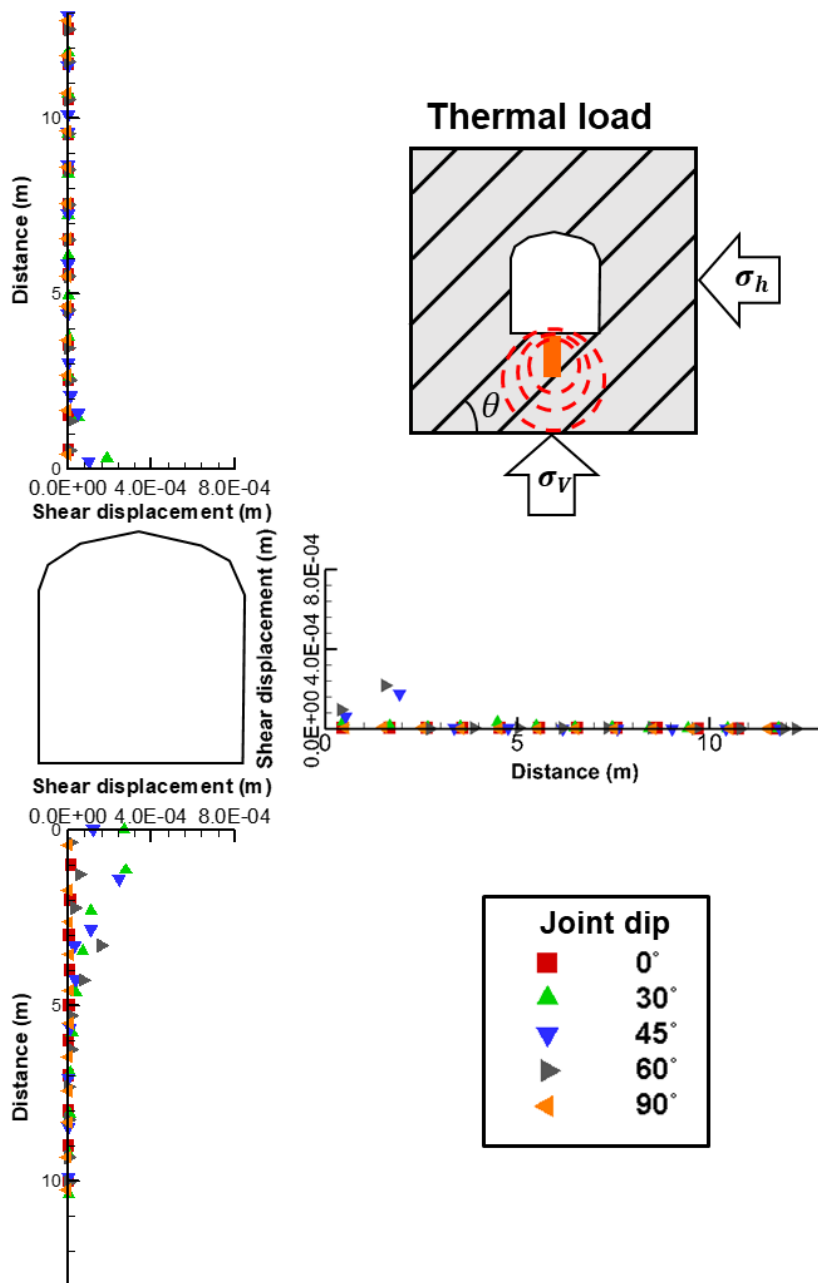
Figure 6.6 Shear displacement induced by thermal loading on models with a 0° joint dip direction

To ensure that the permanent transmissivity increases originated from the thermo-shearing, the thermally induced shear displacements are plotted in Figure 6.6. From the final shear displacement, the initial shear displacement induced by the stress re-distribution is excluded to focus on the thermal effects, and the thermal terms on joints are averaged along each monitoring line.

The thermally induced shear displacement distribution follows the increasing trends of transmissivity in Figure 6.5. The shear slip is occurring significantly at the floor and lateral wall, while the joints along the roof monitoring line rarely show the shearing. The largest shear displacement is found at the roof of the 000/30 models, as well as the transmissivity evolution ratio at a depth of 2 m and a magnitude of 280 μm. In the wall monitoring line, the 000/60 model shows 220 μm of shear displacement at a depth of 3 m.

6.2.2 Model with a 90° joint dip direction

Based on the simulation results from the 90° dip direction models, the transmissivity evolution ratio and shear displacement distribution by depth are plotted in Figure 6.7 and Figure 6.8, respectively. The thermally induced transmissivity increases are only found along the floor monitoring line. as Along with the 0° dip direction models, the 090/30 model shows the largest transmissivity increase, and the evolution ratio is 2.3 at a 4 m depth from the tunnel floor. The largest shear displacement induced by the thermal loading also appears at the same interval of the 090/30 model, at 220 μm. It is also found that there is no thermally induced slip on joints at the tunnel wall (Figure 6.8).
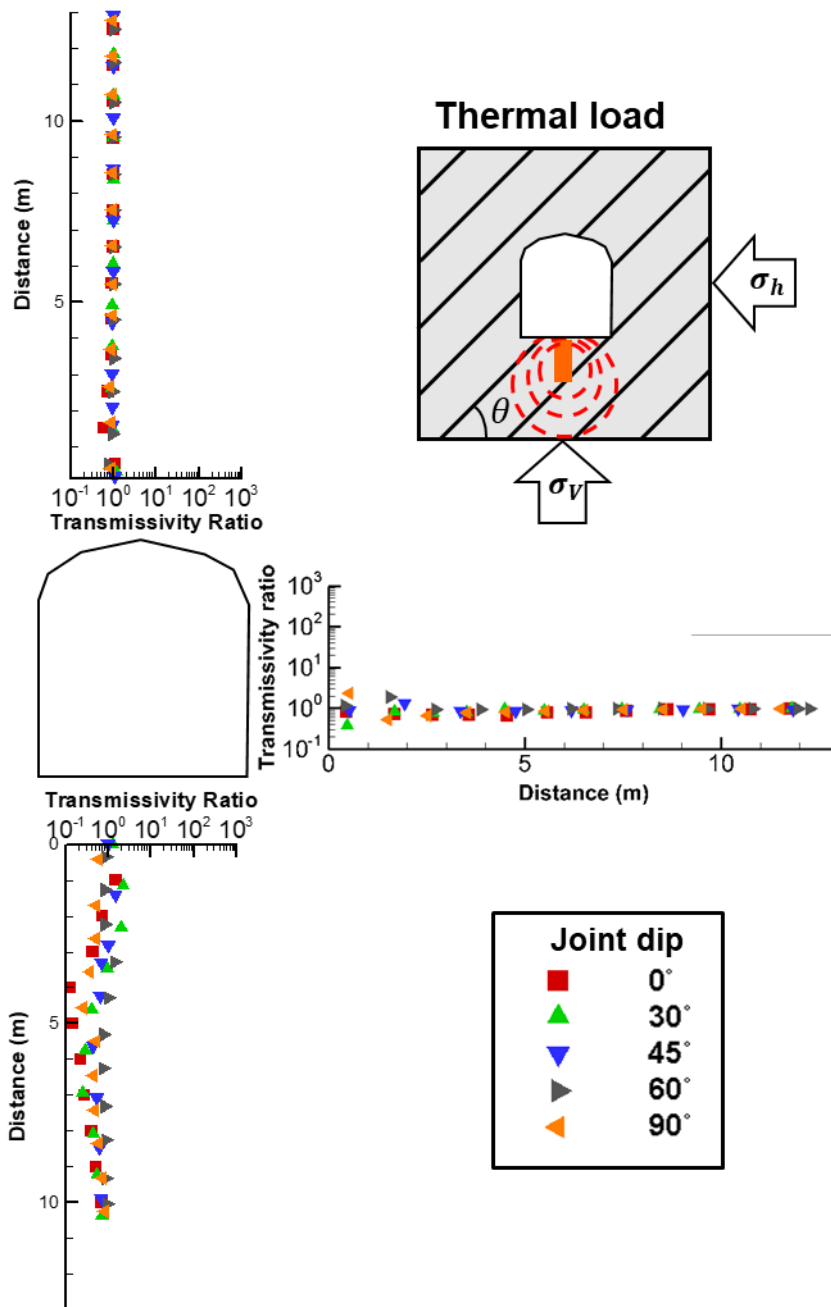
Figure 6.7 Transmissivity evolution ratio by thermal loading on models with a 90°
joint dip direction
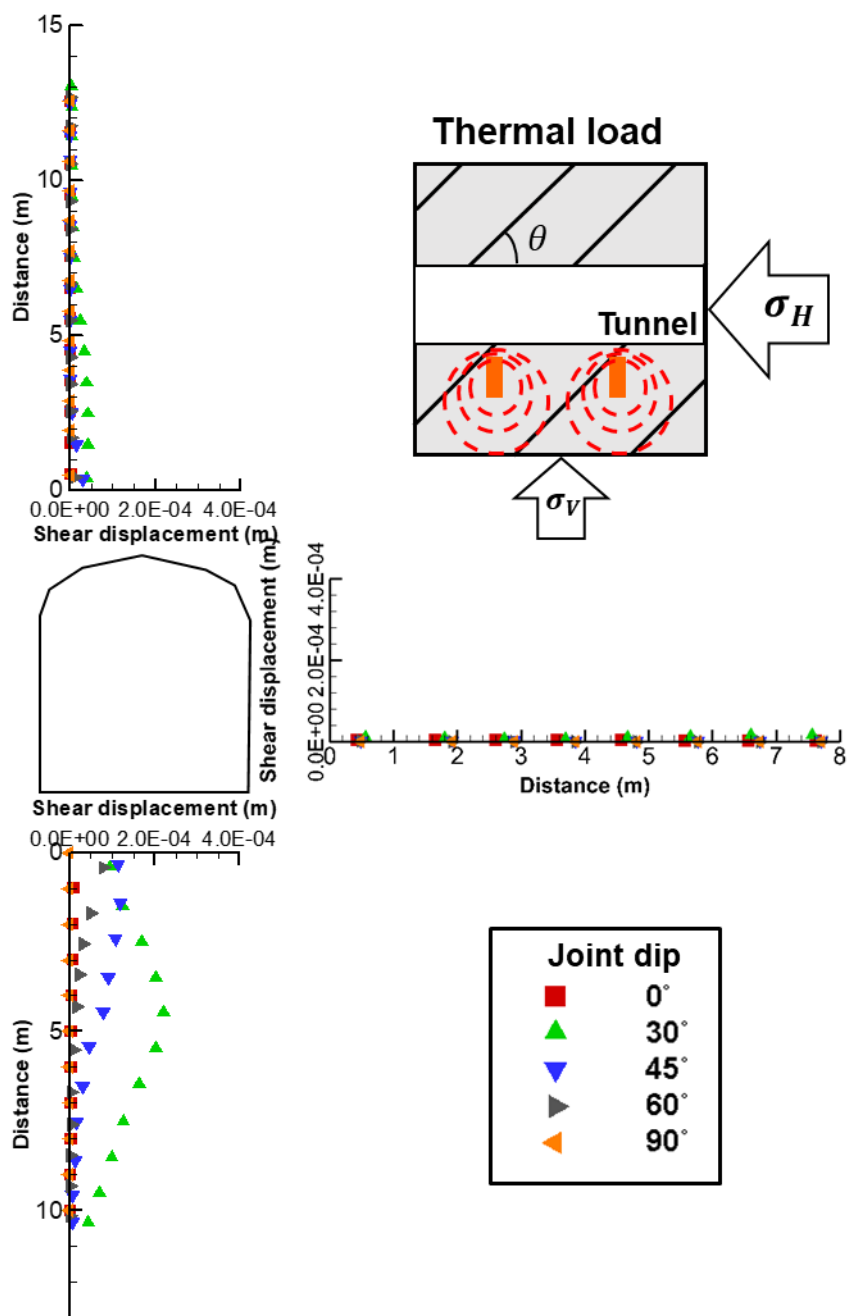
Figure 6.8 Shear displacement induced by thermal loading on models with a 90° joint dip direction

6.3 Glaciation on the uniformly jointed model

To determine the effects of glaciation on fractured rock by orientation, the glacial loads are applied on the prepared uniformly jointed models. The glacial scenarios are the same as the Weichselian glacial model with two glacial maxima (Figure 5.11), and the transmissivity evolution ratio and shear displacement are monitored when the 70,000-year glacial scenarios end. Since the stress conditions at the end of the scenarios are the same as the initial condition, the glacially induced permanent response on fractures can be obtained by a comparison with the results from Chapter 5.1.

6.3.1 Model with a 0° joint dip direction

Compared to the thermally induced changes, the glaciation scenarios induce a more significant transmissivity increase at the shallow depth of every model. Along the roof and floor monitoring line, the 000/30 and 000/45 models showed a drastic increase in fracture transmissivity, while the 000/60 model entails a transmissivity increase at the tunnel wall (Figure 6.9). A two-order increase was the largest transmissivity evolution ratio observed at a depth of 2 m in every monitoring line. The increasing transmissivity trends of the 000/30, 000/45, and 000/60 models coincide with the shear displacement distribution shown in Figure 6.10. The largest shear displacement was observed at a 1 m depth from the tunnel floor of the 000/30 model at 1100 μm. At the tunnel wall, the 000/60 model results showed 770 μm of shear displacement at the 2 m depth.

Figure 6.9 Transmissivity evolution ratio by glaciation on models with a 0° joint dip direction
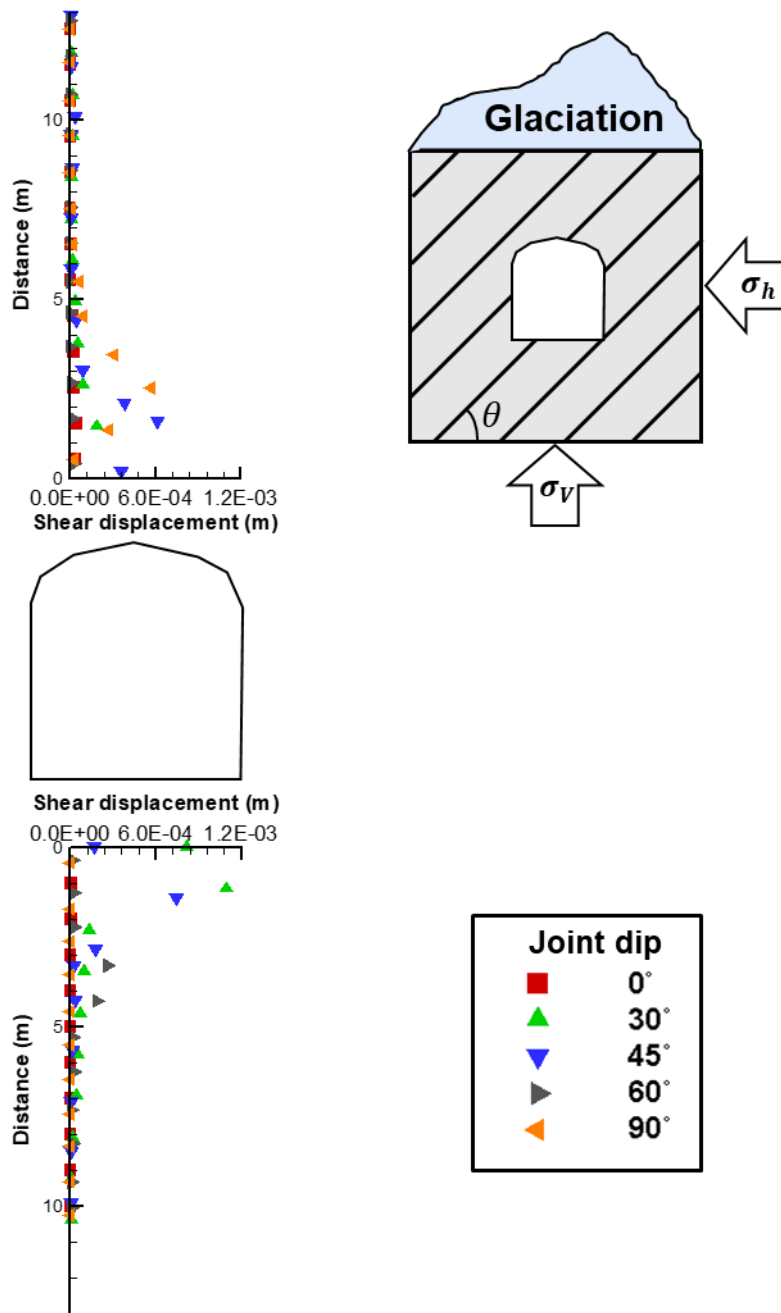
Figure 6.10 Shear displacement induced by glaciation on models with a 0° joint dip direction

Figure 6.11 Spatial extent of the disturbed zone showing a two-times transmissivity increase by stress re-distribution, thermal loading, and glaciation in 0° dip direction models

According to the distributed transmissivity evolution ratio induced by stress re-distribution, thermal loading, and glaciation, Figure 6.11 visualizes the zone showing a two-times transmissivity increase around the tunnel. The fracture transmissivities on contacts contained in each polar pixel are averaged, and the transmissivity evolution ratio is calculated based on the corresponding initial value. The 000/00 and 000/90 models result in a smaller zone than the 000/30, 000/45, and 000/60 models in every scenario. In the excavation scenario, the disturbed zone is distributed nearby the tunnel surface parallel to the joint orientation due to the dominant effect of stress relaxation. The thermal and glacial scenarios also result in a similar zone, but the transmissivity more drastically changes around the tunnel surface, which is slightly inclined (sub-parallel) to the joint orientation. On the joint surface, slightly inclined from the tunnel surface, the shear stress is highly concentrated due to the additionally

concentrated tangential stress induced by the thermal and glacial loading.

In the 000/30, 000/45, and 000/60 model results, the disturbed zone is widely observed at the right corner of the tunnel. The stress concentration at the angular corner tends to be drastic and complicated, and the glacially and thermally induced stresses can highly disturb the stress condition on joint surface. Therefore, the joint near the right corner of the tunnel could be vulnerable to shear slip and could easily show the drastic shear displacement by the additional stress. On the other hand, the joints nearby the left corner intersect the tunnel sub-perpendicularly and entail high normal stress due to the tangential stress concentration.

6.3.2 Model with a 90° joint dip direction

Figure 6.12 is the distributed transmissivity evolution ratio along the three monitoring lines extracted from the 90° dip direction joints. The overall transmissivity increases are smaller than the 0° dip direction models. In particular, there are no significant changes to the transmissivity along the wall monitoring line. The largest change on transmissivity was a one-order increase along the roof monitoring line. Interestingly, the 090/30 and 090/45 models show the increasing tendencies at about 5 m away from the roof and floor, while the 090/00 model shows an increase only at the shallow depth.
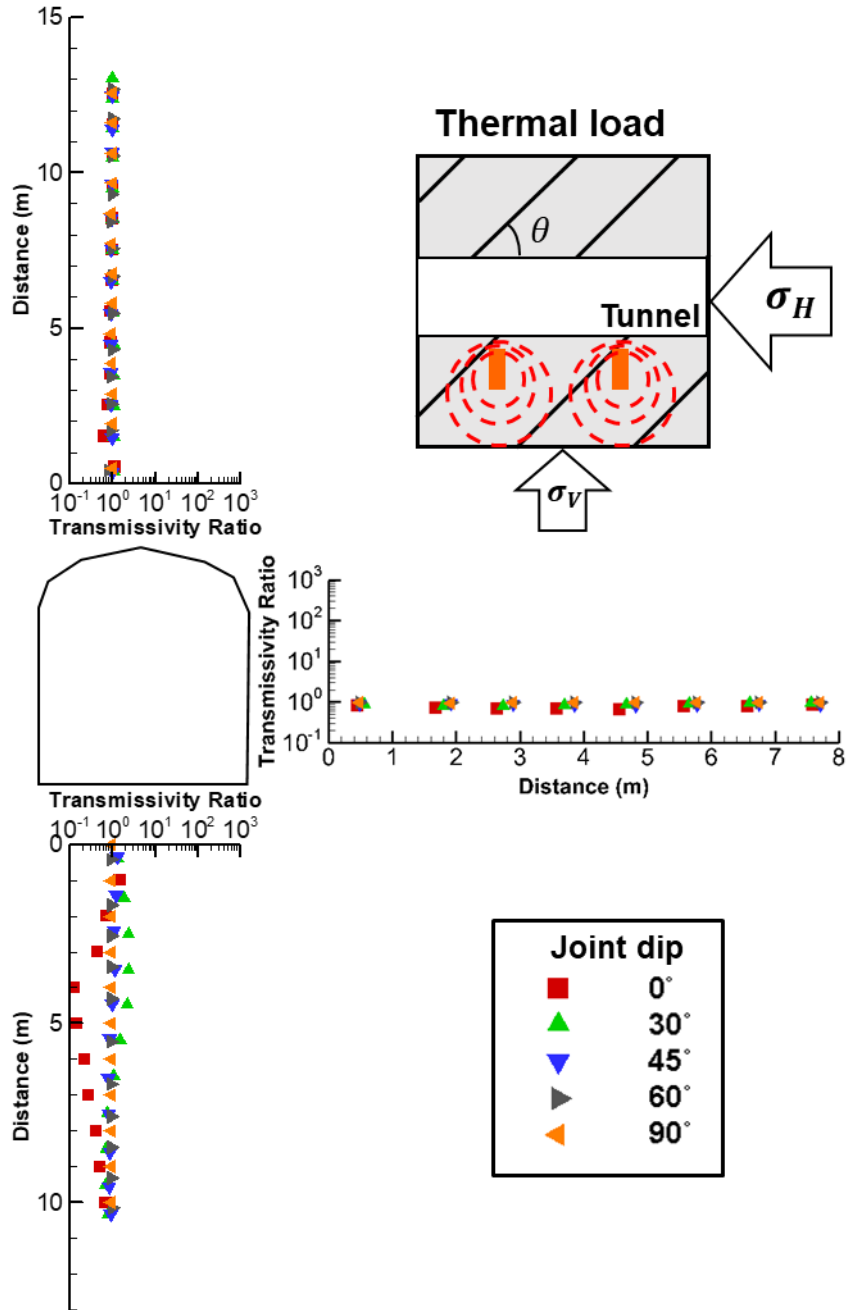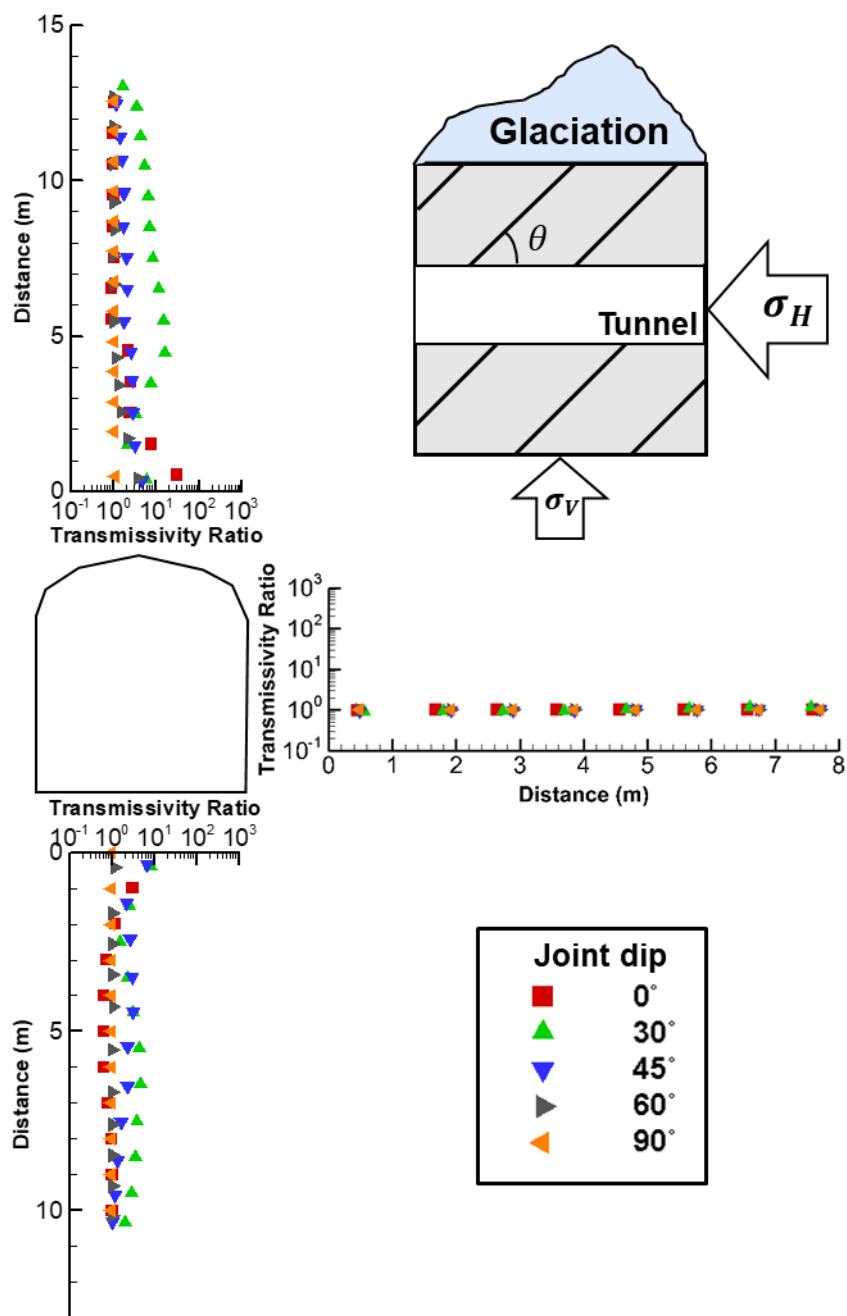
Figure 6.12 Transmissivity evolution ratio by glaciation on models with a 90° joint dip direction
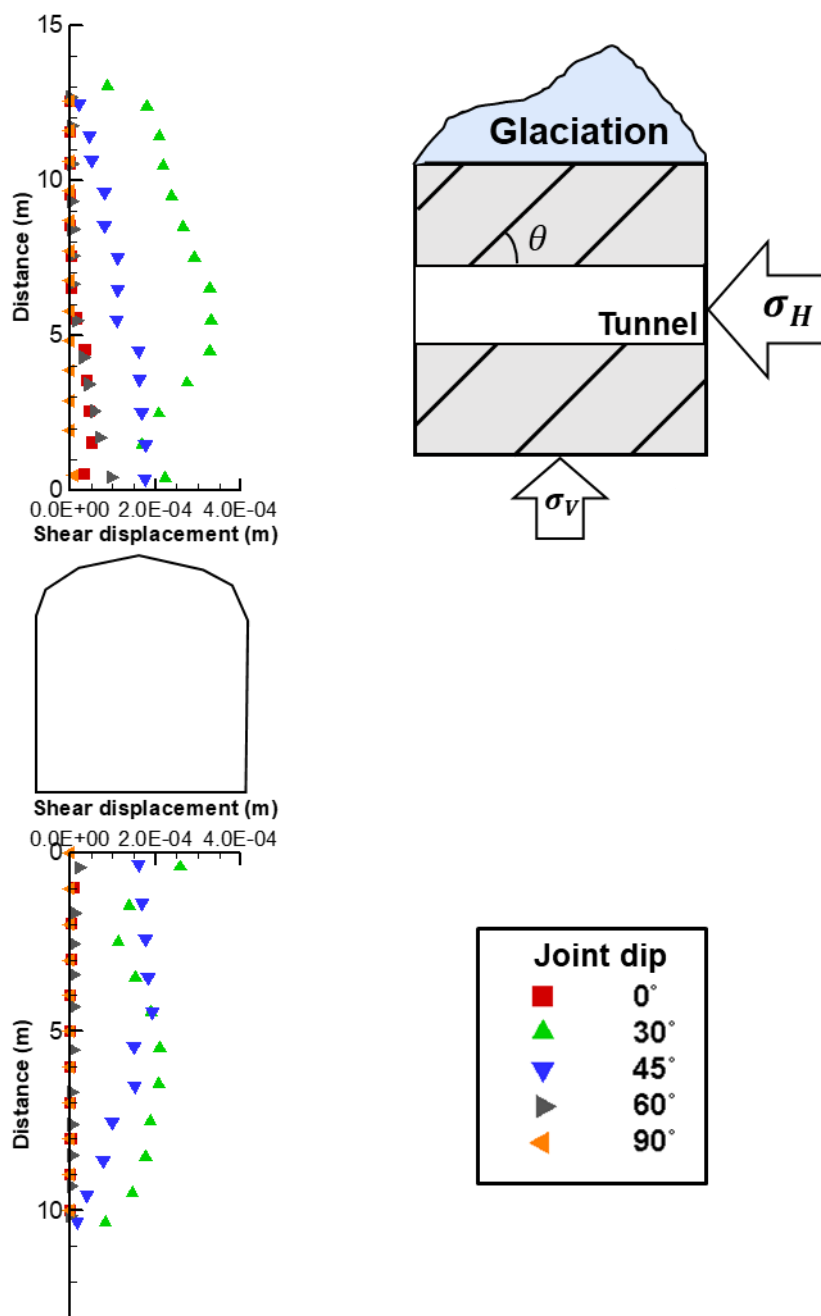
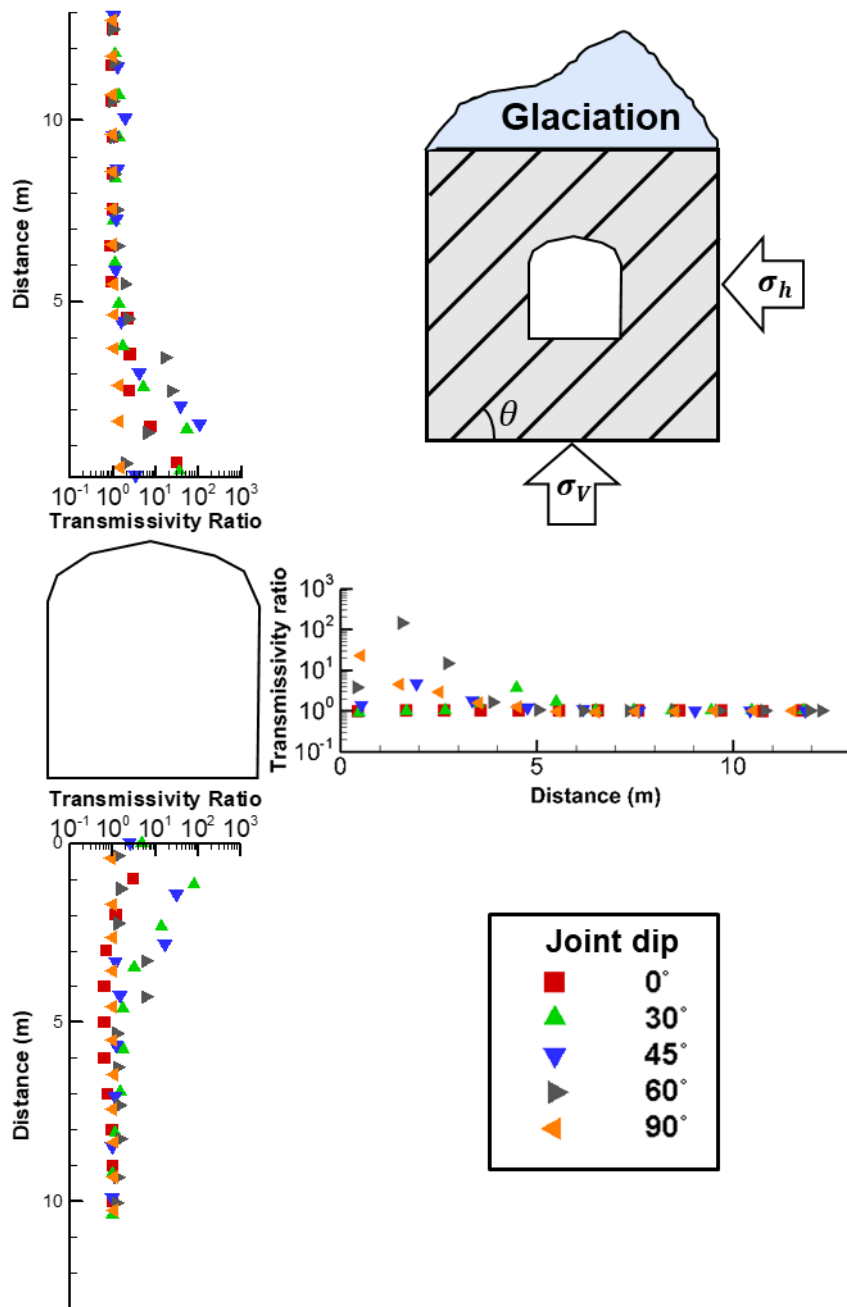Figure 6.13 Shear displacement induced by glaciation on models with a 90° joint dip direction

According to the distribution of the glacially induced shear displacement in Figure 6.13, 330 μm of peak shear displacement appears at about 5 m distance from the tunnel roof in 090/30 model. The joints at the tunnel wall do not show the shear displacement in every case, because the stress conditions of the joint at the wall are only dominated by the stress concentration in tangential and axial directions, which decrease the possibility of shear slip.
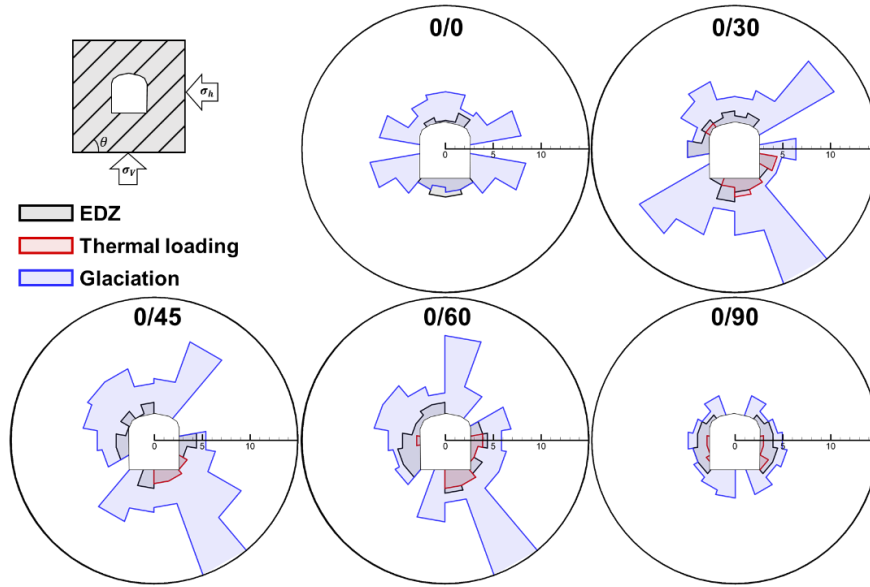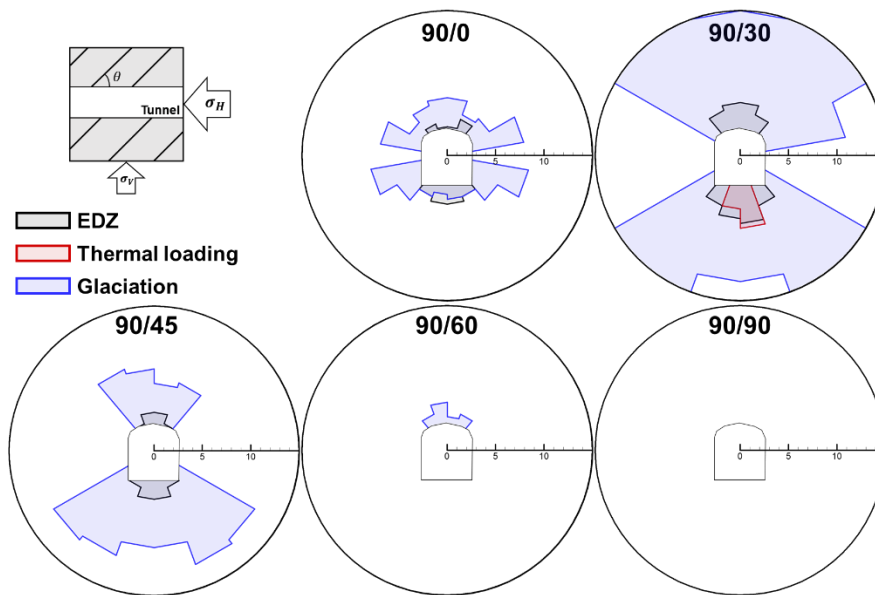

Figure 6.14 Spatial extent of the disturbed zone showing a two-times transmissivity increase by stress re-distribution, thermal loading, and glaciation in 90° dip direction models

Figure 6.14 shows the spatial extent of the zones showing two-time of transmissivity increases on the models with a 90° joint dip direction. The 90° dip direction models accompany a wider disturbed area than the 0° dip direction, especially under the glacial scenarios, despite the smaller magnitude of the transmissivity changes. Since the stress conditions on the 90° dip direction joints are

controlled by the vertical and maximum horizontal in-situ stresses, which induce high shear stress, those joints could already be vulnerable to slip. The 0° dip direction joints are more difficult to slip, however, the shear displacements within the disturbed area tend to be more serious.

6.4 Earthquake on the uniformly jointed model

According to the results from the Äspö HRL model shown in Chapter 4.4, the earthquake models with 0.8 m/s of PGV could induce the permanent transmissivity evolution on fractures, depending on the geometrical characteristics. Therefore, a 0.8 m/s PGV earthquake was applied to the prepared uniformly jointed models to investigate the detailed relationship between the transmissivity change and geometrical characteristics.

Unlike the previous uniformly jointed models, four joints in this earthquake scenario were prepared at a 1 m depth from the roof, left wall, right wall, and floor of the tunnel. The displacements and stress conditions at 1 m distance from the roof, wall, and floor were monitored during 10 seconds of an earthquake.

6.4.1 Model with a 0° joint dip direction

Figure 6.15 shows the transmissivity evolution ratio during an earthquake with 0.8 m/s of PGV. The transmissivities were captured at 1 m apart from the tunnel roof, wall, and floor. The irreversible transmissivity increases appeared on the 000/30 and 000/45 models from both the tunnel roof and floor, while the 000/45 model showed transmissivity increases at the tunnel wall. The largest transmissivity evolution ratio was 4.29 at the tunnel floor of the 000/45 model. The transient shear displacement in Figure 6.16 indicates the occurrence of shear slip on joints showing an irreversible transmissivity increase.

(a)

(b)

(c)

Figure 6.15 Transmissivity evolution ratio during a 0.8 m/s PGV earthquake at the (a) roof, (b) wall, and (c) floor of models with a 0° joint dip direction

The stress conditions during the earthquake are plotted in Figure 6.17 by comparing them to the Coulomb envelope. The 000/30 and 000/45 models, especially the 000/45 model, are under vulnerable initial stress conditions for slipping already and reach the Coulomb envelope due to the fluctuation of about 5 MPa in normal stress and 3 MPa in shear stress. Compared to the other scenarios, the earthquake scenario is sensitive to the initial stress conditions of the joint disturbed by the tunnel opening. Therefore, the 000/45 model, with a normal stress

low enough and shear stress high enough, entails a permanent transmissivity increase at the roof, wall, and floor.

(a)

(b)
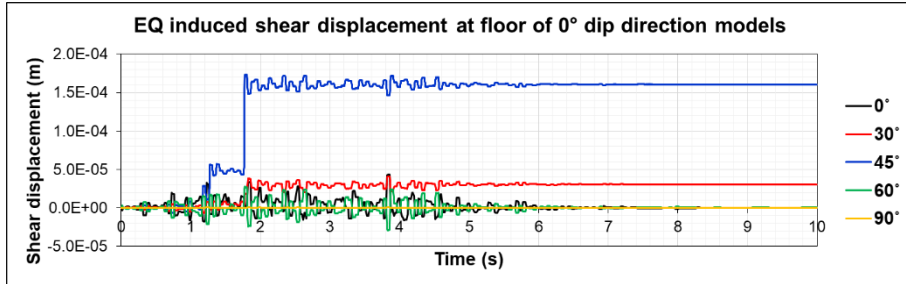
(c)

Figure 6.16 Shear displacement induced by a 0.8 m/s PGV earthquake at the (a) roof, (b) wall, and (c) floor of models with a 0° joint dip direction
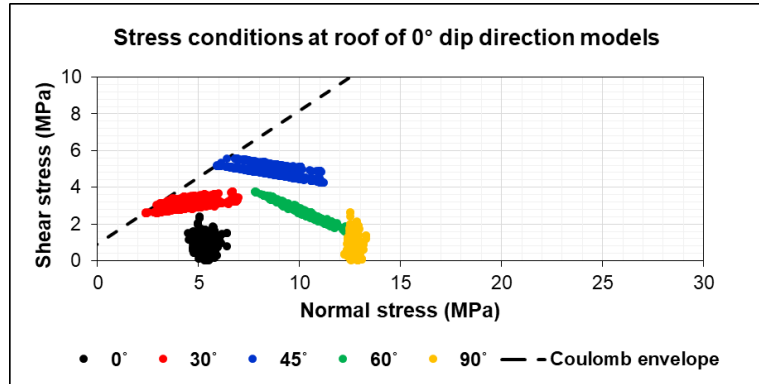
(a)
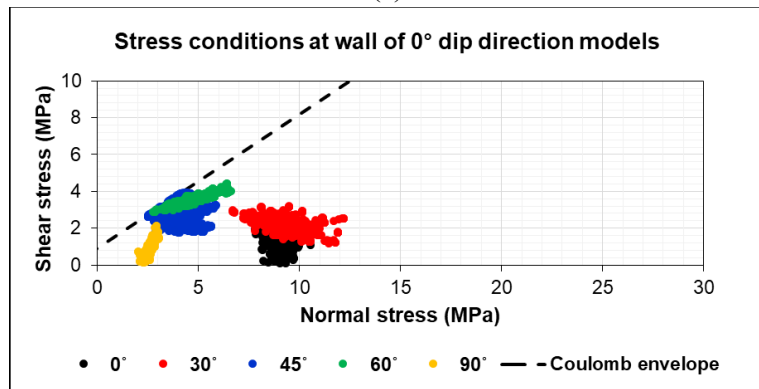
(b)
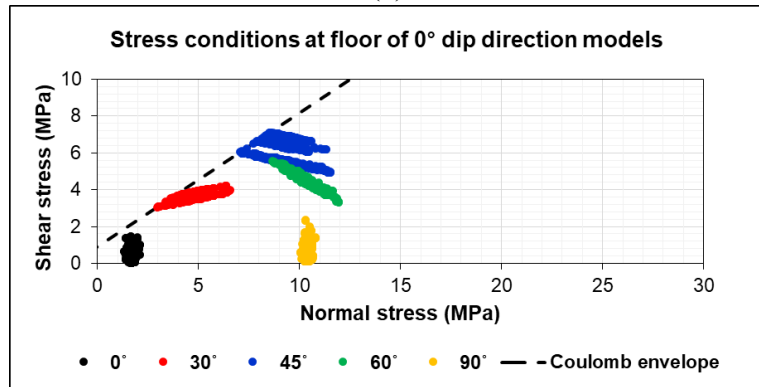
(c)

Figure 6.17 Stress conditions during a 0.8 m/s PGV earthquake at the (a) roof, (b) wall, and (c) floor of models with a 0° joint dip direction

6.4.2 Model with a 90° joint dip direction

(a)

(b)

(c)
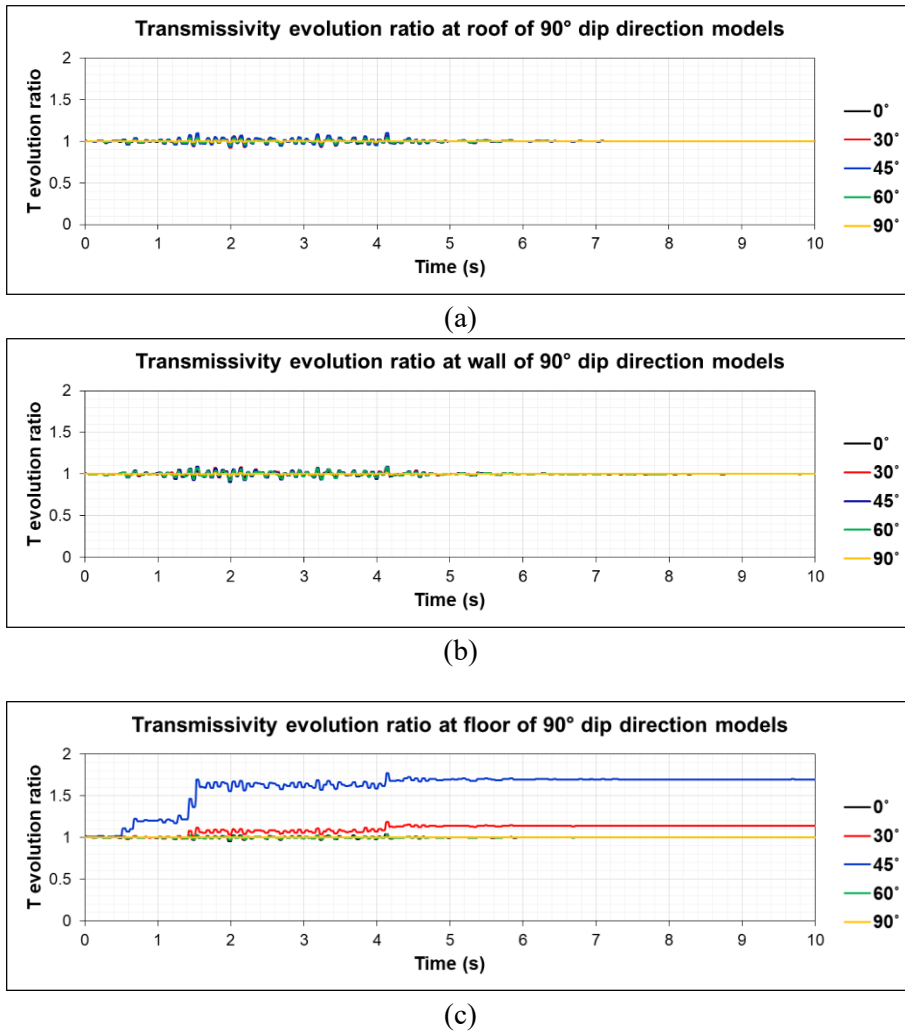
Figure 6.18 Transmissivity evolution ratio during a 0.8 m/s PGV earthquake at the (a) roof, (b) wall, and (c) floor of models with a 90° joint dip direction

The transmissivity evolution ratio of models with a 90° dip direction is plotted in Figure 6.18. Significant irreversible transmissivity increases appeared at the tunnel floor of the 090/30 and 090/45 models. The transmissivities at the roof and wall showed a reversible fluctuation without permanent changes. The largest transmissivity evolution ratio was observed in the 090/45 models at 1.70. Figure 6.19

112

shows the transient shear displacement at each monitoring point during the earthquake loading, along with the significant shear displacement on the 090/30 and 090/45 models.
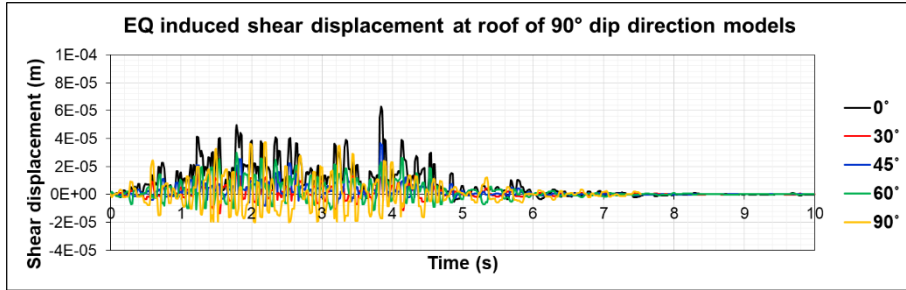
(a)
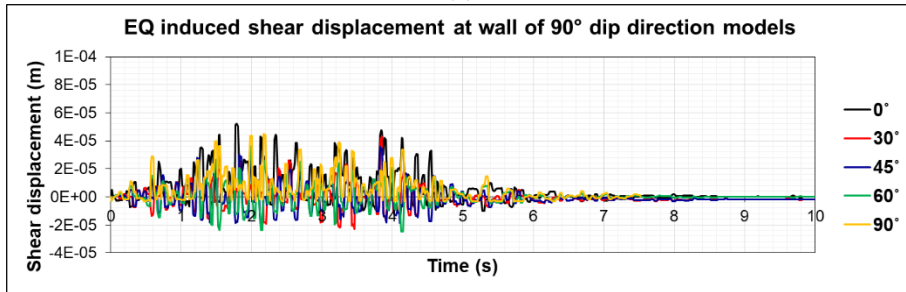
(b)
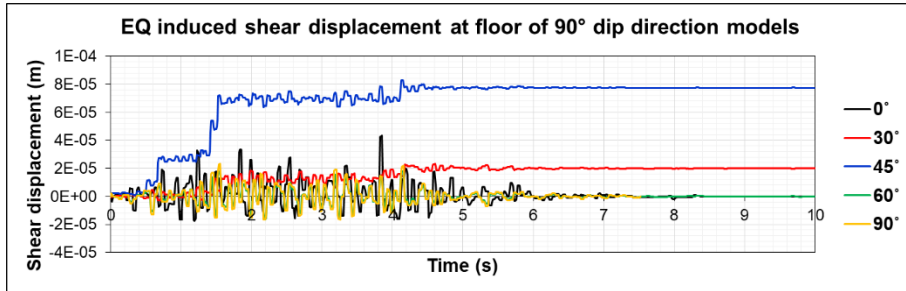
(c)

Figure 6.19 Shear displacement induced by a 0.8 m/s PGV earthquake at the (a) roof, (b) wall, and (c) floor of models with a 90° joint dip direction
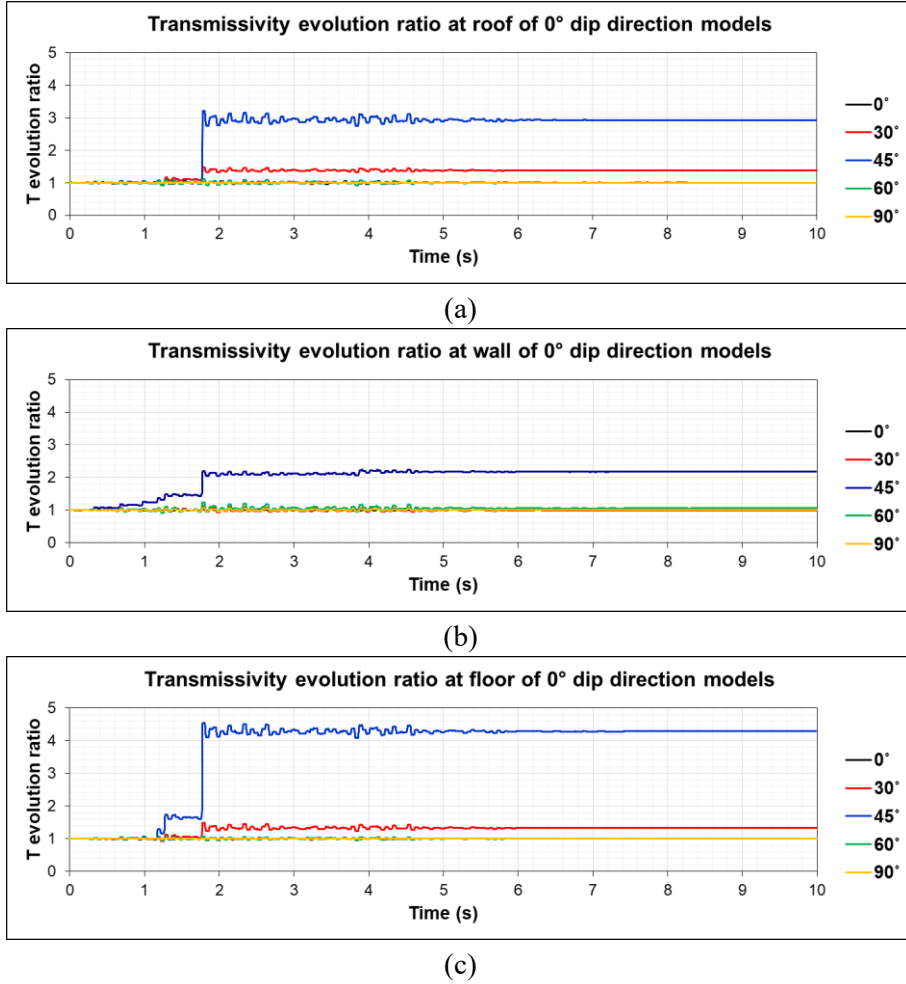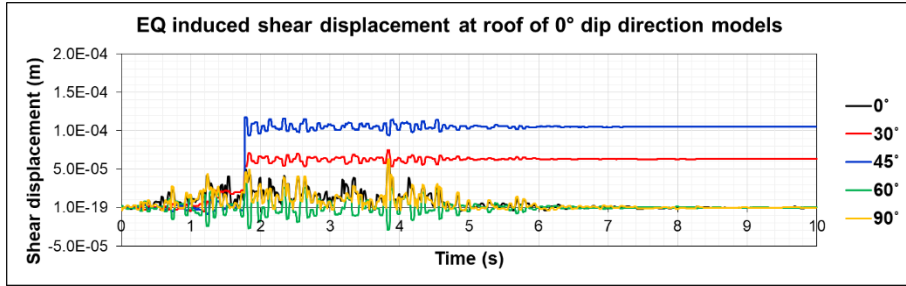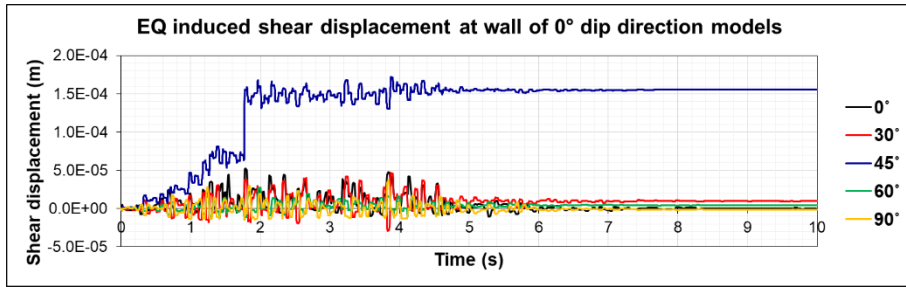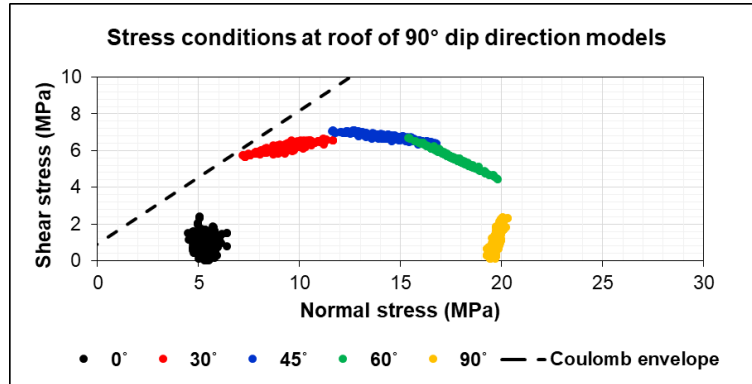
(a)
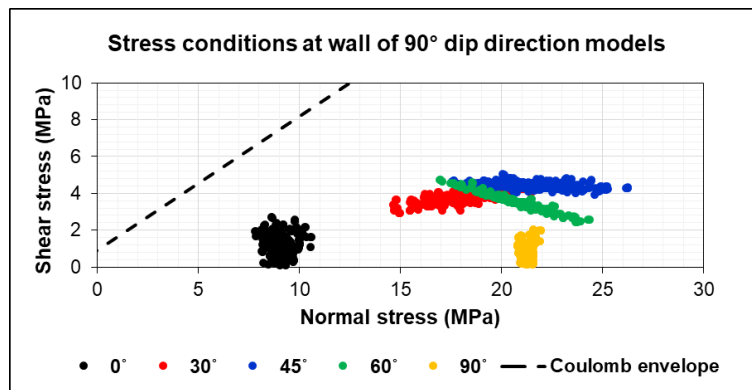
(b)
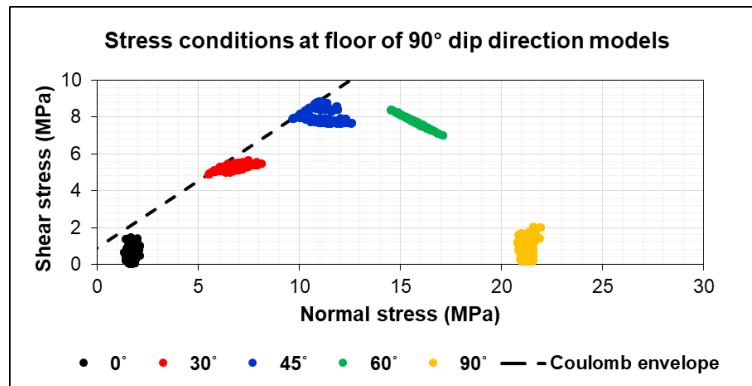
(c)

Figure 6.20 Stress conditions during a 0.8 m/s PGV earthquake at the (a) roof, (b) wall, and (c) floor of models with a 90° joint dip direction

114

The stress conditions during the earthquake scenarios are plotted with the Coulomb slip envelope in Figure 6.20. The fluctuation of stress conditions especially appeared on the normal stress of the 090/30, 090/45, and 090/60 models. Since the initial stress conditions of the 090/30 and 090/45 models at the tunnel floor are close to the Coulomb slip envelope, the stress conditions reached the envelope during the earthquake scenarios. Though the stress conditions at other monitoring points fluctuated with about 5 MPa of normal stress ranges and 3 MPa of shear stress ranges, it is not enough to induce the shear slip due to the high initial normal stress and low initial shear stress.

The magnitudes of the maximum transmissivity evolution ratios and their models are compiled in Table 6.1. Most maximum evolutions are extracted from the 0° dip direction models. The relatively low applied normal stress on joints during each scenario due to the small in-situ stresses may cause a large amount of shear slip. Under the external effects, the inclined joints, especially those inclined at about 30° from the adjacent tunnel surface, tended to show the largest transmissivity evolutions due to the shear stress concentration.

Table 6.1 Maximum transmissivity evolution ratio by each monitoring line and the models resulting in the maximum transsivity evolution ratio

		Excavation	Thermal loading	Glaciation	Earthquake
Maximum T evolution Ratio (Model)	Roof	187 (000/30)	1.21 (000/00)	105 (000/45)	2.93 (000/45)
	Wall	1620 (000/90)	2.32 (000/90)	143 (000/60)	2.17 (000/45)
	Floor	3390 (000/30)	2.34 (090/30)	79.8 (000/30)	4.29 (000/45)

Chapter 7. Discussions and conclusions

7.1 Discussions

This thesis focused on simulating the fracture transmissivity evolutions due to the excavation, thermal loading, glaciation, and earthquake, though there could be other external factors disturbing the stress conditions (i.e., sea-level change, tectonic movement, volcanic activity, and human actions) and more serious scenarios dominating the radionuclide leakage (i.e., corrosion, degradation, and breakage of engineered barriers) during about 100,000 years of the expected lifetime of geological repositories (NEA, 2019). Because the external factors handled in this thesis have been well specified in previous research, the numerical simulations required fewer assumptions to investigate the transmissivity evolutions. Still, the constructed three-dimensional discrete element model included several assumptions for simplifying the repository systems and scenarios. The following discussions explain the assumptions and their consequences.

7.1.1 Hydraulic coupling

The numerical simulations performed in this thesis only considered the mechanical and thermo-mechanical behaviors of fractured rock, and the transmissivity of fractures was represented by the mechanical aperture changes resulting from the mechanical behaviors of fractures. Although the most direct method for understanding the hydraulic conductivity of structures is performing a fluid flow simulation, this thesis tried to concentrate on the detailed mechanical

behaviors of models containing numerous fractures under thermal and mechanical disturbance. In the coupled thermo-hydro-mechanical simulations, the following issues could be additionally considered.

The effective normal stress applied on the fractures can be disturbed by the pore pressure changes during each scenario. Due to the external load, including thermal, glacial, and dynamic stresses, the pore pressure throughout the model could be increased and entails less normal closures and additional shear slip on fractures. Hökmark et al. (2010) also emphasized the effects of increased pore pressure with 98% of the glacially induced vertical stresses and showed additional shear displacement by considering the pore pressure. Therefore, the consideration of pore pressure could result in larger permanent transmissivity evolutions.

Apart from the hydraulic parameters, the hydraulic properties can be affected by the thermo-hydro-mechanical coupling effects. Fluid viscosity and density are the properties deciding the transmissivity of structures and were assumed as the constant value of water in this research. However, the viscosity and density of fluid should be considered as dynamic variables as the temperature changes (Hodgkinson et al., 1983). Indeed, in the thermal simulations, the rock temperatures simulations ranged from 11.5 to 54.5°C, which induces changes in water viscosity ranging from about 1.3 to 0.5 cP (Korson et al., 1969) and changes in water density ranging from about 1000 to 989 kg/m3 (Fierro Jr and Evans, 2007). However, the rock temperature recovered to its initial temperature at the end of the thermal scenario, so permanent changes to the transmissivity could not be affected by the change in hydraulic properties.

7.1.2 Fracture descriptions

The EDZ handled in this thesis represented a stress-induced EDZ according to the reversible deformations and irreversible shear dilations appearing in the pre-existing discontinuities around the excavation. However, the creation and propagation of fractures are also important factors originating in the EDZ with an irreversible property and stability disturbance. The creation and propagation of fractures can entail an increase of not only the equivalent transmissivity but also the connectivity with pre-existing fracture networks. Since the simulations in this thesis focused on the fracture transmissivities calculated from the aperture under external effects, the creation and propagation effects were neglected. In cases where the equivalent hydraulic properties of fractured rock mass are evaluated, the stress-induced fracture creation and propagation should be carefully analyzed.

As an assessment of the hydraulic performance of natural barriers, this thesis aimed to characterize the transmissivity of fractures by averaging results from the entire fracture surface (Chapter 5) or by obtaining the maximum value (Chapter 6). However, the fracture transmissivities calculated from the aperture were heterogeneously distributed regarding the stress conditions and properties on discrete sections of the fracture surfaces (Figure 5.16). Even though the fractures have low averaged fracture transmissivity, a channeling flow can be allowed through a fluid path constituted by a partial fracture area with high transmissivity (Tsang and Neretnieks, 1998; Auradou et al., 2006; Huang et al., 2019). Considerations of maximum transmissivity could overestimate the effects of disturbances, but it could also allow for investigating more conservative studies to assess the performance of

natural barriers.

The fracture transmissivity investigated in this study was defined by Cubic law with a simulated aperture on fractures during each scenario. Although the transmissivity in Cubic law is governed by the hydraulic aperture, this thesis assumed that mechanical apertures were the same parameters as the hydraulic apertures and proportionally related to the dilation angle of fractures. However, the hydraulic aperture could be disturbed by a variety of complicated aspects as a result of micro-mechanical responses on fractures, such as gouge and asperity damages (Olsson and Barton, 2001). Still, shear dilation approaches based on the dilation angle could describe the conservative studies that result in the upper bound of transmissivity increases of the fractured rock.

7.1.3 Repository design

By means of the three-dimensional DEM tool, this research aimed to model the geological repository for the HLW. However, there were assumptions simplifying the exact repository designs and disposing systems. In actual repositories, the deposition tunnels would not remain empty and free surfaces. When the disposal is finished, it is planned to backfill the deposition tunnel using components like crushed rock, bentonite pellets, and clay materials (Hansen et al., 2010). The backfill materials will fill about 73.5% of the deposition tunnel, and the tunnel will be closed using a concrete plug. The main advantage of backfill is its contribution to the mechanical stability at the vicinity of the deposition tunnel. Unlike the tunnel boundaries in this thesis, a backfilled tunnel surface is not mechanically free. Due to

the mechanical support, the discrepancies between the radial and tangential stress induced by the external effects can be reduced. Therefore, the numerical simulation in this thesis could overestimate the shear slip indicating a permanent transmissivity increase.

This thesis described a single deposition tunnel with multiple canisters generating decay heat. In geological disposing systems, these deposition tunnels are designed to be positioned with about 40 m of spacing to control the thermal and mechanical stability (SKB, 2010a). The numerical models constructed in this research had 50 m of width to reflect the tunnel spacing in the disposing systems. According to the numerical simulations in this research, the mechanical and thermal responses from the single tunnel model did not reach the boundary conditions, which indicates that the single tunnel model can represent the hydraulic performance of the fractured rock.

The engineered barriers, including the canister and buffer, were simplified, and the HLW was only reflected as a heat source in the numerical models. Since both the canister and buffer materials have different mechanical and thermal properties with the host rock, there could be discrepancies between the exact thermo-mechanical responses and the simulation results. Due to the simplification of the canister and buffer materials, the transient trend of temperature changes could be abridged, and temperature distribution could be different. In this simulation, the maximum temperature at the deposition wall appeared in 5 years, while previous numerical studies including a canister and buffer showed the peak temperature occurring in 10 ~ 50 years (Hökmark et al., 2010; Min et al., 2013). However, the simulation in this thesis concentrated on the effects of temperature changes on rock mass at the

maximum temperature stage and final stage, and the magnitude of temperature change is similar to the previous studies. Therefore, the transient trends and distributions of temperature could not affect the results of fracture transmissivity evolution.

Furthermore, a bentonite-based buffer showed swelling behaviors disturbing the mechanical conditions around the canister with a sensitive dependency on the thermal and hydraulic environment (Villar and Lloret, 2008). For the exact performance assessment regarding the specific geological repository model, the considerations of these detailed repository design should be conducted under coupled thermo-hydro-mechanical simulations.

7.2 Conclusions

In this research, a series of numerical simulations were performed to investigate changes in the transmissivity of fractures within the natural barriers of repository under the effects of stress re-distribution by excavation, thermal loading, glaciation, and earthquake. The detailed mechanical behaviors of fractures were analyzed by geometrical characteristics of fractures. The following conclusions were drawn:

The three-dimensional DEM models were constructed by containing the discrete fracture networks and uniformly distributed joint sets around the horseshoe-shaped tunnel. The normal stiffness and dilation angle played an important role in controlling the transmissivity changes in the vicinity of tunnel, so those parameters were assumed as stress-dependent values describing the realistic fracture behaviors observed in the in-situ and laboratory tests of specimens from the Äspö HRL. Both stress-dependent normal stiffness from the continuously yielding model and dilation angle from Barton and Choubey's empirical equation accompanied more drastic changes of transmissivity by depth than the constant parameters, which follows the transmissivity trends observed from the interference tests performed at the TAS04 tunnel at the Äspö HRL.

The stress re-distribution in the EDZ induced significant transmissivity increases on the discrete fractures with stress-dependent parameters in the Äspö HRL model. The transmissivity changes ranged from one-order decreases to three-order increases at the shallow depth depending on the fracture orientations. Of all the fractures, 23% showed transmissivity increases up to 2.5 m depth from the tunnel floor, and 6% of fractures showed a one-order increase of fracture transmissivity at

depths up to 1.3 m.

In the thermal loading scenarios, significant permanent increases in the fracture transmissivity were observed. At the peak of the temperature, the normal closure was dominant and reduced the transmissivity with veiling the effects of shear dilation. After the heat dissipates, the thermally normal closure disappeared, and the effects of irreversible shear dilation were revealed on the fracture transmissivity. The fracture transmissivity permanently increased up to one-order from the initial transmissivity up to a 3 m depth.

The glaciation scenarios accompanied permanent increases of transmissivity, and the magnitude of the transmissivity increases was larger than the thermally induced increases. During the loading cycles, the fracture transmissivity tended to be reduced due to the normal closure. After the unloading cycles, the fracture transmissivity recovered the initial values, and some of fractures showed a larger value due to the irreversible shear dilation. When the two glaciation cycles ended, the glacially induced permanent transmissivity increase appeared up to 10 m depth with more than a two-order increase from the initial transmissivity.

Earthquake also induced permanent fracture transmissivity increases. During the earthquake, the transmissivity fluctuated due to the reversible normal deformations induced by the normal stress fluctuation. When the shear stress fluctuation reached the Coulomb failure criteria, the fracture showed irreversible transmissivity increases. The earthquake model with 0.8 m/s of PGV resulted a transmissivity increase of about 1.08 times the initial transmissivity on the fractures with an inclined orientation from the tunnel surface.

Thermal, glacial, and earthquake scenarios consisted of loading and unloading

cycles along with recovering the initial stress conditions at the end. In all scenarios, the normal deformations and shear dilations simultaneously disturbed the fracture transmissivity due to the stress changes. Normal deformations tended to dominate the transmissivity changes at the loading cycles by veiling the shear dilation. However, at the end of scenarios, the reversible normal deformations dissipated, and only irreversible shear dilations remained as permanent transmissivity evolutions. According to the stress path during each scenario, the fracture behaviors were able to be categorized in two different ways, showing the reversible and irreversible transmissivity change depending on the geometrical characteristics.

To define the relation between the transmissivity changes and geometrical characteristics of discontinuities, the uniformly distributed joints were applied to the three-dimensional tunnel model, and the effects of stress re-distribution, thermal loading, glaciation, and earthquake were investigated as fracture transmissivity changes. In the excavation scenario, the largest increase appeared at the floor of the model with a 30° joint dip as a 3,390-times increase. The thermal scenarios resulted the largest transmissivity increases at the floor of the model with a 30° joint dip as a 2.34-time increase, and the glacial scenarios induced a 143-time maximum transmissivity increase at the wall of the model with a 60° joint dip. The earthquake scenarios showed the largest transmissivity increase at the floor of the model with a 45° joint dip at 4.29 times the initial value.

At the roof and floor of the tunnel, the joints with a 30° dip were highly dilated at the end of each scenario, while the model with a 60° joint dip resulted in high permanent transmissivity increases at the tunnel wall. The 90° dip direction joints maintained the initial transmissivity at the wall during every scenario. The

magnitude of the transmissivity evolution was generally high in the 0° dip direction models, which were parallel to the direction of the maximum horizontal stress due to the absence of the effects of the largest principal compressive stress at the shallow depth. According to the contour of the spatial extent for the disturbed zone, the permanent increase of transmissivity tended to appear around the tunnel surfaces slightly inclined from the joint plane due to the shear stress concentrations during all scenarios.

This thesis determined that permanent changes to the fracture transmissivity could be substantial under the effects of stress re-distribution, thermal loading, glaciation, and earthquake, which possibly can happen during the geological repository's lifetime. The results of this thesis indicate that the transmissivity of the crystalline rock obtained from the in-situ or laboratory measurement should be considered as dynamic variables changing as the geological repository operates.

Reference

Ahola MP, Chowdhury AH. Effect of seismic load on a proposed nuclear waste repository at Yucca mountain. Int J Rock Mech Min Sci. 1997;34(3-4):007.

Andersson JC. Äspö pillar stability experiment: Rock mass response to coupled mechanical thermal loading. TR-07-01. Stockholm, Sweden: Svensk Kärnbränslehantering AB (SKB); 2007.

Andersson JC, Martin CD. The Äspö pillar stability experiment: Part I – Experiment design. Int J Rock Mech Min Sci. 2009;46(5):865-878.

Andersson JC, Martin CD, Stille H. The Äspö pillar stability experiment: Part II – Rock mass response to coupled excavation-induce and thermal-induced stresses. Int J Rock Mech Min Sci. 2009;46(5):879-895.

Auradou H, Drazer G, Boschan A, Hulin JP, Koplik J. Flow channeling in a single fracture induced by shear displacement. Geothermic. 2006;35:576-588.

Autio J, Siitari-Kauppi MK, Timonen J, Hartikainen K, Hartikainen J. Determination of the porosity, permeability and diffusivity of rock in the excavation-disturbed zone around full-scale deposition holes using the C-14-PMMA and He-gas method. J Contam Hydrol. 1998;35:19-29.

Bäckblom G. Excavation damage and disturbance in crystalline rock – results from experiments and analyses. TR-08-08. Stockholm, Sweden: Svensk Kärnbränslehantering AB (SKB); 2008.

Barton CA, Zoback MD, Moos D. Fluid flow along potentially active faults in crystalline rock. Geology. 1995;23(8):683-686.

Barton N, Choubey V. The shear strength of rock joints in theory and practice. Rock Mechanics. 1977;10(1-2):1-54.

Bond A, Watson S. Understanding the post-closure thermal impact of HLW/SF waste packages, An NDR RWMD Ressearch Study. QRS-1384Q-R2. Oxfordshire, United Kingdom: Quintessa Limited; 2012.

Chan T, Christiansson R, Boulton GS, Ericsson LO, Hartikainen J, Jensen MR, Mas Ivars D, Stanchell FW, Vistrand P, Wallroth T. DECOVALEX III BMT3/BENCHPAR WP4: The thermo-hydro-mechanical responses to a glacial cycle and their potential implications for deep geologicl disposal of nuclear fuel waste in a fractured crystalline rock mass. Int J Rock Mech Min Sci. 2005;42:805-827.

Chen SG, Zhao J. A study of UDEC modelling for blast wave propagation in jointed rock masses. Int J Rock Mech Min Sci. 1998;35(1):93-99.

Christiansson R, Janson T. A test of different stress measurement methods in two orthogonal bore holes in Äspö Hard Rock Laboratory (HRL), Sweden. Int J Rock Mech Min Sci. 2003;40(7-8):1161-1172.

Cundall PA. A computer model for simulating progressive large scale movements in blocky rock systems. II-8, In Proc Symp ISRM; 1971.

Cundall PA, Hart RD. Numerical modeling of discontinua. Compr rock Eng Vol 2. 1993;9(February 1992):231-243.

Ericsson LO, Thörn J, Christiansson R, Lehtimäki T, Ittner H, Hansson K, Burtron C, Sigurdsson O, Kinnbom P. A Demonstration project on controlling and verifying the excavation-damaged zone. R-14-30. Stockholm, Sweden: Svensk Kärnbränslehantering AB (SKB); 2015.

Elkhoury JE, Brodsky EE, Agnew DC. Seismic waves increase permeability. Nature. 2006;441(29):1135-1138.

Elkhoury JE, Niemeijer A, Brodsky EE, Marone C. Laboratory observations of permeability enhancement by fluid pressure oscillation of in situ fractured rock. J Geophys Res Solid Earth. 2011;116:B02311.

Fäith B, Hökmark H, Munier R. Slip on repository rock fractures induced by large earthquakes. Results from dynamic discrete fracture modeling. ARMA 08-070. The

42nd US Rock Mech Symp; 2008

Fierro Jr P, Nyer EK. The water encyclopedia: Hydrologic data and internet resources. Boca Raton, Florida: CRC press; 2007.

Follin S, Hartley L, Rhén I, Jackson P, Joyce S, Roberts D, Swift B. A methodology to constrain the parameters of a hydrogeological discrete fracture network model for sparsely fractured crystalline rock, exemplified by data from the proposed high-level nuclear waste repository site at Forsmark, Sweden. Hydrogeol J. 2014;22:313-331.

Fransson Å. Literature survey: Relations between stress change, deformation and transmissivity for fractures and deformation zones based on in situ investigations. R-09-13. Stockholm, Sweden: Svensk Kärnbränslehantering AB (SKB); 2009.

Gomes JP, Lemos JV. Characterization of the dynamic behavior of a concrete arch dam by means of forced vibration tests and numerical models. Earthquake Engng Sturct Dyn, 2020;49:679-694.

Hakami E, Fredriksson A, Lanaro F, Wrafter J. Rock Mechanics Laxemar: Site descriptive modelling SDM-Site Laxemar. R-08-57. Stockholm, Sweden: Svensk Kärnbränslehantering AB (SKB); 2008.

Hansen J, Korkiala-Tanttu L, Keski-Kuha E, Keto P. Deposition tunnel backfill design for a KBS-3V repository. Working report 2009-129. Eurajoki, Finland: Posiva

Oy; 2010.

Harrison JP, Hudson JA. Engineering rock mechanics: part 2: illustrative worked examples. Amsterdam, The Netherlands: Elsevier; 2000.

Hashash Y, Hook J, Schmidt B, Yao J. Seismic design and analysis of underground structures. Tunn Underg Sp Tech. 2001;16:247-293.

Hodgkinson DP, Lever DA, Rae J. Thermal aspects of radioactive waste burial in hard rock. Prog Nucl Energ. 1983;11(2):183-218.

Hökmark H, Lönnqvist M, Kristensson O, Sundberg J, Hellstöm G. Strategy for thermal dimensioning of the final repository for spent nuclear fuel. R-09-04. Stockholm, Sweden: Svensk Kärnbränslehantering AB (SKB); 2009.

Hökmark H, Lönnqvist M, Fälth B. THM-issues in repository rock. TR-10-23. Stockholm, Sweden: Svensk Kärnbränslehantering AB (SKB); 2010.

Hong S, Effect of excavation and thermal stress on slip zone and permeability change around deposition hole and tunnel in fracture rock. MS Dissertation. Seoul National University; 2020.

Huang N, Liu R, Jiang Y, Cheng Y, Li B. Shear-flow coupling characteristics of a three-dimensional discrete fracture network-fault model considering stress-induced

aperture variations. J Hydrol. 2019;571:416-424.

Hudson JA, Bäckström A, Rutqvist J, et al. Characterising and modelling the excavation damaged zone in crystalline rock in the context of radioactive waste disposal. Environ Geol. 2009;57(6):1275-1297.

Hutri KL, Antikainen J. Modelling of the bedrock response to glacial loading at the Olkiluoto site, Finland. Eng Geol. 2002;67(1-2):39-49.

Ikonen K. Fuel temperature in disposal canister. Working Report 2006-19, Eurajoki, Finland: Posiva Oy; 2006.

Ikonen K, Raiko H. Thermal analysis of a KBS-3H repository. Working Report 2015-01, Eurajoki, Finland: Posiva Oy; 2015.

Itasca Consulting Group. UDEC 6.0 User's Guide. Minneapolis, Minnesota: Itasca Consulting Group Inc.; 2014.

Itasca Consulting Group. 3DEC 5.0 User's Guide. Minneapolis, Minnesota: Itasca Consulting Group Inc.; 2013.

Jing L. A review of techniques, advances and outstanding issues in numerical modelling for rock mechanics and rock engineering. Int J Rock Mech Min Sci. 2003;40(3):283-353.

Kiuru R, Heikkinen E, Jacobsson L, Kovacs D. EDZ Study area in ONK-TKU-3620: Petrophysical, rock mechanics and petrographic testing and analysis conducted on drill core specimens between 2014 and 2016. Working Report 2017-56, Eurajoki, Finland: Posiva Oy; 2019.

Koyama T, Chijimatsu M, Shimizu H, Nakama S, Fujita T, Kobayashi A, Ohnishi Y. Numerical modeling for the coupled thermo-mechanical processes and spalling phenomena in Äspö Pillar Stability Experiment (APSE). J Rock Mech Geotech Eng. 2013;5:58-72.

Kwon S, Cho WJ. The influence of an excavation damaged zone on the thermal-mechanical and hydro-mechanical behaviors of an underground excavation. Eng Geol. 2008;101:110-123.

Kwon S, Lee CS, Cho SJ, Jeon SW, Cho WJ. An investigation of the excavated damaged zone at the KAERI underground research tunnel. Tunn Undergr Sp Tech. 2009;24:1-13.

Kwon S, Min KB. Fracture transmissivity evolution around the geological repository of nuclear waste caused by the excavation damage zone, thermoshearing and glaciation. Int J Rock Mech Min Sci. (accepted)

Lee C. Characterization of thermal-mechanical behavior of rock mass in the excavation damaged zone at KURT. PhD dissertation. Seoul National University;

2012.

Lemos JV. Block modelling of rock masses, Eur J Environ Civ Eng. 2008:12(7-8):915-949.

Loutre MF, Berger A. Future climatic changes: Are we entering an exceptionally long interglacial? Climatic Change. 2000;46:61-90.

Lund B, Schmidt P, Hieronymus C. Stress evolution and fault stability during the Weichselian glacial cycle. Waste Manag. TR-09-15. Stockholm, Sweden: Svensk Kärnbränslehantering AB (SKB); 2009.

Mas Ivars D, Lope Álvarez D, Sánchez Juncal A, Ghazal R, Damjanac B. Parametrisation of fractures – Estimation of fracture shear displacement due to excavation of new slots at the TASQ tunnel via numerical modeling. Working Report 2015-28. Eurajoki, Finland: Posiva Oy; 2015.

Meacham PG, Anderson DR, Bonano EJ, Marietta MG. Sandia National Laboratories Performance Assessment Methodology for Long-Term Environmental Programs: The History of Nuclear Waste Management. SAND2011-8270. Albuquerque, New Mexico: Sandia National Laboratories; 2011.

Meier T, Backers T. DECOVALEX-2019 Task G Final Report, LBNL-2001266. Berkeley, California: Lawrence Berkeley National Laboratory (LBNL); 2020.

Min KB, Lee J, Stephansson O. Implications of thermally-induced fracture slip and permeability change on the long-term performance of a deep geological repository. Int J Rock Mech Min Sci. 2013;61:275-288.

Min KB, Rutqvist J, Tsang CF, Jing L. Stress-dependent permeability of fractured rock masses: A numerical study. Int J Rock Mech Min Sci. 2004;41(7):1191-1210.

Min KB, Rutqvist J, Tsang CF, Jing L. Thermally induced mechanical and permeability changes around a nuclear waste repository - A far-field study based on equivalent properties determined by a discrete approach. Int J Rock Mech Min Sci. 2005;42(5-6):765-780.

Min KB, Thoraval A. Comparison of Two- and Three-dimensional Approaches for the Numerical Determination of Equivalent Mechanical Properties of Fractured Rock Masses. Tunn Underg Sp. 2012;22(2):93-105.

Munier R. Four-dimensional analysis of fracture arrays at Äspö hard rock laboratory, SE Sweden. Eng Geol. 1993;33:159-175.

Näslund JO. Ice sheet dynamics, in Climate and climate related issues for the safety assessment SR-Can. TR-06-23. Stockholm, Sweden: Svensk Kärnbränslehantering AB (SKB); 2006.

NEA. International Features, Events and Processes (IFEP) list for the deep

geological disposal of radioactive waste. Version 3.0. Paris, France: Nuclear Energy Agency (NEA) – OECD; 2019.

Olsson R, Barton N. An improved model for hydromechanical coupling during shearing of rock joints. Int J Rock Mech Min Sci. 2001;38:317-329.

Park J. Fracture shearing and the evolution of transmissivity due to thermal, glacial and earthquake loadings in geological repository of spent nuclear fuel. MS dissertation. Seoul National University; 2015.

Park J, Lee J, Min KB, Stephansson O, Lanaro F. Transmissivity evolution due to fracture shearing for the thermal, glacial and earthquake scenarios of a deep geological repository of spent nuclear fuel at Forsmark, Sweden. ISRM Reg Symp EUROCK 2015. 2015:597-602.

Pimenoff N, Venäläinen A, Järvinen H. Climate scenarios for Olkiluoto on a time-scale of 120,000 years. POSIVA 2011-04. Eurajoki, Finland: Posiva Oy; 2011.

Posiva. Safety case for the disposal of spent nuclear fuel at Olkiluoto – Design basis 2012. POSIVA 2012-03. Eurajoki, Finland: Posiva Oy; 2012.

Pusch R. Alteration of the hydraulic conductivity of rock by tunnel excavation. Int J Rock Mech Min Sci Geomech Abstr. 1989;26(1):79-83.

Raiko H, Sandström R, Rydén H, Johansson M. Design analysis report for the canister. TR-10-28. Stockholm, Sweden: Svensk Kärnbränslehantering AB (SKB); 2010.

Rutqvist J, Freifeld B, Min KB, Elsworth D, Tsang Y. Analysis of thermally induced changes in fractured rock permeability during 8 years of heating and cooling at the Yucca Mountain Drift Scale Test. Int J Rock Mech Min Sci. 2008;45(8):1373-1389.

Rutqvist J, Stephansson O. The role of hydromechanical coupling in fractured rock engineering. Hydrogeol J. 2003;11(1):7-40.

Rutqvist J, Freifeld B, Min KB, Elsworth D, Tsang Y. Analysis of thermally induced changes in fractured rock permeability during 8 years of heating and cooling at the Yucca Mountain Drift Scale Test. Int J Rock Mech Min Sci. 2008;45:1373-1389.

Rutqvist J, Bäckström A, Chijimatsu M, Feng XT, Pan PZ, Hudson J, Jing L, Kobayashi A, Koyama T, Lee HS, Huang XH, Rinne M, Shen B. A multiple-code simulation study of the long-term EDZ evolution of geological nuclear waste repositories. Environ Geol. 2009;57:1313-1324.

Saanio T, Ikonen A, Keto P, Kirkkomäki T, Kukkola T, Nieminen J, Raiko H. Design of the Disposal Facility 2012. Working Report 2013-17. Eurajoki, Finland:Posiva Oy, 2012.

Sharma S, Juud WR. Underground opening damage from earthquakes. Eng Geol. 1991;30:263-276.

Shen B, Barton N. The disturbed zone around tunnels in jointed rock masses. Int J Rock Mech Min Sci. 1997;34(1):117-125.

Siren T, Kantia P, Rinne M. Considerations and observations of stress-induced and construction-induced excavation damage zone in crystalline rock. Int J Rock Mech Min Sci. 2015;73:165-174.

Siren T. Excavation Damage Zones, Fracture Mechanics Simulation and in Situ Strength of Migmatitic Gneiss and Pegmatitic Granite at the Nuclear Waste Disposal Site in Olkiluoto, Western Finland. PhD Dissertation. Aalto University; 2015.

SKB. Site description of Forsmark at completion of the site investigation phase. TR-08-05. Stockholm, Sweden: Svensk Kärnbränslehantering AB (SKB); 2008.

SKB. Design, construction and initial state of the underground openings for operational and long-term safety. TR-10-18. Stockholm, Sweden: Svensk Kärnbränslehantering AB (SKB); 2010a.

SKB. Data report for the safety assessment SR-Site. TR-10-52. Stockholm, Sweden: Svensk Kärnbränslehantering AB (SKB); 2010b.

SKB. Comparative analysis of safety related site characteristics. TR-10-54. Stockholm, Sweden: Svensk Kärnbränslehantering AB (SKB); 2010c.

SKI. Characterization of seismic ground motions for probabilistic safety analyses of nuclear facilities in Sweden. SKI Technical Report 92:3. Stockholm, Sweden: Swedish Nuclear Power Inspectorate (SKI); 1992.

SSM. The Swedish Radiation Safety Authority's Regulations and general advice concerning the protection of human health and the environment in connection with the final management of spent nuclear fuel and nuclear waste. SSMFS 2008:37. Stockholm, Sweden: Swedish Radiation Safety Authority (SSM); 2008.

Tsai YB, Huang MW. Strong ground motion characteristics of the Chi-Chi, Taiwan earthquake of September 21, 1999. Earthquake Eng Eng Seism. 2000;2:1-21.

Tsang CF, Bernier F, Davies C. Geohydromechanical processes in the Excavation Damaged Zone in crystalline rock, rock salt, and indurated and plastic clays - In the context of radioactive waste disposal. Int J Rock Mech Min Sci. 2005a;42(1):109-125.

Tsang CF, Jing L, Stephansson O, Kautsky F. The DECOVALEX III project: A summary of activities and lessons learned. Int J Rock Mech Min Sci. 2005b;5-6:593-610.

Tsang CF, Neretnieks I. Flow channeling in heterogeneous fractured rocks. Rev Geophys. 1998;36(2):275-298.

Valli J, Hakala M, Wanne T, Kantia P, Siren T. ONKALO POSE Experiment – Phase 3: Execution and Monitoring. Working Report 2013-41. Eurajoki, Finland: Posiva Oy; 2013.

Vidstrand P, Wallroth T, Ericsson LO. Coupled HM effects in a crystalline rock mass due to glaciation: indicative results from groundwater flow regimes and stresses from an FEM study. Bull Eng Geol Environ. 2008;67:187-197.

Villar MV, Lloret A. Influence of dry density and water content on the swelling of a compacted bentonite. Appl Clay Sci. 2008;39:38-49.

Wang WL, Wang TT, Su JJ, Lin CH, Seng CR, Huang TH. Assessment of damage in mountain tunnels due to the Taiwan Chi-Chi Earthquake. Tunn Underg Sp Tech. 2001;16:133-150.

Xue L, Li HB, Brodsky EE, Xu ZQ, Kano Y, Wang H, Mori JJ, Si JL, Pei JL, Zhang W, Yang G, Sun ZM, Huang Y. Continuous permeability measurements record healing inside the Wenchuan Earthquake fault zone. Science. 2011;340(6140):1555-1559.

Yeo IW, De Freitas MH, Zimmerman RW. Effect of shear displacement on the

aperture and permeability of a rock fracture. Int J Rock Mech Min Sci. 1998;35(8):1051-1070.

Zimmerman RW, Bodvarsson GS. Hydraulic conductivity of rock fractures. Transport in Porous Media. 1996;23(1):1-30.

Zhao Z, Guo T, Li S, Wu W, Yang Q, Chen S. Effects of joint surface roughness and orientational anisotropy on characteristics of excavation damaged zone in jointed rocks. Int J Rock Mech Min Sci. 2020;128:104265.

초   록

원자력발전에서 발생하는 고준위 방사성 폐기물은 계속해서 방사선과 열을 발생하기 때문에, 충분한 시간 동안 생태계로부터 격리되어야 한다. 고준위 방사성 폐기물을 영구적으로 처분하는 방법으로 공학적방벽과 천연방벽을 통해 격리시키는 심지층처분방식이 제시되었다. 심지층처분 시스템의 성능을 평가하기 위하여 공학적방벽과 천연방벽의 장기적 거동을 조사하는 다양한 실험 및 수치해석이 진행되고 있다. 특히 천연방벽의 투수량계수는 핵종의 누출을 평가할 수 있는 수단으로 다양한 열, 수리. 역학적 영향 요인에 대한 분석이 필요하다.

본 논문에서는 고준위 방사성 폐기물 심층처분장의 건설 및 운영 중에 천연방벽, 특히 결정질 균열암반의 투수량계수 변화에 대하여 검토하였다. 결정질 균열암반의 실제 거동을 모사하기 위하여 스웨덴 애스푀 지하연구시설에서 취득한 암석 및 균열 물성을 활용하여 삼차원 개별요소법 기반 균열암반모델을 구축하였다. 균열투수량계수에 영향을 주는 요인인 굴착손상영역, 열, 빙하, 지진에 의한 응력 변화를 수치해석 모델에 반영하였다. 굴착손상영역의 영향은 터널 자유면에 의한 응력재분배가 야기한 균열의 수직변형 및 전단 미끄러짐을 통하여 투수량계수의 변화를 분석하였으며, 이렇게 구축된 터널 모델에 각각 열원, 빙하에 의한 경계조건변화, 지진에 의한 동적 하중을 추가하여 각 영향요인에 의한 투수량계수 변화를 분석하였다.

굴착손상영역으로 인한 영향은 크게는 1,000배가량의 투수량계수

141

증진으로 나타났고, 수직 열림/닫힘과 전단 미끄러짐에 의한 영향이 균열의 방향에 따라서 복합적으로 작용한 것으로 나타났다. 열, 빙하, 지진에 의한 영향 분석에서는 모두 하중의 재하와 제하가 반복되는 비슷한 응력변화 양상을 수반하였으며 영향의 분석이 끝난 후에는 모두 초기 응력조건으로 회귀하는 과정이 포함되어 있었다. 열, 빙하, 지진에 의한 영향 분석 모두 일부 균열에서 비가역적인 투수량계수의 증진이 확인되었다. 시간에 따른 투수량계수 및 응력 상태를 분석한 결과 하중의 재하 시에는 균열의 수직 닫힘이 지배적으로 나타났지만, 제하 시에는 닫혔던 균열이 가역적으로 열림과 동시에 수직 닫힘에 의해 가려졌던 비가역적 전단팽창의 영향이 드러났다. 이러한 가역적 수직변형과 비가역적 전단팽창의 영향은 균열의 기하학적 특성에 따라 선별적으로 나타났다.

투수량계수의 변화를 터널 주변 절리의 기하학적 특성에 대하여 보다 일반적으로 분석하기 위하여, 균일절리군을 터널 주변에 추가하여 각각 굴착손상영역, 열, 빙하, 지진에 의한 영향을 정리하였다. 투수량계수의 증진은 주로 최대주응력과 평행인 절리에서 크게 나타났으며, 이는 최대주응력의 영향이 작아 수직방향으로 작용하는 압축응력이 상대적으로 낮았기 때문이었다. 또한 터널면으로부터 약간 기울어진 방향의 절리에서 투수량계수의 증진이 크게 발생했으며, 이는 역학적으로 자유로운 터널면 때문에 추가적인 응력이 절리면 상에서 전단응력으로 집중되어 비가역적인 전단팽창이 크게 발생한 것으로

확인되었다.

　본 논문의 결과는 고준위 방사성 폐기물 심층처분장의 계획 및 건설 시 굴착손상영역, 열, 빙하, 지진 시나리오를 고려한 성능 평가의 기초 자료로 활용될 수 있으며, 투수량계수와 같은 천연방벽의 수리학적 인자가 시간에 따라서 변화할 수 있다는 것을 제시하였다.

143